Effects of Regional Deletion of Rab3A-interacting Molecule 1 and PTEN on Brain Function

APPROVED BY SUPERVISORY COMMITTEE

Craig M. Powell M.D., Ph.D.

_____

Amelia J. Eisch, Ph.D.

_____

Kimberly Huber, Ph.D.

_____

Matthew Goldberg, Ph.D.

_____

DEDICATION

I dedicate this thesis to my wife Tracy, who has supported me through the ups and downs of graduate school, and continues to support me as we journey through the rest of the Medical Scientist Training Program. I cannot thank Tracy, or my children, Nathan, Andrew and Margaret, enough for the many sacrifices they have made on my behalf, and for the future sacrifices they will make during residency and fellowship training wherever those may be.

Effects of Regional Deletion of Rab3A-interacting Molecule 1 and PTEN on Brain Function

by

MICHAEL EDWARD HAWS

DISSERTATION

Presented to the Faculty of the Graduate School of Biomedical Sciences

The University of Texas Southwestern Medical Center at Dallas

In Partial Fulfillment of the Requirements

For the Degree of

DOCTOR OF PHILOSOPHY

The University of Texas Southwestern Medical Center at Dallas

Dallas, Texas

May 2014

Effects of Regional Deletion of Rab3A-interacting Molecule and PTEN on Brain Function

MICHAEL EDWARD HAWS, Ph.D.

The University of Texas Southwestern Medical Center at Dallas, 2012

Craig M. Powell, M.D. Ph.D.

This dissertation describes experiments designed to delete/knockdown molecules from targeted neuronal populations to study brain region-specific behavioral functions. To this end, I utilized two different conditional knockdown techniques to study the role of the presynaptic active zone molecule Rab3A-interacting Molecule (RIM1) and the phosphatase and tensin homologue on chromosome 10 (PTEN).

The cre-lox system was used to eliminate RIM1 from the hippocampal dentate gyrus and area CA3, while adeno-associated virus expressing PTEN-directed interference RNA was injected into the basolateral amygdala to knockdown PTEN in local pyramidal neurons.

In the case of RIM1, I hypothesized that deletion of RIM1 from the dentate gyrus or from area CA3 would replicate a subset of the learning and memory deficits found in RIM1α-/- mice. Though the conditional RIM1 knockout mice were not completely selective for the dentate gyrus or for area CA3, both conditional knockouts induced a different behavioral abnormality present in RIM1α-/- mice. My results help narrow the potential brain regions involved in key RIM1α-/- mice behavioral aberrations.

In the case of PTEN, I hypothesized that deletion of PTEN specifically in the basolateral amygdala (BLA) would cause increased anxiety and neuronal hypertrophy. Knockdown of PTEN in the BLA did not induce anxiogenesis though it did increase soma volume, dendritic caliber, spine size, mushroom:thin spine ratio, and the frequency of spontaneous miniature excitatory post-synaptic currents. These findings are in contrast to previous findings of increased spine density with PTEN knockdown. This difference likely represents the more sensitive techniques employed in the present studies to ascertain dendritic spine type and density. Though PTEN knockdown had synaptic effects I did not observe

any behavioral effects. However, limitations in viral knockdown of PTEN transcripts or viral infection rate may be responsible for the lack of effect.

Indeed, limitations exist for both the transgenic and viral approaches used which proved to be challenging obstacles to designing experiments, interpreting data and coming to more extensive concrete conclusions. Transgene expression is often not as selective as desired. Virus injections may not localize to target region or may not infect enough neurons. Understanding and characterizing these and other limitations is vital.

TABLE OF CONTENTS

PRIOR PUBLICATIONS

Hur EM, Youssef S, **Haws ME**, Zhang SY, Sobel RA, Steinman L. **Osteopontin-induced relapse and progression of autoimmune brain disease through enhanced survival of activated T cells**. Nat Immunol. 2007 Jan;8(1):74-83. Epub 2006 Dec 3.

Speed HE, Blaiss CA, Kim A, **Haws ME**, Melvin NR, Jennings M, Eisch AJ, Powell CM. **Delayed reduction of hippocampal synaptic transmission and spines following exposure to repeated subclinical doses of organophosphorus pesticide in adult mice.** Toxicol Sci. 2012 Jan;125(1):196-208. Epub 2011 Sep 26.

Haws ME, Kaeser PS, Jarvis DL, Südhof TC, Powell CM. **Region-specific deletions of RIM1 reproduce a subset of global RIM1α(-/-) phenotypes.** Genes Brain Behav. 2012 Mar;11(2):201-13. Epub 2012 Jan 3.

Haws ME, Espinosa-Becerra F, Widman A, Jaramillo T, Stuber G, Sparta D, Russo S, Kaplitt M, Bonci A, and Powell CM. **PTEN knockdown regulates dendritic spine morphology but not density.** Submitted to Journal of Neuroscience 2012.

LIST OF FIGURES

Chapter 1: Region-specific deletions of RIM1 reproduce a subset of global RIM1α-/- phenotypes

Chapter 2: PTEN knockdown regulates dendritic spine morphology but not density

Chapter 3: Synthesis and Discussion

LIST OF TABLES

LIST OF ABBREVIATIONS

αCaMKII	alpha calmodulin protein kinase II
AAV	adeno-associated virus
AKT	protein kinase B
ANOVA	analysis of variance
Arc	arcuate nucleus of the hypothalamus
BDNF	brain-derived neurotrophic factor
BGH	bovine growth hormone
BLA	basolateral amygdala
CA1	cornu ammonis region 1
CA3	cornu ammonis region 3
CB1	cannabinoid receptor 1
CBA	chicken β-actin
cKO	conditional knockout
CMV	cytomegalovirus
CS	conditioned stimulus
Cβ1	catalytic subunit of protein kinase A
DAPI	4',6-Diamidino-2-Phenylindole
DEPC-PBS	diethylpyrocarbonate in phosphate buffered saline

DG	dentate gyrus of the hippocampus
DLX-cre	cre recombinase transgene driven by the distal-less homeobox 5/6 promoter
DNA	deoxyribonucleic acid
eCBs	endocannabinoids
ERK	extracellular signal-regulated kinase
Et al	Et alii (In English: and others)
fMRI	functional magnetic resonance imaging
fRIM1	floxed allele of Rab3A interacting molecule 1
GABA	gamma-aminobutyric acid
GAD	generalized anxiety disorders
GFP	green fluorescent protein
GL	cerebellar granule cell layer
HSV	herpes simplex virus
IHC	immunohistochemistry
iLTD	inhibitory long-term depression
ITR	inverted terminal repeats
KA-cre	cre recombinase transgene driven by the kainate receptor subunit 1 promoter
KO	knockout
LTD	long term depression

LTP	long-term potentiation
MAP2	microtubule associated protein 2
MEK	mitogen-activated protein kinase kinase
mEPSC	miniature excitatory post-synaptic currents
mfLTP	mossy fiber long-term potentiation
ML	cerebellar molecular layer
mPFC	medial prefrontal cortex
mTOR	mammalian target of rapamycin
NDS	normal donkey serum
NeuN	neuronal nuclei
PB	phosphate buffer
PBS	phosphate buffered saline
PCL	cerebellar purkinje cell layer
PI3K	phosphoinositide 3-kinase
PKA	protein kinase A
PKC	protein kinase C
PLCγ	phospholipase Cγ
POMC-cre	cre recombinase transgene driven by the pro-opiomelanocortin promoter
PPF	paired pulse facilitation

PPI	paired pulse inhibition
P_r	probability of release
PTEN	phosphatase and tensin homolog
PTP	post-tetanic potentiation
PTSD	post-traumatic stress disorder
PV	parvalbumin
qRT-PCR	quantitative reverse transcription polymerase chain reaction
R1β	Regulatory subunit of protein kinase A
R26R-YFP	YFP expressing ROSA reporter mouse
rAAV	recombinant adeno-associated virus
Rab3A	ras-related protein 3A
Rac1	Ras-related C3 botulinum toxin substrate 1
RIM1	Rab3A Interacting Molecule 1
RIM1α	alpha isoform of Rab3A Interacting molecule 1
RIM2	Rab3A Interacting Molecule 2
RIM3	Rab3A Interacting Molecule 3
RIM4	Rab3A Interacting Molecule 4
RIMs	Rab3A Interacting Molecules
rmANOVA	analysis of variance with repeated measures

RNA	ribonucleic acid
RXX	RIM1 recombined allele
SEM	standard error of the mean
shLuc	luciferase-silencing short hairpin loop RNA
shPTEN	PTEN-silencing short hairpin loop RNA
St	striatum
Th	thalamus
TrkB	tyrosine kinase receptor B
US	unconditioned stimulus
WPRE	woodchuck hepatitis virus post-transcriptional regulatory element
WT	wild type
YFP	yellow fluorescent protein

CHAPTER 1

Region-specific deletions of RIM1 reproduce a subset of global RIM1α-/- phenotypes

(Haws et al., 2012)

Chapter 1, Section 1

Introduction and Methods

Introduction

Understanding the biochemical mechanisms of learning and memory and cognition is a critical step toward treating primary disorders of learning and memory as well as psychiatric and neurologic diseases. These include Alzheimer's, autism spectrum disorder, major depression, anxiety, mental retardation, dementia and schizophrenia to name just a few. These illnesses are diverse, affect every age group and, although knowledge is increasing, their causes still remain unexplained in many cases. Over the past 5 or 6 decades the many mechanisms of synaptic plasticity have become a central point of interest to many scientists and understanding their physiological role in learning and memory, cognition and disease is a principal goal of neuroscience. Post synaptic mechanisms of plasticity are perhaps the most studied and their role in cognitive processes is being elucidated (Kandel, 2001, Matynia et al., 2002). Many of these molecular processes intersect with human disorders such as mental retardation, Alzheimer's disease and schizophrenia (Weeber et al., 2002a, Weeber et al., 2002b, Weeber and Sweatt, 2002, Young et al., 2010).

The role of presynaptically expressed forms of plasticity are less clear, but not less important. Little is known of the mechanisms by which presynaptically expressed forms of short- and long-term plasticity may participate in information processing/

storage or may affect cognition, though their involvement is clear (Powell, 2006).

In mice, global deletion of presynaptic proteins often results in significant behavioral abnormalities reminiscent of human cognitive disease. Silva et al. have found that decreases in paired pulse facilitation (PPF) or post-tetanic potentiation (PTP), two forms of presynaptic short term plasticity, in synapsin II-/-, synapsin I/II-/-, and alpha calmodulin-dependent protein kinase II heterozygous mutants (αCaMKII +/-) displayed learning deficits in fear conditioning and the Morris water maze (MWM) (Silva et al., 1996). Furthermore, enhanced cornu ammonis 1 of the hippocampus (CA1) PPF or PTP has also been associated with learning abnormalities in synaptotagmin $IV^{-/-}$ mice (Ferguson et al., 2004). Mice lacking neurexin, a presynaptic protein associated with autism spectrum disorder, have alterations of synaptic function and a disturbance of social behavior (Etherton et al., 2009). These findings are supported by post mortem studies of schizophrenic brains that have consistently found alterations in presynaptic proteins, particularly genes involved in neurotransmission of gamma-aminobutyric acid (GABA), in the cerebellum, hippocampus and cortex (Glantz and Lewis, 1997, Eastwood et al., 2001, Sawada et al., 2005, Tamminga et al., 2004, Guidotti et al., 2000, Akbarian and Huang, 2006, Woo et al., 2004).

The most studied form of long-term presynaptic plasticity occurs in the hippocampus where mossy fibers synapse onto cornu ammonis 3 (CA3) pyramidal cells, though its role is somewhat controversial: mossy fiber long-term potentiation (mfLTP) (Henze et al., 2000). One study finds that the absence of the regulatory (R1β) or catalytic

(Cβ1) subunit of protein kinase A (PKA) prevents mfLTP while sparing several learning and memory tasks including the Morris water maze (MWM) and fear conditioning (Huang et al., 1995). Ras-related protein 3A (Rab3A) deficient mice, which also lack mfLTP, support this finding (Hensbroek et al., 2003, Powell et al., 2004). However, a more thorough behavioral investigation of the Rab3A deficient mouse reports a deficit in the delayed-match-to-place version of the Morris water maze, suggesting that mfLTP plays a role in more complex forms of "episodic-like" spatial memory or working memory (D'Adamo et al., 2004). These subtler types of learning and memory were not studied in the preceding mouse models that were lacking mfLTP. Unfortunately, all of these studies are confounded by the additional synaptic abnormalities these global knockout (KO) mice possess, precluding a true association of hippocampal-specific functions of these plasticity-mediating genes to the observed behavioral abnormalities.

Another form of presynaptic plasticity that has gained significant attention is mediated by endocannabinoids (eCBs). In this pathway, eCBs are made in the postsynaptic cell in response to excitatory inputs, diffuse out of the cell and bind their receptor, cannabanoid receptor 1 (CB1), on the presynaptic membrane, or the membrane of other nearby inputs, ultimately decreasing neurotransmitter release. Both short- and long-term forms of CB1-mediated plasticity exist although different signaling pathways are used downstream of the CB1 receptor. Inhibitory long term depression (iLTD) is a PKA dependent form of CB1-mediated presynaptic plasticity (Chevaleyre et al., 2006, Chevaleyre et al., 2007). The CB1 receptor KO mouse exhibits a deficit in

extinction of auditory fear conditioning compared to wild-type (WT) controls, a phenotype mimicked with local application of CB1 antagonists to the basolateral amygdala (BLA), a brain region known to be involved in extinction of aversive memories (Marsicano et al., 2002, Chhatwal et al., 2005, Varvel et al., 2005, Kamprath et al., 2006, Cannich et al., 2004). Additional studies have suggested a role of the CB1 receptor in other learning tasks such as MWM, 8 arm radial maze, and delayed-non-match-to-sample (Lichtman et al., 2002, Robinson et al., 2007).

In addition to the genes already discussed above, all of the forms of presynaptic plasticity mentioned also utilize another group of presynaptic proteins: Rab3A interacting molecules (RIMs). RIMs are active zone proteins primarily expressed in neurons and are involved in several aspects of presynaptic function (Wang et al., 1997, Castillo et al., 2002, Schoch et al., 2002). There are 4 RIM genes (RIM1, RIM2, RIM3 and RIM4) with different expression patterns within the mouse brain. RIM1 and RIM2 both possess long α and β isoforms, while RIM2, RIM3 and RIM4 possess short γ isoforms (Kaeser et al., 2008, Wang et al., 2000). These proteins interact with multiple presynaptic active zone and synaptic vesicle proteins *in vivo* and are thought to act as molecular scaffolding proteins involved in organizing and modulating synaptic release machinery (Schoch et al., 2002, Wang et al., 2002, Wang et al., 1997, Wang et al., 2000, Betz et al., 2001, Coppola et al., 2001, Takao-Rikitsu et al., 2004, Ohtsuka et al., 2002). Their selective localization to active zones and its interactions with many presynaptic

molecules places RIM proteins in key positions to mediate presynaptic release and plasticity.

RIM1α modulates neurotransmitter release and is involved in presynaptically mediated plasticity. Mice lacking RIM1α display around a 50% reduction in probability of evoked neurotransmitter release (P_r) at the Schaffer-collateral to CA1 pyramidal neuron synapse in hippocampal slices (Schoch et al., 2002). This decrease in P_r is accompanied by an increase in PPF. Prolonged stimulation at 14 Hz reveals a lack of normal synaptic depression (Schoch et al., 2002). A later report suggests this is caused by an increase in the probability of release of individual synaptic vesicles in the RIM1α KO mouse during the first 4 or 5 responses (Calakos et al., 2004b). In addition, PTP is augmented in RIM1α KO mice (Schoch et al., 2002).

The PKA dependent mfLTP is absent in RIM1α-/- mice without affecting short term plasticity at that location (Castillo et al., 2002). A similar form of presynaptically expressed LTP at the parallel fiber/Purkinje cell synapse in the cerebellum is also absent in these mice (Castillo et al., 2002, Lonart et al., 2003). RIM1α-/- cerebellar cultures lack presynaptic LTP, which can be rescued by expression of wild-type RIM1α (Lonart et al., 2003).

Because of the PKA-dependence and presynaptic expression, one group hypothesizes that iLTD shares molecular mechanisms with other presynaptic, PKA-dependent forms of LTP such as mfLTP (Castillo et al., 2002). In another report, results suggests that RIM1α-/- mice do not exhibit iLTD but do retain other PKA-independent

forms of CB1 mediated short term plasticity, concluding that RIM1α is required for iLTD (Chevaleyre et al., 2007).

The behavioral effects of RIM1α deletion have been most thoroughly investigated by Dr. Craig Powell. In 2004 and 2010, he reported that RIM1α-/- mice had significant learning and memory deficits, social deficits and even schizophrenia-like phenotypes. These abnormalities include learning deficits in the Morris water maze (MWM) and both contextual and cued fear conditioning (Powell et al., 2004), decreased pre-pulse inhibition (Blundell et al., 2010b), increased locomotor response to novelty (Powell et al., 2004), deficits in social interaction with a juvenile (Blundell et al., 2010b), increased sensitivity to the non-competitive N-methyl-D-aspartic acid (NMDA) receptor antagonist MK-801 (Blundell et al., 2010b) and deficits in maternal behavior (Schoch et al., 2002).

Given RIM1's diverse functions and expression, attributing behavioral phenotypes in the RIM1α-/- mouse to the loss of RIM1α from specific neurons is difficult. Consequently, I obtained a conditional (floxed) *Rim1* knockout (RIM1f/f) mouse from Dr. Thomas Sudhof, and crossed it to previously characterized transgenic cre recombinase lines. Initially, I aimed to examine the behavioral effects of eliminating RIM1 selectively from 3 distinct neuronal populations: 1) dentate gyrus (DG) granule neurons, where it is required for mfLTP (Castillo et al., 2002) and thought to play a role in episodic-like/working memory (Hensbroek et al., 2003), 2) from CA3 pyramidal neurons, where it is required for multiple forms of presynaptic plasticity (Schoch et al.,

2002, Calakos et al., 2004a) and where I hypothesized it would play a role in the learning and memory deficits observed in the RIM1α-/- mouse, 3) from inhibitory interneurons of the forebrain (Yee et al., 2009, Kohwi et al., 2007) where it is required for iLTD, whose role in cognition and learning and memory is unknown. Unfortunately, none of the cre driver lines were as selective when crossed to the fRIM1 mutants as had been previously reported (Balthasar et al., 2004, McHugh et al., 2007, Nakazawa et al., 2002, Kohwi et al., 2007). In fact, the interneuron-directed cre recombinase driver line was removed completely from the study due to significant ectopic cre-mediated recombination.

Nevertheless, I observed that a subset of behaviors were altered in DG and CA3 selective RIM1 KOs that match with the global RIM1α-/- mouse, thereby narrowing the brain regions involved in some behaviors. Specifically, mice lacking RIM1 selectively in the DG, arcuate nucleus of the hypothalamus and select neurons of the cerebellum resulted in increased sensitivity to the psychotomimetic drug MK-801. The findings also suggest that loss of RIM1 in other brain regions or in multiple brain regions simultaneously may partially reproduce other behavioral abnormalities observed in RIM1α-/- mice.

Methods

Genetic manipulations

Mice homozygous for the floxed Rim1 allele (RIM1f/f) were generated as described previously (Kaeser et al., 2008). Briefly, 129Sv R1 stem cells containing the fRIM1 construct were injected into C57BL/6J blastocysts to produce chimeric mice which were crossed for one generation to C57BL/6J for germ line transmission. They were then crossed to transgenic mice expressing flp recombinase mice (which were generated by injecting the flp transgene-containing vector into a fertilized egg from a $B6SJLF_1/J$ X $B6SJLF_1/J$ cross (Dymecki, 1996)) and the resultant offspring were intercrossed to generate the homozygous fRIM1 mice. The WT, floxed, and recombined RIM1 alleles were genotyped by PCR with oligonucleotide primers as described previously (Kaeser et al., 2008). The pro-opiomelanocortin-cre (POMC-cre) mouse was generously provided by Joel Elmquist; it was generated in FVB/NJ mice and previously backcrossed 3 times to C57BL/6J as previously reported (McHugh et al., 2007, Balthasar et al., 2004). The kainate-cre (KA-cre) mouse was generously provided by Susumu Tonegawa; it was generated in C57BL/6J mice, crossed to the Roas26 reporter mouse (Soriano, 1999) and then subsequently backcrossed 8 times to C57BL/6J mice as previously reported (Nakazawa et al., 2002). In order to generate mice homozygous for the floxed RIM1 allele with either the POMC-cre transgene (fRIM1/POMC-cre+) or KA-cre transgene (fRIM1/KA-cre+) with sex-matched littermate controls (homozygous for floxed RIM1 allele without either cre transgene) I used the following 3-step breeding strategy. 1) Hemizygous POMC-cre+ or KA-cre+ mice were crossed with RIM1f/f mice. 2)

The resulting RIM1+/f, hemizygous cre+ mouse from cross 1 was crossed again with the RIM1f/f mouse. 3) The resulting RIM1f/f, hemizygous cre+ mouse from cross 2 was crossed a third time to the RIM1f/f mouse. This final cross provided sex-matched littermate pairs on a mixed genetic background that were homozygous for the floxed RIM1 allele and either hemizygous for one of the cre transgenes (fRIM1/cre+, experimental) or lacked a cre transgene (fRIM1/cre-, littermate control). Mice that displayed cre-mediated recombination in the tail DNA were excluded from the study.

Immunohistochemistry

Following transcardial perfusion of fRIM1/POMC-cre+/ROSA-YFP or fRIM1/KA-cre+/ROSA-YFP triple transgenic mice with first PBS and then 4% paraformaldehyde (Sigma; St. Louis, MO) in PBS, pH 7.4, whole brains were post-fixed in 4% paraformaldehyde in PBS, pH 7.4 at 4°C overnight. Brains were then transferred to 30% sucrose (Sigma) and allowed to equilibrate until they sank. 30µm sections were cut (HM 430 Sliding microtome, Microm; Waldorf, Germany) and stored at 4°C in PBS containing 0.1% sodium azide (Sigma) until use. Tissue sections were mounted onto positively charged glass slides (Fisher; Waltham, MA) and allowed to air dry. A 0.1M citric acid (Sigma) antigen unmasking treatment was performed prior to blocking slices with 3% normal donkey serum (NDS) (Jackson ImmunoResearch; West Grove, PA) in PBS containing 0.3% triton X-100 (Sigma). Overnight primary antibody incubation in 3% NDS, 0.3% Tween-20 (Sigma) in PBS at room temperature (Chicken anti-GFP 1:2000, Invitrogen, Carlsbad, CA; Mouse anti-NeuN 1:250, Mouse anti-Parvalbumin 1:400, and

Rabbit anti-Neurogranin 1:200, Millipore, Billerica, MA,) was followed by a 2 h secondary antibody treatment (Biotin-conjugated donkey anti-chicken, CY3-conjugated donkey anti-mouse or CY3-conjugated donkey anti-rabbit; Jackson ImmunoResearch). Amplification was performed using the Avidin Biotin Complex Kit (Vector Laboratories; Burlingame, CA) and a Tyramide Signal Amplification Kit (PerkenElmer; Waltham, MA). Images were taken on an Olympus BX51 epifluorescent microscope (Tokyo, Japan).

Radioactive In Situ Hybridization

Preparation of mouse tissues and embryos

Transgenic mice were transcardially perfused first with 10 ml of diethylpryocarbonate-PBS (DEPC-PBS) at 2 ml/min then with 10 ml of 4% paraformaldehyde in DEPC-PBS, pH 7.4 at 2 ml/min. Brains were dissected and post-fixed in 4% paraformaldehyde in DEPC-PBS, pH 7.4 for 16 h with rocking at 4°C before transfer to DEPC-saline. Tissues were then dehydrated, paraffin embedded, sectioned at 4 µm onto microscope slides treated with Vectabond (Vector Laboratories, Burlingame, CA). Slides were stored desiccated at 4°C.

Vector cloning and riboprobe synthesis

Riboprobe synthesis was performed with some variation to protocols published by the University of Texas Southwestern Medical Center (UTSW) Pathology Core (Shelton et al., 2000). Oligonucleotide sequences were used as primers to both amplify a 210 bp sequence of exon 6 from mouse RIM1 cDNA and create an EcoRI site at the 5' end and a Hind III site at the 3' end of the CPR product. (sense primer – 5' GCC GAA TTC

AAG GCT CCA GTT CTT TCA GAG C 3', anti-sense primer – 5' GCC AAG CTT GTC TTC AGC CAC CCT GCC ATC C 3') The amplified PCR product (containing bases 5-214 of exon 6) was then subcloned into pBluescript II KS (Stratagene, La Jolla, CA) at the EcoRI and Hind III sites. A positive clone was identified, verified by sequencing, and then linearized with either EcoRI or Hind III to synthesize ^{35}S-labeled sense and antisense riboprobes respectively by in vitro transcription with the Ambion Maxiscript kit (Ambion, Austin, TX) according to the kit instructions. Briefly, in 20 µl reactions, 200 ng of template DNA was transcribed with T7 (antisense) or T3 (sense) polymerase in the presence of 280 µCi of [α-^{35}S]-UTP (800 Ci/mmol) (Amersham, Piscataway, NJ) for 30 min at 37°C. After DN'ase digestion and termination of all enzymatic activity, the transcription products were suspended in final volumes of 75 µl (DEPC-H_2O) and purified over G-50 spin columns (5'–3', Boulder, CO). Pre- and post-column samples were assessed for quality by scintillation counting and denaturing polyacrylamide gel electrophoresis, and the remainder of the transcription products were stored at -80°C.

Prepared tissue and ^{35}S-labeled riboprobes were given to the UTSW pathology core for in situ hybridization, emulsion exposure and photomicroscopy. Their previously reported protocols were used and are described below (Shelton et al., 2000).

Riboprobe hybridization

For pre-hybridization, slides were heated to 58°C for 30 min. Utilizing RN'ase-free glass staining dishes and metal racks (Shandon, Pittsburgh, PA), slides were deparaffinized in xylene and hydrated through a series of graded ethanol/DEPC-saline

rinses (95%, 85%, 60%, 30%) to DEPC-saline. To accomplish microwave RNA retrieval, the slides were transferred to upright plastic racks and immersed in plastic containers (Miles Tissue-Tek, Elkhart, IN) filled with DEPC-1X Antigen Retrieval Citra pH 6.0 (Biogenex, San Ramon, CA). Empty slots were filled with blank slides, and the plastic slide dish was covered loosely. The slides were heated in a 750 watt microwave at 90% power for 5 min. Any evaporated solution was replaced with DEPC-H_2O, and the container was heated at 60% power for an additional 5 min. The slides were cooled for 20 min, then returned to their metal racks and washed twice in DEPC-PBS, pH 7.4, for 5 min each. Subsequently, the slides were fixed for 20 min in 4% paraformaldehyde/DEPC-PBS, pH 7.4, and washed twice in DEPC-PBS, pH 7.4, for 5 min each. To further unmask RNA, the slides were permeabilized for 7.5 min with 20 µg/ml pronase-E in 50 mM Tris-HCl, pH 8.0/5 mM EDTA, pH 8.0/ DEPC-H_2O. Excess pronase-E was removed by a 5-min DEPC-PBS, pH 7.4 wash before re-fixing in 4% paraformaldehyde/ DEPCPBS, pH 7.4, for 5 min. Slides were washed in DEPC-PBS, pH 7.4, for 3 min. The slides were then acetylated in 0.25% acetic anhydride/ 0.1 M triethanolamine–HCl, pH 7.5, twice for 5-min. Next, the slides were equilibrated in 1 X SSC, pH 7.0, for 5 min followed by incubation in 50 mM n-ethylmaleimide/1 X SSC, pH 7.0, for 20 min. Five-min washes in DEPC-PBS, pH 7.4, and DEPC-saline followed and then the slides were dehydrated through graded ethanol/DEPC-saline rinses (30%, 60%, 85%, 95%) to absolute ethanol, and dried under vacuum for 2 h.

Riboprobes and hybridization mixture containing 50% formamide, 0.3 M NaCl, 20 mM Tris-HCl, pH 8.0, 5 mM EDTA, pH 8.0, 10 mM $NaPO_4$, pH 8.0, 10% dextran sulfate, 1 X Denhardt's, and 0.5 mg/ml tRNA were thawed from -80°C storage. Probes were diluted in aliquots of hybridization mixture sufficient to achieve 7.5 X 10^3 cpm/µl and the mixture heated to 95°C for 5 min. Diluted probes were then cooled to 37°C and 1 M DTT was added to achieve a final concentration of 10 mM DTT. Riboprobe was applied directly over the section, and slides were placed in a Nalgene utility box lined with 5 X SSC/50% formamide-saturated gel blot paper. Each slide was coverslipped with parafilm. The box was sealed and slides were hybridized for 14 h at 55°C.

After hybridization, parafilm coverslips were removed and the slides were placed in upright plastic racks and immersed in a 5 X SSC/10 mM DTT wash at 55°C for 40 min. Subsequently, the slides were washed for 30 min at 65°C in HS (2 X SSC/50% formamide/100 mM DTT), followed by three 10-min washes in NTE (0.5 M NaCl/10 mM Tris-HCl, pH 8.0/5 mM EDTA, pH 8.0) at 37°C. Slides were transferred to a fourth NTE wash containing RN'ase-A (2 µg/ml) and incubated 30 min at 37°C. Excess RN'ase-A was removed in a fifth NTE wash for 15 min at 37°C, before the slides were returned to HS for another 30 min at 65°C. After this second HS, the slides were washed for 15 min at 37°C each in 2 X SSC and 0.1 X SSC. Finally, the slides were dehydrated in graded ethanol rinses (30%, 60%, 85%, and 95%) to absolute ethanol, and dried under vacuum.

Emulsion exposure and Photomicroscopy

Dried slides were dipped in dilute Ilford K.5 nuclear emulsion (Polysciences, Warrington, PA) pre-warmed to 42°C. Slides were hung vertically and slowly dried at room temperature at 75% humidity for 3 h. The slides were placed into 25-count microscope slide storage boxes with desiccant. The boxes were sealed with tape, wrapped with foil, and placed at 4°C. After 28 days autoradiographic exposure, the slides were developed in D19 (Eastman Kodak, Rochester, NY) at 14°C and the latent image was fixed with Kodak Fixer. The slides were thoroughly rinsed, counterstained with hematoxylin (Richard-Allen, Kalamazoo, MI), dehydrated, and coverslipped with permanent mounting media.

Visualization of MTP expression was achieved with a Leitz Laborlux-S microscope stand equipped with Plan-EF optics, a standard bright-field condenser, and a Mears low-magnification darkfield condenser. Photomicrographic record was made with an Optronics VI-470 CCD camera and a Power Macintosh G3 equipped with a Scion CG-7 frame grabber and Scion Image 1.62 software.

Quantitative Reverse Transcriptase Polymerase Chain reaction

Rapid tissue harvesting for quantitative reverse transcriptase polymerase chain reaction (qRT-PCR) was performed in chilled dissection solution (26 mM $NaHCO_3$, 212.7 mM Sucrose, 2.6 mM KCL, 1.23 mM NaH_2PO_4, 10 mM Dextrose, 3 mM $MgCl_2 \bullet 6(H_2O)$, 1 mM $CaCl_2 \bullet 2(H_2O)$) and stored at -80°C until mRNA was extracted with Trizol (Invitrogen). Reverse transcription of the mRNA library was performed using Superscript III 1st strand synthesis kit (Invitrogen). SYBR GreenER qPCR SuperMix Universal Kit

(Invitrogen) was used for qRT-PCR according to manufacturer's instructions. Each tissue sample was tested in triplicate and their Ct values were averaged together. Oligonucleotide primers were designed to create a 105 bp product spanning portions of exons 5 and 6 of the RIM1 mRNA transcript (forward primer – AAGCAGGCATCAAGGTCAAG, reverse primer – ACGTTTGCGCTCACTCTTCT). The neuron specific microtubule associated protein 2 (MAP2) was used as a reference gene (Sundberg et al., 2006, Mukaetova-Ladinska et al., 2002) (forward primer – ACTTGACAATGCTCACCACGTA, reverse primer – CCTTTGCATGCTCTCTGAAGTT). The relative change of RIM1 transcript between experimental and control tissue was normalized to MAP2 transcript levels using standard calculation methods (Pfaffl, 2001). To test if the normalized relative change in RIM1 transcript levels were significantly different from unity (no change) a one sample t-test was employed.

Behavioral Overview

Mice were housed 2 per cage (always littermate pairs but not always WT and cKO pairs) and maintained on a light/dark cycle with light on from 6 A – 6 P in a 22 ± 2°C (30%-70% humidity) housing room. All behavioral tests were performed in the afternoon. For both fRIM1/POMC-cre+ and fRIM1/KA-cre+ mice, fRIM1/cre- sex-matched littermates were used as WT controls to ensure a constant genetic background. Food (normal chow) and water were available *ad libitum* for the duration of the behavioral battery. Sex-matched littermate pairs ranged from 3-8 months of age at the onset of behavioral testing and all behaviors were completed within 8 weeks. 2

cohorts of fRIM1/POMC-cre (N=12 and N=8 littermate pairs, total N=20 littermate pairs; littermate pairs age range at onset of behavior: 3 mo, 3 pairs; 4 mo, 3 pairs; 6 mo, 10 pairs; 7 mo, 1 pair; 8 mo, 3 pairs) and 2 cohorts of fRIM1/KA-cre (N=10 and N=10 littermate pairs, total N=20 littermate pairs; littermate pairs age range at onset of behavior: 3 mo, 5 pairs; 4 mo, 4 pairs; 5 mo, 4 pairs; 6 mo, 3 pairs; 7 mo, 4 pairs) were tested separately and pooled for analysis (except for rotarod, startle threshold, PPI and locomotor response to psychotomimetics in which only one of the cohorts was tested). In total, 13 male and 7 female fRIM1/KA-cre littermate pairs and 9 male and 11 female fRIM1/POMC-cre littermate pairs were tested. Behaviors were done in the following order: elevated plus maze, dark/light, open field, locomotor, social interaction in the open field, accelerating rotarod, startle threshold, prepulse inhibition, fear conditioning, Morris water maze and locomotor response to MK-801. Mice were allowed 1 h to habituate to the testing room prior to beginning experiments. All tests were done in accordance with Institutional Animal Care and Use Committee and UT Southwestern Medical Center animal guidelines and protocols.

Elevated Plus Maze – Performed essentially as described previously (Powell et al., 2004). Mice were placed in the center of a black plexiglass elevated plus maze (each arm 33 cm in length and 5 cm wide, with 25 cm high walls on closed arms) in a dimly lit room for 5 min. 2 mazes were used and video-tracked simultaneously (Ethovision 2.3.19, Noldus; Wageningen, The Netherlands). A barrier was set between the mazes to prevent mice from seeing each other. Time spent in open and closed arms, number of open and

closed entries, and time in the middle was calculated. 5 fRIM1/POMC-cre and 1 fRIM1/KA-cre mice were excluded from analysis because either the experimental or control mouse fell from the platform during testing.

Dark/Light – Performed essentially as described previously (Powell et al., 2004). Apparatus is a 2 compartment opaque plexiglass box (25 cm x 26 cm in each compartment). One side is black and kept closed and dark, while the other is white with a fluorescent light directly above its open top (1700 lx). Mice were placed in the dark side for 2 min, then the divider between the two sides was removed allowing the mouse to freely explore both chambers for 10 min. Anxiety like behavior is measured as latency to enter the light side, as well as time spent in the light vs. dark compartments. Measures were taken using photobeams and MedPC software (Med Associates; St. Albans, VT).

Open Field – Performed essentially as described previously (Powell et al., 2004). The open field test was performed for 10 min in a brightly lit, 48 x 48 x 48 cm white plastic arena using the Ethovision video-tracking software (Noldus). Time spent in the center zone (15 x 15 cm) and frequency to enter the center was recorded. Locomotor activity was also measured during the open field test.

Locomotor – Mice were placed in a fresh home cage with minimal bedding for a 2 hour testing period. Lengthwise horizontal locomotor activity was tested in 5 minute bins for the duration of the task using photobeams linked to computer data acquisition software (San Diego Instruments, San Diego, CA). Beams were organized linearly along one

horizontal axis in 5 cm increments and total beam breaks was used as the dependent variable.

Social Interaction in the open field – Performed essentially as described previously (Blundell et al., 2010a). The test was performed in a 48 cm × 48 cm white plastic arena under red light using a 6.0 cm × 9.5 cm perforated plexiglass rectangular cage containing an unfamiliar adult mouse, allowing olfactory, visual, and minimal tactile interaction. Mice were first placed in the arena for 5 min with the empty clear plexiglass cage. Then mice were allowed to interact with a novel caged social target for another 5 min. Time spent in the interaction zone was obtained using Ethovision video-tracking software (Noldus).

Accelerating Rotarod – Performed essentially as described previously (Powell et al., 2004). A 5-lane accelerating rotarod designed for mice (IITC Life Science; Woodland Hills, CA) was used (rod diameter was 3.2 cm; rod length was 10.5 cm). The rotarod was activated after placing mice on the motionless rod. The rod accelerated from 0 to 45 revolutions per min in 60 s. Time to fall off the rod was measured.

Startle Threshold and Pre-Pulse Inhibition – Both of these tasks were performed as described previously (Etherton et al., 2009). The **pre-pulse inhibition** (PPI) test began with six presentations of a 120 dB pulse to calculate the initial startle response. Afterward, the 120 dB pulse alone, prepulse/pulse pairings of 4, 8, or 16 dB above 70 dB background followed by the 120 dB pulse with a 100 ms delay, or no stimulus were presented in pseudorandom order. For the **startle threshold** test, mice were presented

with 6 trial types of varying intensity (No Stimulus or 80, 90, 100, 110, or 120 dB pulses – eight presentations of each). Mean startle amplitudes for each condition were averaged.

Fear Conditioning – Performed essentially as described previously (Powell et al., 2004). Mice were placed in clear plexiglass shock boxes (Med Associates) for 2 min, and then two, 90 dB acoustic conditioned stimuli (CS; white noise, each 30 seconds in duration and separated by a 30 second delay) were played. Each CS co-terminated in a 2 s, 0.5 mA foot shock unconditioned stimulus (US). Mice remained in the chamber for 2 min after the second pairing before returning to their home cages. Freezing behavior (motionless except respirations) was monitored at 5 s intervals by an observer blind to the genotype. To test contextual learning 24 hr later, mice were returned to the same training context and scored for freezing in the same manner. To assess cue-dependent fear conditioning, mice were placed in a novel environment with an unfamiliar vanilla odor in the afternoon following the contextual test. Freezing was measured first during a 3 min baseline period then during 3 minutes with the CS playing.

Morris water maze – The MWM and visible platform tests were performed as described previously (Powell et al., 2004) except the probe trial was performed only on day 9. Briefly, a 1.22-meter-diameter, white, plastic, circular pool was filled with opaque water (22°C ± 1°C) in a room with prominent extra-maze cues. Mice were trained with 4 trials/day with an inter-trial interval of 1–1.5 min for 8 consecutive days. Mice were placed in one of four starting locations and allowed to swim until they found the submerged platform or until a maximum of 60 s had elapsed. Latency to reach the

platform, distance traveled to reach the platform, swim speed, and percent thigmotaxis (time spent near the wall of the pool) were measured using the Ethovision video-tracking software (Noldus). A probe trial (free swim with the submerged platform removed) was performed on day 9. The % time spent in the target quadrant and the # of platform location crossings were measured. The **visible water maze** task was conducted similarly to the traditional Morris water maze with a few changes. A visible cue (black foam cube) was placed on top of the platform. The starting location was held constant while the platform location was moved for each trial. Mice were given 6 trials/day for 2 consecutive days, and the latency to reach the visible platform was measured.

Locomotor response to psychotomimetics – The apparatus and methods described for the locomotor test were also used to measure locomotion in this task. The test was performed as described in Blundell, et al. 2010 (Blundell et al., 2010b). Briefly, at the beginning of each hour of a 3 hr locomotor session, mice were given a ~0.2 ± 0.1 cc intra-peritoneal injection of saline (time 0), 0.1 mg/kg MK-801 (1 h), 0.2 mg/kg MK-801 (2 h). Because fRIM1/KA-cre+ showed increased locomotion to novel environments, they underwent 3 days of this protocol (receiving only saline injections) to habituate prior to the actual testing on day 4.

Statistics

I used genotype and sex as independent variables for all behavioral tests and performed 2-way ANOVAs for statistical analysis. Where applicable, time (locomotion tasks), trial (rotarod and visual MWM tasks), day (MWM training) or intensity (PPI and

startle threshold) were included as independent variables and a 3-way ANOVA with repeated measures was performed. In the MWM probe trial, genotype, sex and location were included as independent variables and a 3-way ANOVA was performed. A student's t-test was used for the planned comparisons analysis in the locomotor tasks and the MWM probe trial. I used Statistica (StatSoft, Inc., Tulsa, OK) for statistical analysis and significance was always taken as $p < 0.05$.

Chapter 1, Section 2

Experimental Findings

fRIM1/POMC-cre+ results in *Rim1* deletion in dentate gyrus, arcuate nucleus and select neurons of the cerebellum

I first crossed fRIM1 mice to a transgenic cre line driven by the POMC (preproopiomelanocortin) promoter (POMC-cre). This particular POMC-cre line was previously reported to induce recombination selectively in DG granule neurons as well as the arcuate nucleus of the hypothalamus (Balthasar et al., 2004, McHugh et al., 2007). Recombination was reported to begin at 2-3 weeks of age and to remain spatially restricted into adulthood. Assessing the location of RIM1 knockout is particularly challenging due to the absence of antibodies that function selectively in immunohistochemistry (IHC) and the high degree of homology between Rim1 and Rim2. Thus, I first crossed in the previously described yellow fluorescent protein (YFP) expressing conditional Rosa reporter transgenic line (R26R-YFP) (Soriano, 1999, Lagace et al., 2007) to obtain fRIM1/POMC-cre+/R26R-YFP mice to label cre recombinase activity in the presence of fRIM1.

IHC staining for YFP in the fRIM1/POMC-cre+/R26R-YFP mice revealed successful cre-mediated recombination largely limited to the DG granule neurons, select neurons in the granule and molecular layers of the cerebellum, and arcuate nucleus (Figure 1.1a-c). Co-staining for a neuronal marker, neuronal nuclei protein (NeuN), revealed that cre-mediated recombination in DG neurons was robust, but

somewhat mosaic. Interneurons in the stratum radiatum, stratum lacunosum-moleculare, and stratum lucidum of the hippocampus and in the hilus region did not undergo cre-mediated recombination, nor did pyramidal neurons in area CA3 or CA1 (Figure 1.1d-f). The YFP staining pattern in cerebellum suggested cre-mediated recombination restricted to neurons of the granular and molecular layers without involvement of Purkinje Cells (Figure 1.2a-c). In the molecular layer, consisting largely of interneurons, this was confirmed by co-staining for parvalbumin-containing interneurons demonstrating that almost all of YFP-positive neurons in this layer were also positive for the inhibitory interneuron marker parvalbumin, though cre-mediated recombination did not occur in all parvalbumin positive neurons (Figure 1.2d-f). The cerebellar granular layer largely consists of granule neurons making mosaic staining for YFP in this region most likely to be in granule cells. To rule out Golgi cells, another common neuron type in the granule cell layer (GL), as responsible for the YFP expression in the GL, I co-stained for the Golgi cell marker neurogranin (Singec et al., 2003). Essentially none of the YFP positive cells co-stained for neurogranin (data not shown), making it most likely that the YFP-positive neurons in this region represent mosaic cre recombination in granule cells of the cerebellum.

To address whether levels of RIM1 transcript were decreased in YFP+ brain regions, I performed quantitative reverse transcription polymerase chain reaction (qRT-PCR) using primers that bind RIM1 transcripts on either side of the exon 5 – exon 6 junction. I analyzed RIM1 transcript levels in fRIM1/POMC-cre+ and fRIM1/POMC-cre-

control tissue from cortex, cerebellum and 3 hippocampal regions: DG, CA3, and CA1 (Figure 1.3). Consistent with cre-mediated recombination data, I found RIM1 transcripts to be decreased by 43.89 % in the DG (SEM = ±7.48 %, $p < 0.05$) and 24.39 % in the cerebellum (SEM = ±8.97 %, $p < 0.05$) in fRIM1/POMC-cre+ mice compared to controls.

fRIM1/KA-cre+ results in *Rim1* deletion in CA3 pyramidal neurons as well as mosaic deletion in dentate gyrus and other brain regions.

I next crossed fRIM1 mice to a transgenic cre line driven by the KA-1 (a kainate receptor subunit) promoter (KA-cre). This KA-cre line was previously shown to selectively induce recombination in CA3 pyramidal neurons, 10 % of DG granule neurons and cerebellar granule neurons, as well as 50% of facial nerve nuclei of the hindbrain (Nakazawa et al., 2002). In area CA3, recombination was first observed at 2 weeks of age with 100% of CA3 pyramidal neurons recombined by 8 weeks. Again, I crossed in the previously described conditional R26R-YFP mouse (Soriano, 1999, Lagace et al., 2007) to generate fRIM1/KA-cre+/R26R-YFP mice which would label cre recombinase activity in the presence of fRIM1.

IHC staining for YFP in the fRIM1/KA-cre+/R26R-YFP mice revealed robust cre-mediated recombination in area CA3 of the hippocampus, and mosaic recombination in DG, cortex, thalamus, and cerebellum (Figure 1.1g-i). I did not observe robust staining in the facial nerve nuclei (data not shown). Co-staining for the neuronal marker NeuN revealed that cre-mediated recombination in virtually all CA3 pyramidal neurons, hilus region neurons, and in a small fraction of DG granule neurons (Figure 1.1j-l). Interneurons in the stratum radiatum and stratum lacunosum-moleculare of the

hippocampus and area CA1 pyramidal neurons did not undergo cre-mediated recombination (Figure 1.1j-l). I also observed YFP staining in cerebellar purkinje cells and mosaically in neurons of the cerebellar granule layer (Figure 1.2g-i).

Using qRT-PCR, I measured RIM1 transcript levels in the fRIM1/KA-cre+ mice in the same 5 brain regions analyzed in the fRIM1/POMC-cre+ mice (Figure 1.3). RIM1 transcript levels were decreased by 58.86 % in the DG (SEM = ±12.83 %, $p < 0.05$) and 67.02 % in area CA3 (SEM = ±7.96 %, $p < 0.05$) of fRIM1/KA-cre+ mice compared to controls.

In Situ hybridization of RIM1 transcripts

In addition to immunohistochemistry and qRT-PCR I also attempted to validate knockdown of RIM1 transcripts in both of the conditional RIM1 knockout lines using emulsion *in situ* hybridization. Specifically, an ^{35}S labeled antisense riboprobe (110 bp) complimentary to exon 6 of the RIM1 transcript, was hybridized with paraffin embedded brain tissue from WT, global RIM1α-/-, fRIM1/cre-, fRIM1/POMC-cre+ and fRIM1/KA-cre+ mice. The analogous sense riboprobe was used as a negative control on a WT mouse (Figure 1.4). The antisense probe on WT tissue revealed RIM1 expression to be almost ubiquitous in the mouse brain, while the absence of signal on the KO tissue suggests that the antisense probe is highly specific for RIM1 transcript (Figure 1.4a-b). The absence of signal using the sense probe on WT tissue suggests a low level of background signal with high specificity for RIM1 transcript (Figure 1.4d). The fRIM1/cre- tissue has similar RIM1 expression to the WT mouse, suggesting that the floxed gene has

no effect on RIM1 expression (Figure 1.4c). Finally, in both the fRIM1/POMC-cre+ and fRIM1/KA-cre+ tissue I observed some unexpected patterns of RIM1 signal (Figure 1.4e and 1.4f respectively). In the fRIM1/POMC-cre+ mouse there is an increase in signal in the dentate gyrus, molecular layer of the cerebellum and other scattered neurons. In the fRIM1/KA-cre+ mouse I observed an increase in signal in area CA3 of the hippocampus, dentate gyrus, and thalamus. These results are in contrast to the decrease in RIM1 transcript I expected to see in those areas. However, the brain regions showing the increased signal in the in situ hybridization experiment correspond well with the brain regions showing cre-mediated recombination in the fRIM1/cre+/ROSA-YFP reporter mice. Furthermore, this result was replicated when I performed qRT-PCR experiments using primers that bind RIM1 transcript specifically in exon 6 (data not shown). Though I was unable to identify the exact transcript that seems to be upregulated in the fRIM1/cre+ mice, the data suggest that full length RIM1 transcripts are decreased as no known splice variants of RIM1 exist that do not contain exon 5 (Wang et al., 2000). One possibility is that after cre-mediated recombination exon 6 is still able to be transcribed under a new promoter, separate from the first part of the RIM1 gene. Attempts at understanding this phenomenon were unsuccessful.

POMC-cre-mediated loss of RIM1 in dentate gyrus, selected cerebellar neurons and arcuate nucleus leads to increased locomotor responses to MK-801

Previous work demonstrated that RIM1α-/- mice had severe abnormalities including schizophrenia-related deficits (Blundell et al., 2010b), learning and memory deficits (Powell et al., 2004), decreased maternal behavior (Schoch et al., 2002) and

social interaction abnormalities (Powell et al., 2004). To test whether RIM1 loss from the DG, select neurons of the cerebellum, and arcuate nucleus in the fRIM1/POMC-cre+ mice was sufficient to induce any of the behavioral abnormalities observed in the RIM1α-/- mice, I put the fRIM1/POMC-cre+ mice with sex-matched littermate controls through many of the same behavioral tasks.

When I tested the locomotor enhancing effects of MK-801, I found that the fRIM1/POMC-cre+ mice mimicked the global RIM1α-/-. Specifically, there is no change in locomotion when injected with saline (Figure 1.5a; 3-way mixed ANOVA with repeated measures; main effect of genotype, $F_{(1,12)} = 1.09$, p = 0.32; main effect of time, $F_{(11, 132)} = 15.76$, $p < 0.0001$; main effect of sex, $F_{(1,12)} = 0.004$, $p = 0.95$; genotype x time interaction, $F_{(11, 132)} = 0.60$, $p = 0.83$; genotype x sex interaction, $F_{(1,12)} = 0.38$, $p = 0.55$; time x sex interaction, $F_{(11, 132)} = 0.60$, $p = 0.83$; genotype x time x sex interaction: $F_{(11,132)} = 0.74$, $p = 0.69$) and no change in locomotion at the low 0.1 mg/kg MK-801 dose (Figure 1.5a; main effect of genotype, $F_{(1,12)} = 1.93$, $p = 0.19$; main effect of time, $F_{(11, 132)} = 5.11$, $P < 0.0001$; main effect of sex, $F_{(1,12)} = 1.03$, $p = 0.33$; genotype x time interaction, $F_{(11, 154)} = 0.84$, $p = 0.60$; genotype x sex interaction, $F_{(1,12)} = 5.05$, $p < 0.05$; time x sex interaction, $F_{(11, 132)} = 0.80$, $p = 0.64$; Sex x Genotype x Bin Interaction, $F_{(11,132)} = 0.68$, $p = 0.75$). However, there is a significant interaction between genotype and time during the hour following the higher 0.2 mg/kg MK-801 dose demonstrating that the response to this higher dose of MK-801 is different between the two genotypes (Figure 1.5a; main effect of genotype, $F_{(1,12)} = 4.39$, $p = 0.06$; main effect of time, $F_{(11, 132)} = 22.02$, $p < 0.0001$;

main effect of sex, $F_{(1,12)} = 0.13$, $p = 0.73$; genotype x time interaction, $F_{(11, 132)} = 2.07$, $p < 0.05$; genotype x sex interaction, $F_{(1, 12)} = 0.002$, $p = 0.99$; time x sex interaction, $F_{(11, 132)} = 0.20$, $p = 0.997$; genotype x time x sex interaction, $F_{(11, 132)} = 0.38$, $p = 0.96$). Planned comparison analysis identified that mutant mice were significantly different from littermate controls following the 0.2 mg/kg MK-801 injection. These planned comparisons indicated that fRIM1/POMC-cre+ mice are significantly more active beginning 20 minutes after injection ($p < 0.05$) and begin returning toward control levels of locomotion 50 minutes following the injection.

When I tested the fRIM1/POMC-cre+ mice for other abnormalities found in the RIM1α-/- mice including locomotion to novelty (Figure 1.6a), PPI (Figure 1.7b), MWM (Figure 1.8a-c), fear conditioning (Figure 1.9a), and social interaction (Figure 1.9b) I observed no differences compared to littermate controls. I also tested these mice for changes in startle response (Figure 1.7a and c), and anxiety-related behaviors (dark/light box, elevated plus maze, open field; Figure 1.10a, c, e respectively), and accelerating rotarod (data not shown), but found no change in any of these behaviors.

KA-cre-mediated loss of RIM1 in CA3 of hippocampus and mosaic loss in dentate gyrus and other brain regions leads to hyperactivity to novelty

I tested the fRIM1/KA-cre+ mice with sex-matched littermate controls in the same behavioral tasks as the fRIM1/POMC-cre+ mice. fRIM1/KA-cre+ mice mimicked RIM1α-/- mice only in their hyperactivity during a 2 hour test of locomotion (Figure 1.6b; 3-way mixed ANOVA; main effect of genotype, $F_{(1, 36)} = 7.79$, $p < 0.01$; main effect of time, $F_{(23, 828)} = 61.68$, $p < 0.001$; main effect of sex, $F_{(1, 36)} = 0.48$, $p = 0.49$; genotype x

time interaction, $F_{(23, 828)}$ = 1.17, p = 0.27; genotype x sex interaction, $F_{(1, 36)}$ = 0.47, p = 0.50; time x sex interaction, $F_{(23, 828)}$ = 0.63, p = 0.91; genotype x time x sex, $F_{(23, 828)}$ = 0.38, p = 0.997). When I evaluated the first 10 min of locomotor activity in the same environment over 4 days, their locomotor activity diminished until it was equal to littermate controls (Figure 1.6c; 3-way mixed ANOVA; main effect of genotype, $F_{(1,16)}$ = 0.52, p = 0.48; main effect of day, $F_{(3, 48)}$ = 13.44, p < 0.0001; main effect of sex, $F_{(1,16)}$ = 0.05, p = 0.83; genotype x day interaction, $F_{(3, 48)}$ = 3.12, P < 0.05; genotype x sex interaction, $F_{(1,16)}$ = 0.30, p = 0.59; day x sex interaction, $F_{(3, 48)}$ = 1.67, p = 0.19; genotype x day x sex interaction, $F_{(3,48)}$ = 1.34, p = 0.27; student's t-test was used for a planned comparison on Day 1, p < 0.05). Similar to RIM1α-/- mice, in order to test the locomotor response to MK-801 in the fRIM1/KA-cre+ mice, I had to habituate the fRIM1/KA-cre+ mice to the MK-801-induced locomotor task protocol for 3 days using only saline injections (Figure 1.5b). On the fourth day, I followed the same MK-801-induced locomotor activity protocol performed on the fRIM1/POMC-cre+ mice. In this case, however, I saw no difference between fRIM1/KA-cre+ mice and littermate controls (Figure 1.5c), providing a double dissociation between locomotor response to novelty (in fRIM1/KA-cre+ but not fRIM1/POMC-cre+ mice) and locomotor response to the psychotomimetic MK-801 (in fRIM1/POMC-cre+ but not fRIM1/KA-cre+ mice).

I also tested the fRIM1/KA-cre+ mice in startle threshold and PPI (Figure 1.7d-f), MWM (Figure 1.8d-f), fear conditioning (Figure 1.9c), social interaction in the open field

(Figure 1.9d), anxiety tests (Figure 1.10d, d and f) and accelerating rotarod (data not shown). In all of these tests, the fRIM1/KA-cre+ mice were not different from controls.

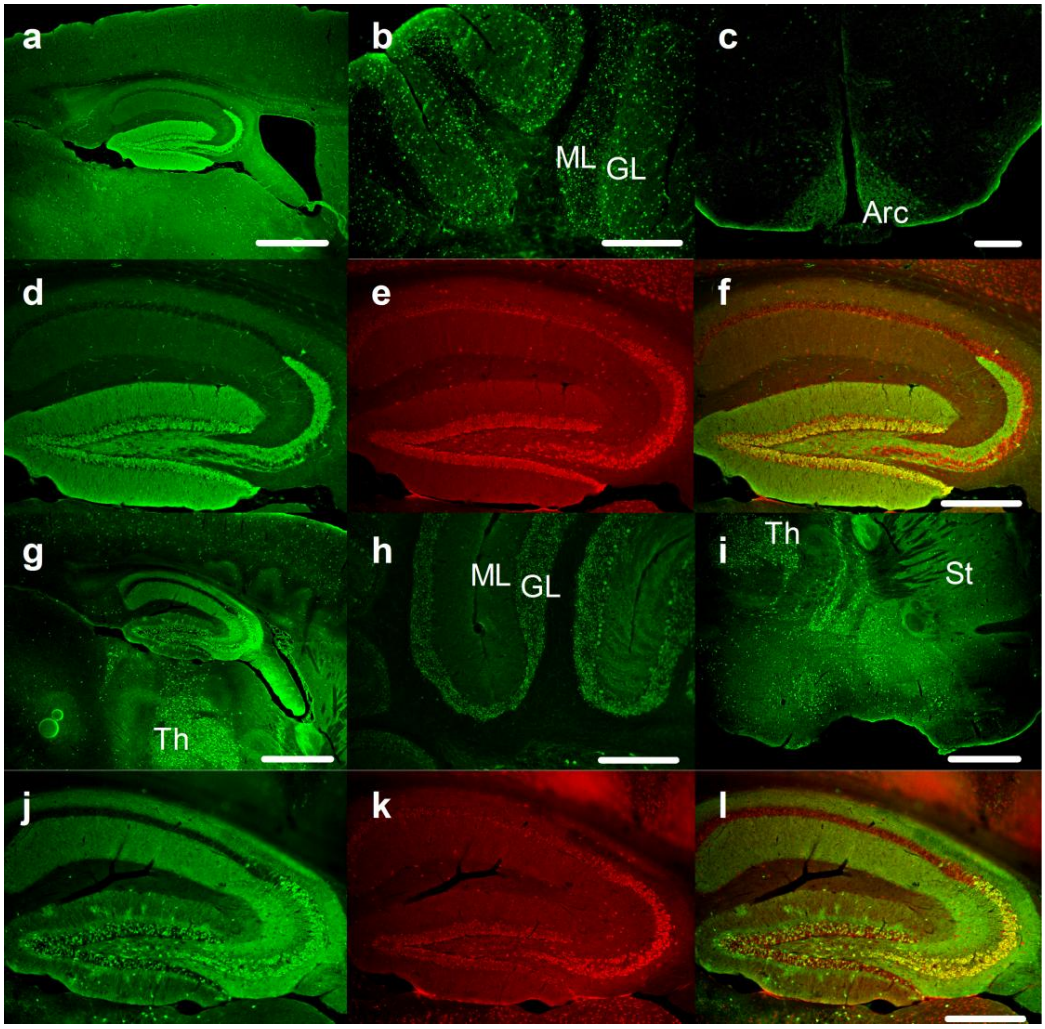

FIGURE 1.1 Immunofluorescent signal reveals regional specificity of the fRIM1/POMC-cre+/R26R-YFP and fRIM1/KA-cre+/R26R-YFP reporter mice. (Green – Anti-YFP, Red – Anti-NeuN) YFP expression in fRIM1/POMC-cre+/R26R-YFP brain tissue from hippocampus **(a)**, cerebellum **(b),** and hypothalamus **(c)**. YFP and NeuN expression in a fRIM1/POMC-cre+/R26R-YFP hippocampus **(d-f)**. FP expression in fRIM1/KA-cre+/R26R-YFP brain tissue from hippocampus **(g)**, cerebellum **(h)** and forebrain **(i)**. YFP and NeuN expression in a fRIM1/KA/R26R-YFP hippocampus **(j-k). f and l** are merges of **d-e and j-k** respectively. **(a**, **h and i**, scale bar = 1 mm. **b, d-f, h and j-k**, scale bar = 500 µm. **c**, scale bar = 250 µm. ML, molecular layer; GL, granule layer; Th, thalamus; St, striatum)

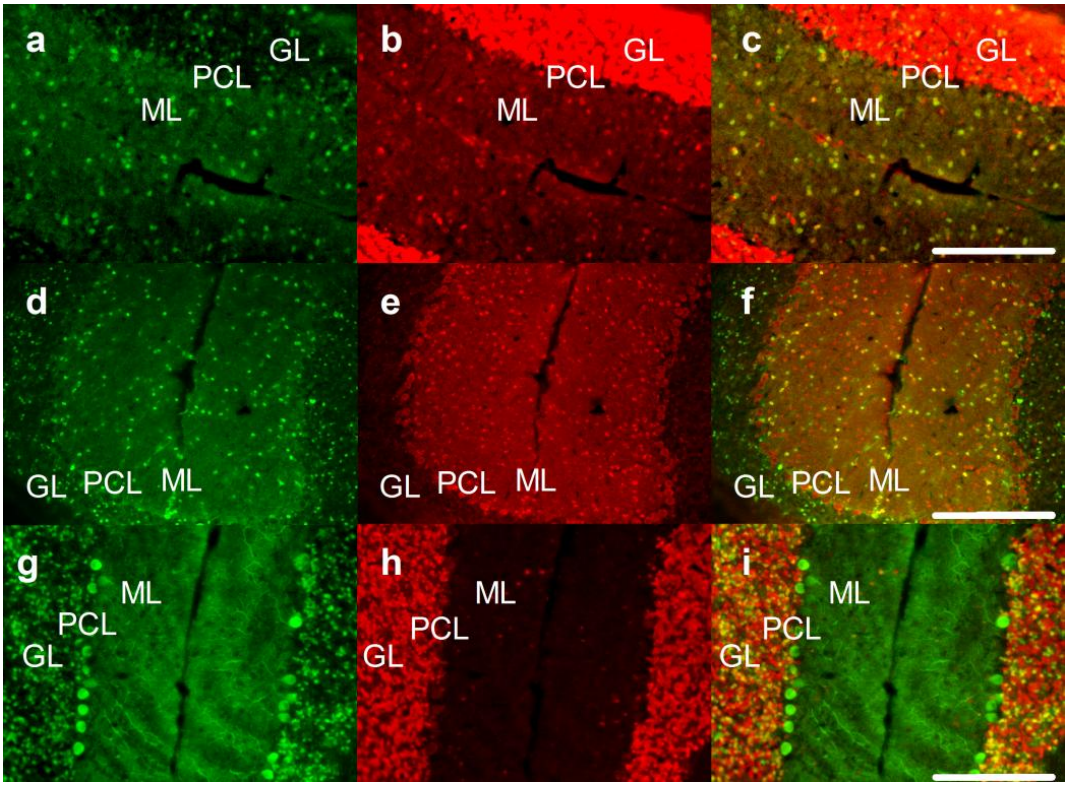

FIGURE 1.2 Cell specific cre-mediated recombination in fRIM1/POMC-cre+/R26R-YFP and fRIM1/KA-cre+/R26R-YFP cerebellum. (Green - Anti-YFP, red - Anti-NeuN or Anti-Parvalbumin as labeled) **a-c.** High magnification of YFP and NeuN expression in the cerebellum of a fRIM1/POMC-cre+/R26R-YFP mouse. **d-f.** High magnification of YFP and Parvalbumin expression in the cerebellum of a fRIM1/POMC-cre+/R26R-YFP mouse. **g-i.** High magnification of YFP and NeuN expression in the cerebellum of a fRIM1/KA-cre+/R26R-YFP mouse. **c, f and i** are merges of **a-b, d-e and g-h** respectively. (All scale bars = 250 µm. GL-granule layer, PCL-Purkinje Cell Layer, ML-Molecular Layer.)

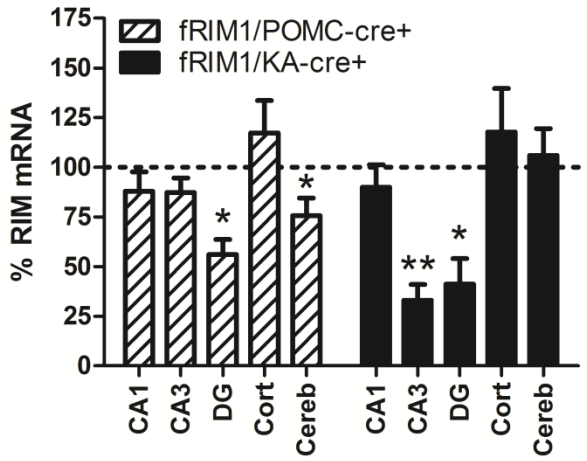

FIGURE 1.3 Regional specificity of fRIM1/POMC-cre+ and fRIM1/KA-cre+ conditional knockouts by qRT-PCR. Quantitative RT-PCR was used to measure levels of RIM1 transcript in the CA1, CA3 and dentate gyrus regions of the hippocampus as well as cortex and cerebellum in the fRIM1/POMC-cre+ and fRIM1/KA-cre+ mice compared to their littermate controls. RIM1 transcript levels were internally normalized to MAP2 transcript levels and reported as a percentage of normalized RIM1 transcript levels observed in littermate controls (dashed line). (*****, $p < 0.05$; ******, $p < 0.01$,)

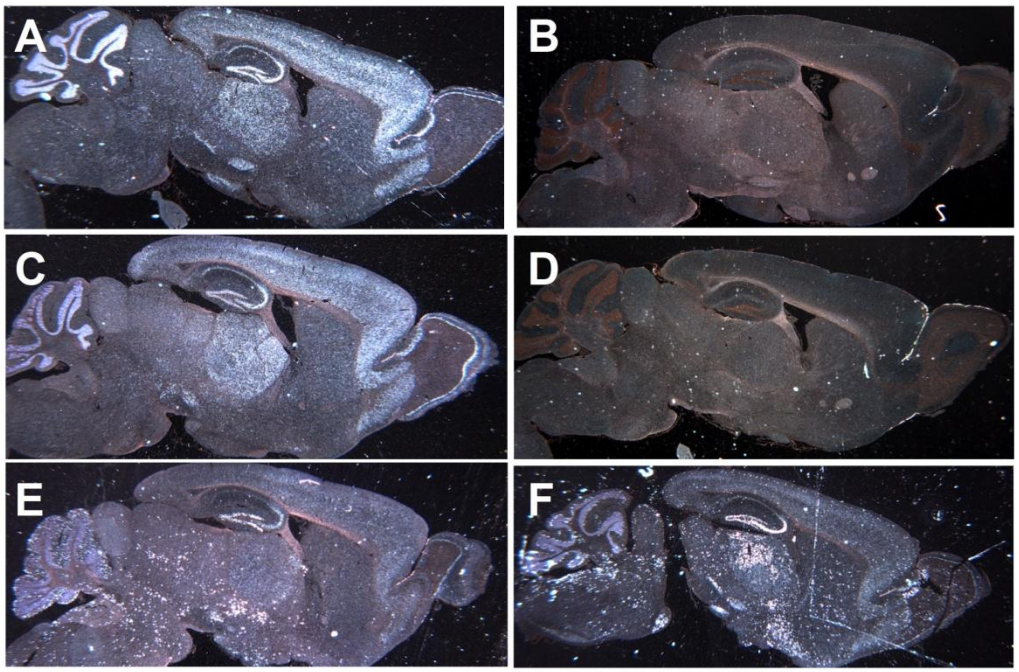

FIGURE 1.4 RIM1 emulsion *in situ* hybridization of conditional RIM1 knockouts using S35-labeled riboprobes. Sagittal sections from WT (A), RIM1α-/- (B), and fRIM/cre- (C) tissue hybridized with the anti-sense probe targeting exon 6 of the RIM1 transcript. The sense probe was hybridized with WT tissue (D). fRIM1/POMC-cre+ (E) and fRIM1/KA-cre+ (F) tissue were hybridized with the antisense probe and display increased signal of transcripts containing exon 6 in selected brain regions.

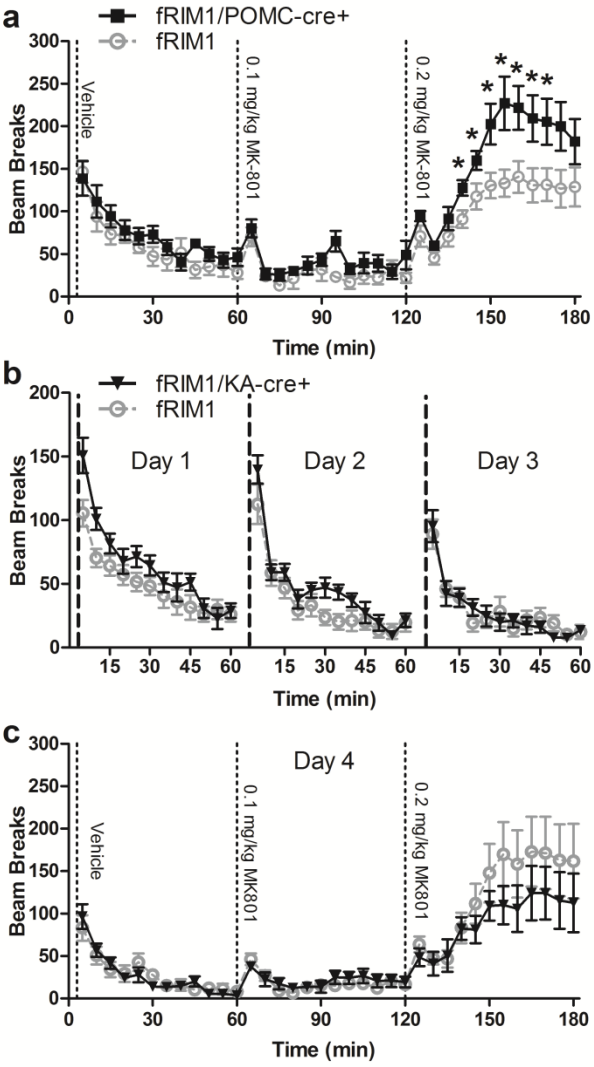

FIGURE 1.5 fRIM1/POMC-cre+ mice exhibit enhanced locomotor response to psychotomimetics. a. 3 hour locomotor test in which fRIM1/POMC-cre+ mice received an injection of saline, 0.1 mg/kg MK-801 or 0.2 mg/kg MK-801 at the beginning of each hour as marked by the vertical dotted lines **b.** Since fRIM1/KA-cre+ mice are hyperactive in novel environments, they were habituated to the 3 hour locomotor test over 3 days, receiving only saline injections at the start of each hour (Only the first hour is shown). **c.** On day 4 fRIM1/KA-cre+ mice underwent the 3 hour locomotor test, receiving saline, 0.1 mg/kg MK-801 or 0.2 mg/kg MK-801 at the start of each hour as marked by the vertical dotted line. (* = $p < 0.05$ using student's t-test)

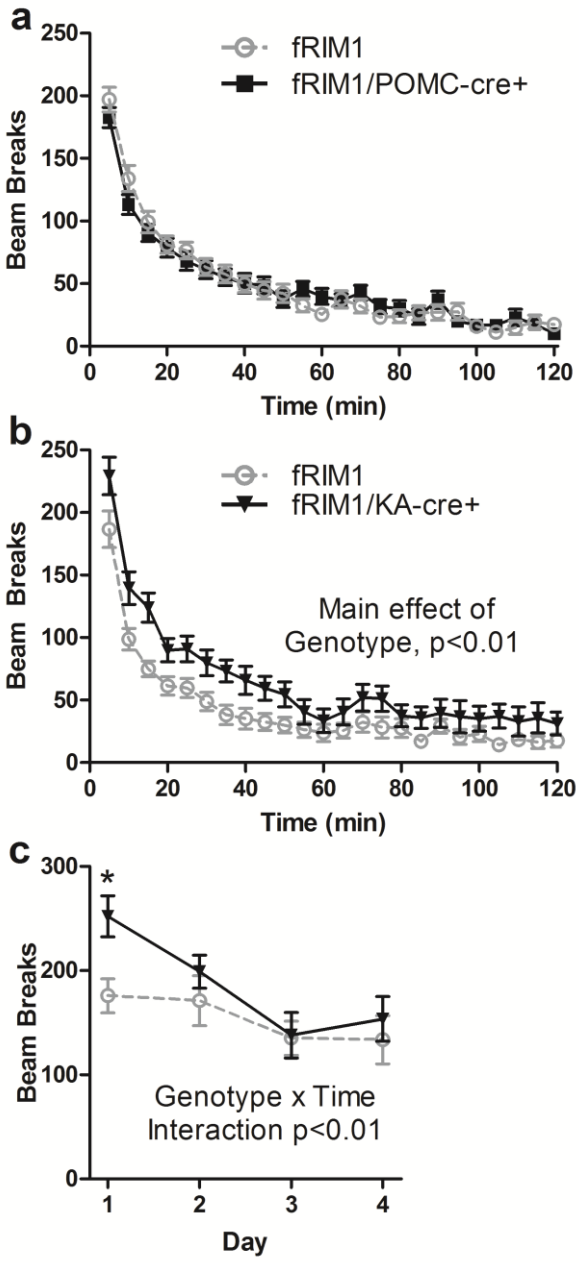

FIGURE 1.6 fRIM1/KA-cre+ mice display enhanced locomotion to novel stimuli. a. fRIM1/POMC-cre+ mice underwent a 2 hour test of locomotion in a novel home cage in which lengthwise movement was monitored using photobeams. **b.** fRIM1/KA-cre+ mice underwent the same test. **c.** Locomotor habituation of the fRIM1/KA-cre+ mice: Over 4 days the first 10 minutes of locomotor activity was recorded (*****, $p < 0.05$ using student's t-test)

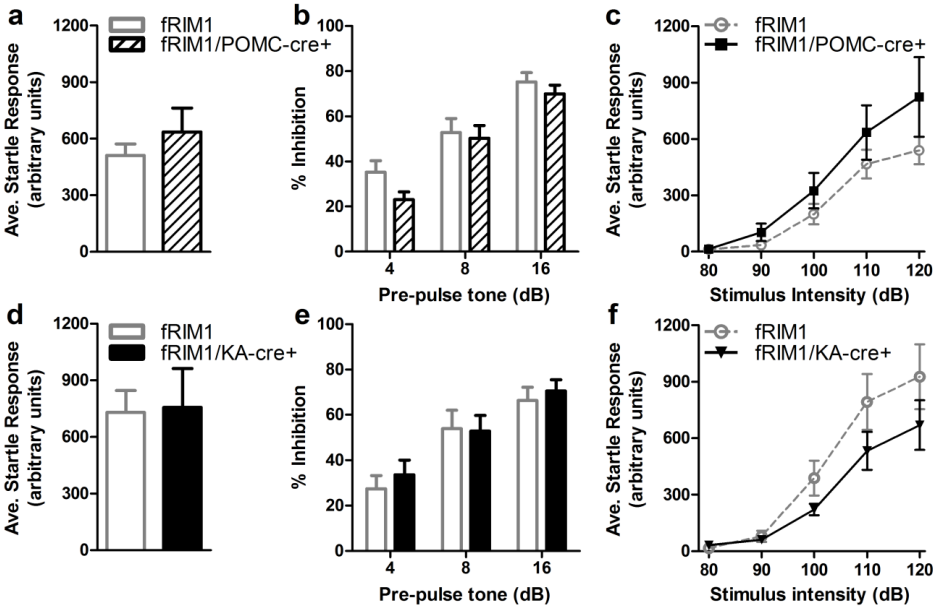

FIGURE 1.7 fRIM1/POMC-cre+ and fRIM1/KA-cre+ mice display normal startle response and pre-pulse inhibition. a and d. The average startle response to a 120 dB tone of fRIM1/POMC-cre+ and fRIM1/KA-cre+ mice respectively prior to the start of the pre-pulse inhibition test. **b and e.** Pre-pulse inhibition test. The percent decrease of the startle response caused by a 4, 8 or 16 dB pre-pulse tone given 100 ms before the 120 dB stimulus tone. **c and f.** Startle threshold. Average startle response to increasing stimulus intensity delivered in a pseudo random order.

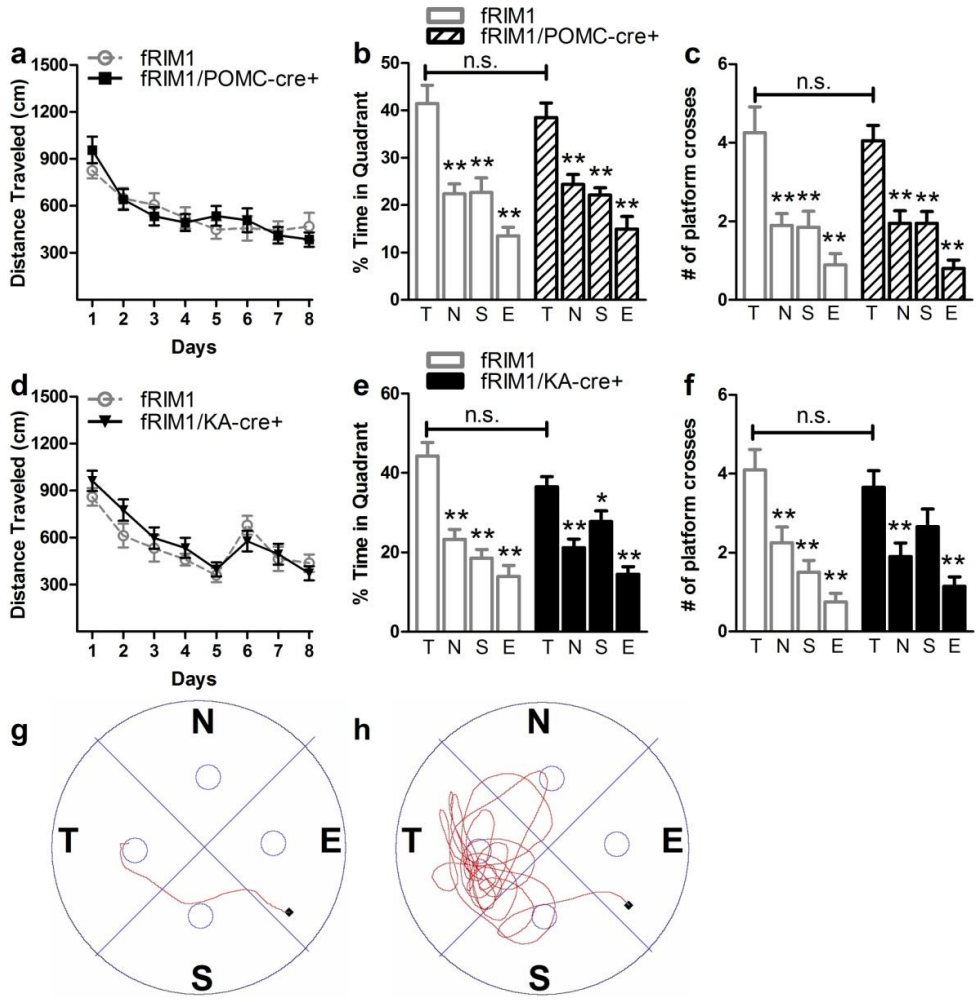

FIGURE 1.8 fRIM1/KA-cre+ and fRIM1/POMC-cre+ display normal spatial learning in the MWM. **a.** During 8 days of training in the Morris water maze, the distance traveled to find the hidden platform was measured in the fRIM1/POMC-cre+ mice. **b and c.** fRIM1/POMC-cre+ probe trial. On day 9 the platform was removed from the pool and the amount of time spent in each quadrant **(b)** and the number of platform location crossings **(c)** were recorded. **d.** 8 day training period in Morris water maze of the fRIM1/KA-cre+ mice. **e and f.** fRIM1/KA-cre+ probe trial. The platform was removed from the pool and the amount of time spent in each quadrant **(e)** and the number of platform location crossings **(f)** were recorded. **g**. Representative tracing of a training trial from day 8. **h**. Representative tracing of a probe trial. (Quadrants and Platform locations: T=Target (West), N=North, S=South, E=East; ***** = $p < 0.05$, ***** = $p < 0.01$, n.s.= not significant)

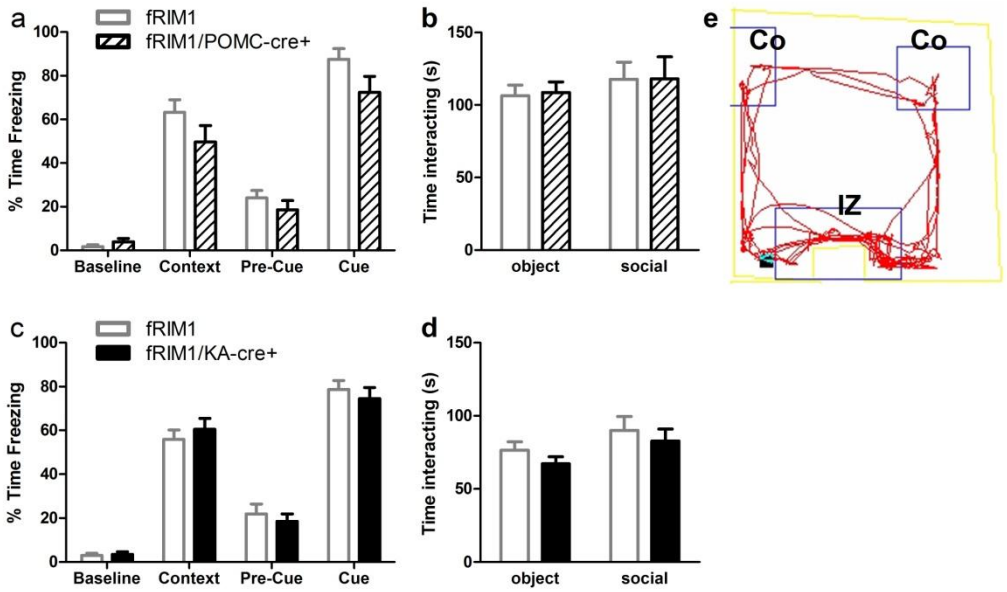

FIGURE 1.9 Contextual and Cued fear conditioning as well as social interaction in the open field are normal in both the fRIM1/POMC-cre+ and fRIM1/KA-cre+ mice. a and c. Fear conditioning in fRIM1/POMC-cre+ and fRIM1/KA-cre+ mice respectively. Baseline freezing was measured during the first two minutes in the novel context prior to tone/footshock delivery. Contextual fear conditioning was measured during a 5 minute exposure to the same context the following day. Cued fear conditioning was also measured the following day. Mice were exposed to a different context without the tone for 3 minutes (pre-tone), followed by 3 minutes with the tone playing (tone). **b and d.** Social interaction in the open field was measured as the amount of time spent in an interaction zone with either an empty cage (object) or a cage containing a target mouse (social). **e.** Representative tracing of a social interaction in the open field trial. (IZ, interaction zone; Co, Corners of the box opposite the interaction zone.)

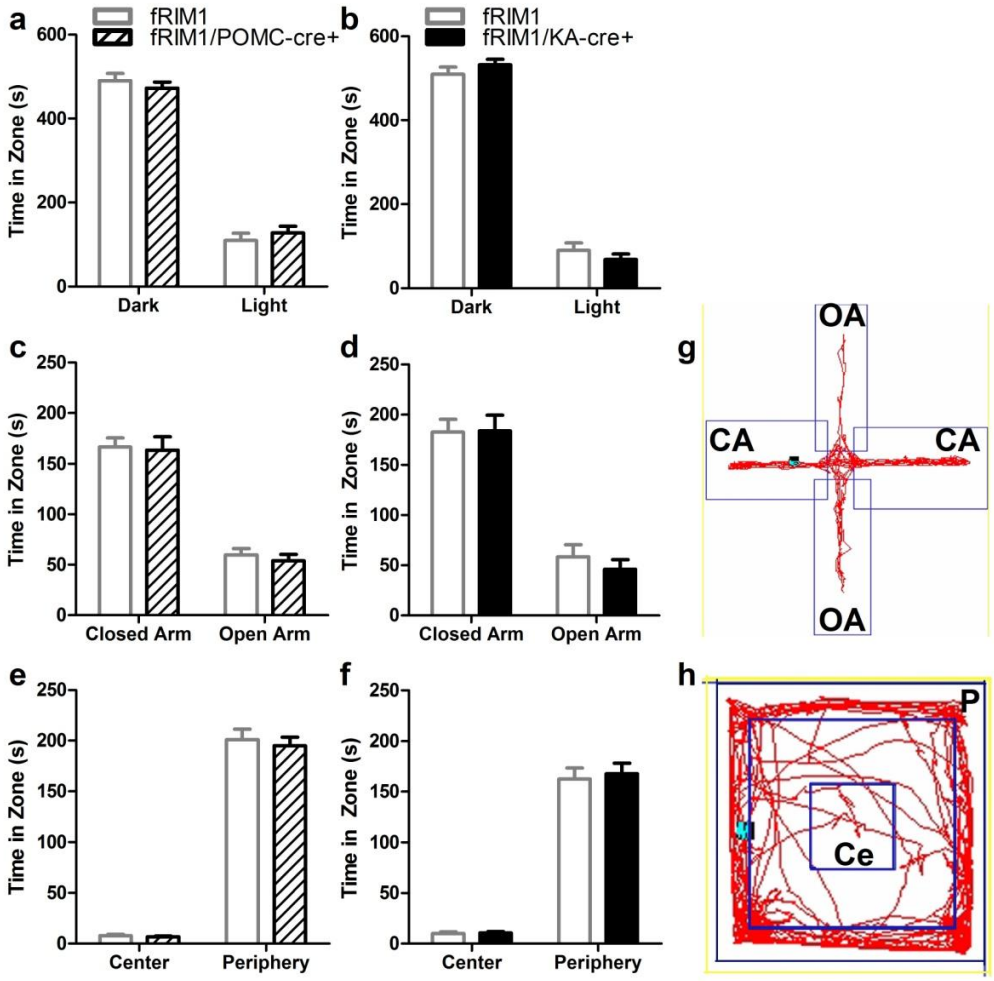

FIGURE 1.10 Three measures of anxiety are normal in both the fRIM1/POMC-cre+ and fRIM1/KA-cre+ mice. a and b. Dark/Light. The amount of time spent in the dark versus light zones is reported. **c and d.** Elevated Plus Maze. The amount of time spent in the open versus closed arms is reported. **e and f.** Open Field. The amount of time spent in the center versus periphery of the open field box is reported. **g**. Representative tracing of an elevated plus maze trial. **h**. Representative tracing of an open field trial. (CA, closed arm; OA, open arm; P, periphery; Ce, Center)

Chapter 1, Section 3

Conclusions and Future Directions

It was have previously demonstrated that global deletion of RIM1α results in multiple behavioral abnormalities including learning deficits in fear conditioning (Powell et al., 2004) and Morris water maze (Powell et al., 2004), decreased pre-pulse inhibition (Blundell et al., 2010b), increased locomotor response to novelty (Powell et al., 2004), deficits in social interaction (Blundell et al., 2010b), increased sensitivity to the non-competitive NMDA receptor antagonist MK-801 (Blundell et al., 2010b) and deficits in maternal behavior (Schoch et al., 2002). The present results serve to narrow the brain regions responsible for the increased sensitivity to the non-competitive NMDAR antagonist MK-801 and the increased locomotor response to novelty. Deficits in maternal behavior and pup rearing were not examined in the present study as they would require specific, complex breeding strategies outside the scope of the present studies.

Characterization of fRIM1/POMC-cre+ and fRIM1/KA-cre+ mice

The fRIM1/POMC-cre+ and fRIM1/KA-cre+ mice lack RIM1 in distinct, partially overlapping brain regions. fRIM1/POMC-cre+ mice exhibit selective cre-mediated recombination in DG granule neurons, arcuate nucleus of the hypothalamus, parvalbumin positive (PV+) GABAergic interneurons of the cerebellar molecular layer

(Yu et al., 1996) and scattered neurons of the cerebellar granule layer. This pattern of cre-mediated recombination in fRIM1/POMC-cre+ mice is supported by the qRT-PCR data demonstrating significantly decreased RIM1 mRNA expression levels in both dentate gyrus and cerebellum, but not in other areas of the hippocampus or the cortex. fRIM1/KA-cre+ mice show robust cre-mediated recombination in area CA3 of the hippocampus and mosaic recombination in hippocampal DG granule neurons, granule and purkinje layers of the cerebellum, thalamus and cortex. Again, the most robust cre-mediated recombination in fRIM1/KA-cre+ mice in CA3 and dentate gyrus was confirmed by qRT-PCR, while the mosaic, cre-mediated recombination in other parts of the brain was not supported by the qRT-PCR data, suggesting that cre-mediated recombination measured by a reporter transgene does not always accurately reflect cre-mediated recombination of a different conditional allele. The RIM1 loss in the cerebellum of fRIM1/POMC-cre+ mice and the widespread mosaic expression of cre-mediated recombination in brains from fRIM1/KA-cre+ mice differ from previous reports characterizing the POMC and KA cre driver lines (Balthasar et al., 2004, McHugh et al., 2007, Nakazawa et al., 2002). Changes in expression patterns of cre recombinase due to changes in genetic background, however, have been observed in other cre driver lines (Smith, 2011). These findings underscore the importance of determining the regions of cre-mediated recombination in each experimental setting.

Additionally and unexpectedly, I found that specifically exon 6 of the RIM1 gene seemed to be upregulated when examined by exon 6 targeted *in situ* hybridization and

qRT-PCR. Attempts at and sequencing the transcript after qRT-PCR demonstrated that it was in fact exon 6 of RIM1. I also attempted to amplify and sequence the exon 6 containing transcript from cDNA libraries derived from the DG of fRIM1/POMC-cre+ by using a sense primer in conjunction with a poly-A primer. This was difficult as multiple fragments were generated, and though I did find an exon 6 containing PCR product, it was not complete and did not provide useful information. Though these attempts failed, it may be possible to repeat this experiment with more carefully collected cDNA libraries that contain more complete transcripts. Understanding exactly what this transcript is would confirm or exclude the likelihood that I have indeed successfully deleted RIM1 transcripts from the targeted neurons. Furthermore, the synthesis of high concentrations of an exon 6 containing gene product, after cre-mediated recombination has presumably removed exon 6 from the genome may suggest a new mechanism of genetic manipulation, or at the very least help in the understanding of potential pitfalls when novel floxed mice are created in the future.

Though the fRIM1/POMC-cre+ mice and fRIM1/KA-cre+ mice show some overlapping cre expression, the two mouse lines do not share any behavioral abnormalities. This provides evidence that at least some of the abnormal behaviors observed in the RIM1α-/- mice are due to a loss of RIM1 function from one or a few select classes of neurons. Identifying how alterations in presynaptic function in select neuronal subtypes alter select behaviors is important for understanding the cellular basis for these behaviors.

Limited neuronal populations sufficient to induce increased MK-801-induced hyperactivity

Like the RIM1α-/- mice, the fRIM1/POMC-cre+ mice exhibit hypersensitivity to the locomotor enhancing effects of MK-801 (Blundell et al., 2010b). Little is known about the specific brain regions or cell types involved in the locomotor effects of MK-801. Because the fRIM1/POMC-cre+ mice mimic the Rim1α-/- mice, however, the results suggest that RIM1 function in the DG, arcuate nucleus or select neurons of the cerebellum (including PV+ interneurons and granule cells) may modulate the effect of MK-801 on locomotor activity. Though some or all of these regions may in fact play a role in this behavioral phenotype, one interesting possibility is a role for PV+ GABAergic interneurons. Studies of PV+ neurons in the cortex suggest that MK-801 acts preferentially on NMDA receptors expressed on PV+ GABAergic cells leading to decreased inhibition (Xi et al., 2009, Kinney et al., 2006, Li et al., 2002, Beasley and Reynolds, 1997, Benes and Berretta, 2001, Hashimoto et al., 2003, Lewis et al., 2005, Cochran et al., 2002). Unfortunately, I was unable to further narrow the brain regions or neuronal types involved in this phenotype due to the technical limitation that there are not selective RIM1 antibodies that work for immunohistochemistry.

While both fRIM1/POMC-cre+ and fRIM1/KA-cre+ mice lead to cre-mediated recombination in the dentate gyrus, only fRIM1/POMC-cre+ mice exhibit increased sensitivity to MK-801. At first glance, this would appear to rule out a role for loss of RIM1 in dentate gyrus in this behavioral abnormality. The percentage of dentate granule neurons in which cre-mediated recombination occurs, however, is clearly much

larger in fRIM1/POMC-cre+ mice than in fRIM1/KA-cre+ mice. Thus, I cannot rule out that an effect of loss of RIM1 in a majority of dentate granule neurons (fRIM1/POMC-cre+) rather than a smaller percentage (fRIM1/KA-cre+) may account for the increased sensitivity to MK-801 in fRIM1/POMC-cre+ mice. It is also possible that loss of RIM1 in combinations of the neuronal subtypes identified in fRIM1/POMC-cre+ is leading to the increased susceptibility to MK-801. Finally, though these mice performed normally in the rotarod task, I cannot rule out the possibility that other cerebellar-related abnormalities may become evident if a more extensive coordination test battery were performed.

Lack of memory deficits in fRIM1/POMC-cre+ and fRIM1/KA-cre+ mice

Unlike RIM1α-/-, the fRIM1/POMC-cre+ and fRIM1/KA-cre+ mice did not show a learning deficit in hippocampus-dependent forms of learning and memory including the Morris water maze and fear conditioning. Since fRIM1/POMC-cre+ lack RIM1 from most DG granule neurons, it suggests that RIM1-mediated forms of plasticity in DG granule neurons are either not required or that only a small percentage of RIM1 expressing DG granule neurons are necessary for these forms of learning. Similarly, since fRIM1/KA-cre+ mice lack RIM1 from almost 100% of CA3 pyramidal neurons, it seems that RIM1-dependent plasticity in area CA3 is not required for these forms learning. It may also be that robust loss of RIM1 from multiple synapses in the hippocampal tri-synaptic pathway is necessary to induce significant learning and memory deficits. As fRIM1/KA-cre+ mice lack RIM1 robustly in area CA3 and mosaically in the DG, it raises the possibility that the learning and memory deficit observed in RIM1α-/- mice may be due,

at least in part, to the loss of RIM1 from extra-hippocampal synapses and may or may not require a loss of RIM1 in the hippocampus.

fRIM1/KA-cre+ mice have a subtle phenotype compared to RIM1α-/- mice

RIM1α-/- mice exhibited increased locomotor activity to novelty (Blundell et al., 2010b). The fRIM1/KA-cre+ mice follow the same pattern except the increased locomotion is lesser in magnitude. Because of a lack of region selectivity and mosaicism of cre expression in fRIM1/KA-cre+ mice, it is difficult to pinpoint brain regions responsible for the increased locomotion to novelty. One interesting point suggested by the results, however, is the double dissociation between increased locomotion to novelty and enhanced MK-801-induced hyperactivity. These two phenotypes do not seem to be mediated by the same set of neurons.

Overview

Overall, both the fRIM1/POMC-cre+ and fRIM1/KA-cre+ mice recapitulate limited components of the phenotypes observed in the RIM1α-/- mice. Both of these cre recombinase driver lines have been used in a variety of studies (Ramadori et al., 2010, Banno et al., 2010, Fukushima et al., 2009, Zhang et al., 2009), some of which specifically compared locomotor activity or swim speed in B6 mice with and without the cre transgene and no abnormalities were observed (Xu et al., 2008, Tonegawa et al., 2003). The phenotypes observed in the fRIM1/KA-cre+ mice are subtle and difficult to attribute to RIM1 loss from particular neurons. The hypersensitivity to the locomotor activation effects of MK-801 was more narrowly limited to a few cell types and brain regions in the fRIM1/POMC-cre+ mice. One way to better study these brain regions in the future may

be to use virally expressed cre recombinase in order to target specific brain regions without the lack of selectivity that often accompanies cre driver lines.

Behavior	RIM1a-/-	fRIM1/POMC-cre+	fRIM1/KA-cre+
Elevated plus maze	Normal	Normal	normal
Open field	not tested	Normal	normal
Dark/Light	Normal	Normal	normal
Locomotion	hyperactivity to novelty	Normal	hyperactivity to novelty
Social interaction with a juvenile	Decreased social interaction	not tested	not tested
Social interaction in the open field	not tested	Normal	normal
Rotarod	Normal	Normal	normal
Startle threshold	not tested	Normal	normal
Pre-pulse inhibition	Decreased pre-pulse inhibition	Normal	normal
Contextual and cued fear conditioning	decreased freezing	Normal	normal
Morris water maze	did not learn to find platform	Normal	normal
Locomotor response to MK-801	enhanced locomotor response	enhanced locomotor response	normal
Maternal Behavior	decreased maternal behavior	not testes	not tested

TABLE 1.1 Summary of behavioral deficits in the RIM1α-/-, fRIM/POMC-cre+ and fRIM1/KA-cre+ mice

CHAPTER 2

PTEN knockdown Regulates Dendritic Spine Morphology but not Density

Chapter 2, Section 1

Introduction and methods

Introduction

According to the National Institute of Mental Health, anxiety disorders are collectively among the most common mental disorder experienced by Americans. The 12-month prevalence among U.S. adults is 18.1%, with lifetime prevalence exceeding 30% for adults between 18 and 55 years old with an average age of onset at 11 years old (Kessler et al., 2005). In the elderly (> 55 years of age) there is wide variation in the prevalence of anxiety disorders reported ranging from 1.2% in New York to 14% in a study conducted in France (Bryant et al., 2008). For adolescents between 13 and 18 years old there is 25.1% lifetime prevalence rate (Merikangas et al., 2010). Overall, females are much more likely than men to experience symptoms of anxiety disorders, and about one fifth of all patients diagnosed with anxiety disorders area considered have severe cases (Merikangas et al., 2010, Kessler et al., 2005).

There is a spectrum of anxiety disorders including generalized anxiety disorder (GAD), panic disorder, specific phobias (which include social anxiety disorder and agoraphobia), obsessive-compulsive disorder, post-traumatic stress disorder (PTSD) and childhood anxiety disorder. Of those patients diagnosed with anxiety disorders, one third are receiving treatment by a health care provider, and only 12.7% are receiving minimally adequate care (Wang et al., 2005). Thus understanding the mechanisms

that underlie anxiety disorders is essential for uncovering novel and more specific therapeutic targets which will be more effective than the current treatment options. Current treatment options for generalized anxiety disorder are broad and vary from person to person but include benzodiazepines, azapirones, antidepressants, anticonvulsants and antipsychotic drugs (Reinhold et al., 2011). In all of these cases, significant side effects exist making compliance a challenge.

These diseases are often co-morbid with other mood disorders including depression and bipolar disorder, and children with untreated anxiety disorders are at a higher risk for developing psychiatric disorders later in life (Ramsawh et al., 2010). Thus, it is not surprising to find that there is overlap between what is known about the neurobiology of these diseases.

The amygdala is a primary site of stress, anxiety and fear response regulation (Davis, 1992, Roozendaal et al., 2009). When one considers the efferent fibers from the central amygdala (the major output from the amygdala), this makes sense. The outputs include 1) Lateral hypothalamus (can cause pupil dilation, tachycardia, blood pressure elevation), 2) Dorsal Motor Nucleus of Vagus and the nucleus ambiguous (which can modulate digestion, urination and induce bradycardia), 3) parabrachial nucleus (cause panting and respiratory distress), 4) ventral tegmental area, locus coeruleus and dorsal lateral tegmental area (can increase vigilance and increase behavioral and EEG arousal), Nucleus reticularis pontis caudalis (can increase startle response), central gray (can cause freezing behavior and inhibit social interaction), trigeminal facial motor nucleus

(can cause facial expression of fear), and the paraventricular nucleus of the hypothalamus (can induce corticosteroid release) (Davis, 1992). Most major inputs to the amygdala go to the basolateral amygdala (BLA) which in turn regulates the central amygdala. One of principal inputs to the BLA comes from the medial prefrontal cortex (mPFC) (Kim et al., 2011). It has been postulated that defects in Inhibition of the BLA from the medial prefrontal cortex, or over-activation of the BLA or both is important in the development of anxiety disorders. In support of this hypothesis imaging studies show that individuals who report increased levels of anxiety have overactive amygdala by functional magnetic resonance imaging (fMRI) at rest and when shown emotionally stimulating images (Goldin et al., 2009, Stein et al., 2002, Yoon et al., 2007, Bishop et al., 2004, Somerville et al., 2004, Holzschneider and Mulert, 2011).

In accordance with this hypothesis, one group has performed a series of manipulations in rats which induce morphological changes that increase the connectivity of excitatory inputs onto BLA pyramidal neurons and cause associated anxiogenesis. Specifically, chronic immobility stress in rats induces enhanced dendritic arborization in BLA pyramidal neurons and decreases the time spent in the open arms of the elevated plus maze task (Vyas et al., 2002). They later go on to show that this enhanced dendritic arborization is accompanied by increased spine density (Mitra et al., 2005). Interestingly, though one day of immobility stress was sufficient to induce dendritic arborization it did not produce an immediate increase in spine density or anxiety. However, one day of chronic immobility stress did produce a 10-day delay in

spinogenesis on BLA pyramidal neurons that paralleled a 10-day delay in the onset of anxiogenesis (Mitra et al., 2005). Finally, they used a transgenic mouse that overexpressed brain derived neurotrophic factor (BDNF) in the forebrain. They found that these mice showed increased anxiety and spine density compared to controls in the absence of any stressful stimuli, and that a further increase in anxiety did not occur with chronic immobility stress, suggesting that BDNF is a mediator of stress induced anxiogenesis and spinogenesis (Govindarajan et al., 2006). As these manipulations were not limited to the amygdala, it is not clear whether the anxiogenic effects of BDNF are tied to the spinogenesis effects of BDNF in the amygdala, though they do provide correlative evidence suggesting a linear relationship between spine density in the amygdala and increased anxiety (Govindarajan et al., 2006).

BDNF and its receptor Tyrosine Kinase Receptor B (TrkB) have been implicated in anxiety disorders by a number of studies as well (Mahan and Ressler, 2012, Radley and Morrison, 2005). Some of these studies examined Val66Met variants of BDNF (Dennis et al., 2010), truncated TrkB isoforms (Carim-Todd et al., 2009), TrkB inhibitors (Cazorla et al., 2010), and BDNF over-expression in the forebrain (Govindarajan et al., 2006) to name a few.

There are a number of major signaling pathways that can be stimulated downstream of BDNF and its receptor TrkB including 1) MEK/ERK, 2) PI3K/AKT and 3) PLCγ/PKC signaling. Though nothing is known about which of these pathways mediates the BDNF induced spinogenesis in the amygdala, some of these molecules and others

have already been implicated in spinogenesis in other brain regions, in particular the hippocampus. One of the downstream pathways of interest is the PTEN/PI3K/AKT pathway.

Phosphatase and tensin homolog deleted on chromosome ten (PTEN) is a lipid and protein phosphatase that negatively regulates the phosphatidylinositol 3-kinase (PI3K)/AKT/mTOR signaling pathway, ultimately modulating cell growth and translation (Leslie and Downes, 2002, Downes et al., 2001, Vazquez and Sellers, 2000, Di Cristofano and Pandolfi, 2000, Dahia, 2000, Maehama and Dixon, 1999, Eng, 1999, Besson et al., 1999, Eng, 2003, Hobert and Eng, 2009, Orloff and Eng, 2008, Waite and Eng, 2002, Maehama and Dixon, 1998, Hoeffer and Klann, 2010). PTEN was originally discovered as the gene responsible for a subset of familial hamartoma syndromes associated with increased risk for certain cancers (Nelen et al., 1997) and as a gene often mutated in human cancers and tumor cell lines (Li et al., 1997, Steck et al., 1997). More recently, mutations in PTEN have been linked directly to autism with macrocephaly and neurodevelopmental delay with macrocephaly, findings that have been replicated by multiple laboratories in multiple cohorts (Boccone et al., 2006, Butler et al., 2005, Buxbaum et al., 2007, Goffin et al., 2001, Herman et al., 2007, McBride et al., 2010, Orrico et al., 2009, Stein et al., 2010, Varga et al., 2009, Zori et al., 1998). Thus, understanding PTEN's role in neuronal morphology and function is important for understanding human neuropsychiatric disease.

PTEN deficiency results in erratic neuronal migration, neuronal hypertrophy, and abnormal arborization and myelination in humans (Abel et al., 2005) and animal models (Backman et al., 2001, Kwon et al., 2001, Fraser et al., 2008, Kwon et al., 2006, Xiong et al., 2012). Using Golgi staining or immunohistochemistry, I and others have demonstrated that PTEN-deficient neurons in brains of animal models have increased synaptic spine density (Kwon et al., 2006, Zhou et al., 2009, Luikart et al., 2011, Fraser et al., 2008) and increased frequency of mEPSCs (Luikart et al., 2011), findings suggestive of a role for PTEN in de novo synapse and synaptic spine formation.

Using sensitive fluorescent dye measures, I have performed a detailed analysis of synaptic spine density and morphology in two different populations of central neurons with shRNA knockdown or transgenic deletion of PTEN. Interestingly, I do not find an increased spine density that would implicate PTEN in de novo spine formation, but rather an overall decrease in total spine density of basolateral amygdala complex (BLA) neurons associated with a decrease in density of thin protrusions at distal dendritic segments and an increase in density of more “mature”, mushroom-shaped spines all along the dendritic tree. In the dentate gyrus granule neurons I found no change in overall spine density, but the same shift in spine morphology: decreased thin protrusions and increased mushroom spines. Spine head diameter of mushroom-shaped spines is also significantly increased. These changes are accompanied by increased frequency and amplitude of mEPSCs onto PTEN-deficient neurons, implying that this structural spine maturation is accompanied by concomitant functional maturation.

These results implicate PTEN and the PI3K/AKT/mTOR pathway in functional and structural spine alterations rather than de novo spine formation. Finally, my data suggest that increased functional, mushroom spine density in the BLA is not sufficient to cause anxiety-like behavioral phenotypes that have previously been correlated with increased BLA spine density and anxiety-like behaviors following chronic stress (Lakshminarasimhan and Chattarji, 2012).

Methods

Recombinant Adeno-Associated Virus

Viruses were constructed and purified by the laboratory of Dr. Michael Kaplitt. Recombinant adeno-associated virus (rAAV) vectors encoding for luciferase-silencing or PTEN-silencing short hairpin loop RNA (shLuciferase and shPTEN respectively) sequences were generated as follows: DNA oligos encoding shLuc and shPTEN were annealed and cloned immediately downstream from the human PolIII H1 promoter into *Bgl*II and *Xba*I sites of an rAAV vector. The following oligos were used: 5'-GATCCCCCCGCTGGAGAGCAACTGCATTTCAAGAGA ATGCAGTTGCTCTCCAGCGGTTTTTGGAA-3' (shLuc) and 5'-GATCCCCGAGTTCTTCCACAAACAGAACTTCCTGTCA TTCTGTTTGTGGAAGAACTCTTTTTTGGAAT-3' (shPTEN). The underlined regions are the target-specific palindrome sequences separated by the loop sequence. The rAAV vector bicistronically expresses YFP under the control of the hybrid CMV enhancer/chicken β-actin promoter. Vector stocks were prepared by packaging the plasmids into AAV serotype 2 particles using a helper-free plasmid transfection system. Serotype 2 has been shown to have specificity for neurons over microglia and astrocytes (Bartlett et al., 1998). The vectors were purified using heparin affinity chromatography and dialyzed against PBS. AAV titers were determined by quantitative PCR using CMV-enhancer-specific primers and adjusted to 10^{11} genomic particles per ml. The integrity and accuracy of all constructs were verified by sequencing.

Intracranial viral injections

7 week old male C57BL/6J mice were anesthetized with 0.1 ml of a 20% ketamine, 10% xylazine in 0.9% saline solution, mounted onto a mouse stereotactic apparatus (KOPF Instruments, Tujunga, CA), and sterilized with ethanol and povidone-iodine (Betadine, Purdue Products). Holes in the skull were drilled 1.2 mm posterior, 3.25 mm lateral from bregma bilaterally and a pulled glass capillary pipette (Sutter Instruments, Novato, CA) containing the virus was brought to the brain surface. The pipette was lowered 4.5 mm where 0.5 µl of AAV-shPTEN or AAV-shLuc was slowly injected into the region of the basolateral amygdala complex (BLA – comprised of the basolateral and lateral nuclei of the amygdala). Following injections, silk sutures were used to close the wound. The location and spread of viral infection was examined post-mortem using immunohistochemistry (IHC – method described below) to detect YFP expression. Only mice that bilaterally expressed YFP in the BLA without significant YFP expression in the cortex, striatum or central amygdala were defined as bilateral BLA hits and used for experimental analysis. This determination took place after the experiments were completed by an investigator blind to the experimental results of each individual mouse. On a subset of mice, I used IHC to co-label 30 µm thick brain sections with anti-NeuN and anti-YFP antibodies, and then took high magnification images within a virally infected region of the BLA. The percentage of infected neurons infected was then calculated as the percent of NeuN+ cells that were also YFP+. For each group, a total of 5 slices were analyzed from 3 mice and averaged together. Immunohistochemical, electrophysiological, and morphological experiments were

performed 3 weeks after surgeries. All experiments were done in accordance with NIH (National Institutes of Health) and University of Texas Southwestern Medical Center animal guidelines and protocols.

Immunohistochemistry

Virus-injected mice were perfused with 4 % paraformaldehyde (Sigma; St. Louis, MO), then whole brains were post-fixed in 4 % paraformaldehyde at 4°C overnight. Brains were then transferred to 30 % sucrose (Sigma) and allowed to equilibrate until they sank. 30 µm sections were cut (HM 430 Sliding microtome, Microm; Waldorf, Germany) at dry ice temperatures and stored at 4°C in PBS containing 0.1 % sodium azide (Sigma) until use. Tissue sections were mounted onto positively charged glass slides (Fisher; Waltham, MA) and allowed to air dry. A 0.1 M citric acid (Sigma) antigen unmasking treatment was performed prior to blocking slices with 3 % normal donkey serum (NDS) (Jackson ImmunoResearch; West Grove, PA) in PBS containing 0.3 % triton X-100 (Sigma). Overnight primary antibody incubation in 3 % NDS, 0.3 % Tween-20 (Sigma) in PBS at room temperature (Chicken anti-GFP 1:2000, Invitrogen, Carlsbad, CA; Mouse anti-NeuN 1:250, Millipore, Billerica, MA; Rabbit anti-PTEN 1:400, and Rabbit anti-pAKT 1:200, Cell Signaling, Danvers, MA) was followed by a 2 h secondary antibody treatment (DyLight 488-conjugated donkey anti-chicken, CY3-conjugated donkey anti-mouse or Biotin-conjugated donkey anti-rabbit; Jackson ImmunoResearch). Tyramide amplification was performed using the Avidin Biotin Complex Kit (Vector Laboratories;

Burlingame, CA) and a Tyramide Signal Amplification Kit (PerkenElmer; Waltham, MA). Images were taken on an Olympus BX51 epifluorescent microscope (Tokyo, Japan).

Neuronal Morphology and Spine Density

Basolateral Amygdala Neurons

Mouse brain tissue was prepared for intracellular loading of neurons in the BLA with Alexa Fluor 568 following methods reported by Dumitriu, et al., with some modifications (Dumitriu et al., 2010, Dumitriu et al., 2011). Mice used for spine analysis were injected with virus and then sacrificed 3 weeks later, 2 mice at a time (1 shLuc and 1 shPTEN), allowing for perfusion, cell filling and confocal imaging to be done within 72 hours. Virus-injected mice were perfused with 5 ml of 1 % PFA in 0.1 M phosphate buffer, pH 7.4 (PB) followed by 60 ml of 4 % PFA and 0.125 % Glutaraldehyde in 0.1 M PB at 5 ml/min. Brains were post-fixed for 2 hours in 4 % PFA and 0.125 % Glutaraldehyde in 0.1 M PB then 225 μm thick slices were cut on a vibratome in chilled 1X PBS (Fisher, Waltham, MA) and stored in 1X PBS at 4°C until use.

Loading of virally infected neurons with Alexa Fluor 568 (Invitrogen) was performed as previously described (Hao et al., 2006) with minor modifications. Sections were immersed in 1X PBS and virally infected neurons of the BLA were identified by epifluorescence, impaled with sharp micropipettes, and loaded with 10 mM Alexa Fluor 568 in 200 mM KCl under a direct current of 1–4 nA for 5–10 min, or until the dye filled distal processes and no additional loading was observed. 5-10 neurons were loaded with dye per mouse and 2-4 neurons were loaded per slice. Sections containing loaded cells

were mounted on glass slides, and covered with H-1000 Vectashield mounting medium (Vector Laboratories). Confocal z-stacks of filled neurons contained 50-80 images 2 µm apart and were captured with a Plan-Achromat 20X/0.75 NA objective lens on a Zeiss, LSM 510. Filled neurons had to meet four criteria to be kept for morphological and spine analysis. (1) The neuron had to be located in the basolateral amygdala complex. (2) The neuron had to express YFP, detected with 3-dimensional imaging taken by confocal fluorescent microscopy (Laser Scanning Microscope 510, Zeiss, Peabody, MA). (3) Due to differences in morphology and spine density between different neuron types in the BLA, the neuron had to be a Class I neuron (McDonald, 1982). Class I neurons were defined as cells with a soma at least 15 µm in diameter, at least 5 primary dendrites and at least 3 quaternary branches derived from different primary branches. (4) The center of the cell body had to be located 20-35 µm beneath the surface of the slice so that a consistent portion of the total dendritic arbor would be included in morphological analysis. 3-dimensional digital reconstructions of neurons were created using Neurolucida and morphological analysis was performed with NeuroExplorer (MBF Bioscience, Williston, VT). After excluding cells that did not meet these criteria, 17 shLuc infected cells from 5 mice and 16 shPTEN infected cells from 5 mice were included in the amygdala study.

Printouts of neuronal reconstructions that included a series of scaled, concentric circles 10 µm apart centered on the cell body were used to pseudo-randomly select dendritic segments for spine analysis. I selected one dendritic segment every 10 µm

from the cell body up to 100 µm. Confocal z-stacks of dendritic segments containing up to 60 images 0.2 µm apart were captured with a 100X/1.4 NA oil immersion objective lens on a Zeiss, LSM 510. Dendritic segments had to meet three criteria to be imaged and included in analysis. (1) The dendritic segment had to span a 10 µm thick circular band created by two adjacent concentric circles. (2) The dendritic segment had to be nearly parallel to the surface of the slice, such that the entire segment could be imaged within a 6 µm thick z-stack. (3) No branching or crossing of nearby labeled dendrites could be observed within the segment. Settings for pinhole size, aperture gain, and offset were optimized initially and then held constant throughout the study to ensure that all images were digitized under the same illumination conditions at a resolution of 0.032 µm × 0.032 µm × 0.2 µm per voxel. One high magnification image was taken every 10 µm from the soma up to 100 µm from the soma. The confocal z-stacks were deconvolved with AutoDeblur (Media Cybernetics, Bethesda, MD) and imported into NeuronStudio (Mt. Sinai School of Medicine, New York, NY) for semi-automated three-dimensional dendrite segment width and length, spine density, spine head diameter and spine classification analysis as reported in Rodriguez et al., 2008 (Rodriguez et al., 2008). Briefly, the spine density was calculated by dividing the total number of spines present by the length of the dendritic segment. Spine subtypes were characterized by Neuron Studio as follows: A spine was deemed stubby if no neck was identified and the total length of the spine was < 2.5 times the width of the base of the spine. A spine was classified as a thin protrusion in two ways: 1) No neck was identified but its total length

was > 2.5 times the width of the identified base of the spine. 2) A neck was identified but the head diameter was < 0.37 µm. A mushroom spine was classified as a spine with a neck and a head diameter > 0.37 µm. Details regarding the algorithms used to calculate head diameter and neck length have been published elsewhere (Rodriguez et al., 2008). Of note, head diameter is taken as the largest diameter of the head in three-dimensional space. The head diameter threshold of 0.37 µm was obtained by manually classifying spines in a subset of shLuc neurons and plotting the head diameter distribution of thin and mushrooms spines. The intersection of those distributions was used as the head diameter threshold. No distinction was made between filapodia and thin spines and thus both are included in the thin protrusion category. A Student's t-test was used for statistical analysis except when distance was included as a repeated measure factor in which case a 2-way ANOVA with repeated measures was used.

Dentate Gyrus Granule Neurons

PTEN cKO mice and WT littermate pairs were provided by Dr. Luis Parada. Mice were sacrificed for spine analysis at 6 months of age. Tissue was prepared in the same manner as above, with the exception that prior to cell-filling, slices were stained with DAPI so that the dentate gyrus cell body layer could be identified. Cells were filled in the same manner as stated above, except that dentate gyrus cell body layer neurons were chosen at random. Whole cell morphological analysis was not performed, but dendritic segments of filled cells were selected for confocal imaging based on three criteria. (1) The dendritic segment had to span the 20-50 µm distance from the edge of the cell body

layer. (2) The dendritic segment had to be nearly parallel to the surface of the slice, such that the entire segment could be imaged within a 6 µm thick z-stack. (3) No branching or crossing of nearby dendrites could be observed within the segment. Dendrite width, spine density and spine head diameter were all analyzed as stated above except that manual classification of spines from a subset of the WT DG granule neurons provided a head diameter threshold of 0.5 µm.

Electrophysiology

Spontaneous, Miniature Synaptic Transmission in Amygdala

Coronal slices (300 um thick) including the BLA were prepared and recordings performed as described previously (Stuber et al., 2011). Briefly, 3-5 weeks after stereotaxic injections of the viral vectors (see above), mice were anesthetized with pentobarbital, perfused intracardially with 20-30 ml of modified 0°C artificial cerebrospinal fluid (aCSF) and decapitated. The brain was quickly isolated and chilled into dissecting solution. The dissecting solution contained the following (in mM): 75 sucrose, 81 NaCl, 2.5 KCl, 1.0 NaH2PO4, 0.1 CaCl2, 4.9 MgCl2, 26.2 NaHCO3, and 1.5 glucose (300-305 mOsm). The bathing solution contained the following (in mM): 119 NaCl, 2.5 KCl, 1.25 NaH2PO4, 2.5 CaCl2, 1 MgCl2, 26.2 NaHCO3, and 10 dextrose, saturated with 95% O2/5% CO2. For recording of mEPSCs, the bathing solution was supplemented with Tetrodotoxin (0.5 □M) and Picrotoxin (100 □M). Slices were incubated in the bathing solution at 32°C for at least 1 h. Afterward, slices remained at 32°C or room temperature until transferred to a submersion-type recording chamber.

Whole-cell patch-clamp recordings from BLA neurons were performed using micropipettes (3-5 M□) made from 1.1/1.5 mm borosilicate glass (Sutter or King Precision Glass). Recording pipettes were filled with the following solution (in mM): 117 Cs-methanesulphonate, 2.8 NaCl, 5 TEA-Cl, 0.4 EGTA, 2 ATP-Mg, 0.25 GTP-Mg, 20 HEPES-CsOH (pH 7.2-7.4, 275-285 mOsm). Access resistance was frequently checked to be < 25 M□ and stable (less than 20% of variability). Recordings were obtained using the 700B Multiclamp amplifier (Molecular Devices), and neurons were visualized using a fluorescent microscope equipped with infrared differential interference contrast. All responses were digitized at 10 kHz and filtered at 1 kHz. Data were analyzed offline using pClamp, Minianalysis (Synaptosoft) and Microsoft Excel. Student's t-test was used to evaluate significance of all analyses.

Behavior

Behaviors were done on two cohorts of mice with less stressful tests at the beginning and more stressful tests toward the end in the following order: elevated plus maze, dark/light, open field, locomotor, social interaction with a juvenile, social interaction in an open field, startle threshold, contextual and cued fear conditioning, and footshock threshold (McIlwain et al., 2001). The behavioral tests were begun at 3 weeks post virus injection. Mice were given a 24 hr inter-test interval throughout the test battery (Paylor et al., 2006). Mice were allowed 1 h to habituate to the testing room prior to beginning experiments. Significance was taken as $p < 0.05$ for all behaviors. Only mice with clear, bilateral BLA viral targeting were included in the study. (N=15 AAV-

PTEN-shRNA injected mice and N=12 AAV-Luciferase-shRNA injected mice). All behavioral tests were done in accordance with IACUC and UT Southwestern Medical Center animal guidelines and protocols.

Tests of Anxiety – tests of anxiety were performed as previously reported (Tabuchi et al., 2007). For the **elevated plus maze** task mice were placed in the center of a black plexiglass elevated plus maze (each arm 33 cm in length and 5 cm wide, with 25 cm high walls on closed arms) in a dimly lit room for 5 min. 2 mazes were used and video-tracked simultaneously (Ethovision 2.3.19, Noldus; Wageningen, The Netherlands). A barrier was set between the mazes to prevent mice from seeing each other. Time spent in open and closed arms, number of open and closed entries, and time in the middle was calculated. Data were analyzed with a 1-way ANOVA. The **open field** test was performed for 10 min in a brightly lit, 48 x 48 x 48 cm white plastic arena using the Ethovision video-tracking software (Noldus). Time spent in the center zone (15 x 15 cm) and frequency to enter the center was recorded. Locomotor activity was also measured during the open field test. Data were analyzed with a 1-way ANOVA. The **dark/light** apparatus is a 2 compartment opaque plexiglass box. One side is black and kept closed and dark, while the other is white with a fluorescent light directly above its open top. Mice were placed in the dark side for 2 min, and then the divider between the two sides was removed allowing the mouse to freely explore both chambers for 10 min. Time spent in the light and in the dark compartments were measured. Measures were taken

using photobeams and MedPC software (Med Associates; St. Albans, VT). Data were analyzed with a 1-way ANOVA.

Locomotor – The locomotor test was performed as previously reported (Tabuchi et al., 2007). Mice were placed in a fresh home cage with minimal bedding for a 2 hour testing period. Lengthwise horizontal activity was monitored using photobeams linked to computer data acquisition software (San Diego Instruments, San Diego, CA). Data were analyzed with a 2-way ANOVA with repeated measures (2-way rmANOVA).

Social Interaction Tests – Tests of social interaction were performed as previously reported (Tabuchi et al., 2007). Direct **social interaction with a juvenile** took place in a novel, empty, clear, plastic mouse cage under red light as previously reported. Following a 15 min habituation in the dark, the experimental and target mice were placed in the neutral cage for two min and allowed to directly interact. Time spent interacting with the juvenile was scored by an observer blind to genotype. Social learning was assessed three days later by allowing mice to interact with the same juvenile for an additional two min. Again, time spent interacting with the juvenile was scored. Data were analyzed with a 3-way mixed ANOVA with genotype and sex as between subjects factors and test session as a within subjects factor. **Social interaction in the open field** was tested by placing experimental mice in a 48 × 48 cm^2 white plastic arena using a 6.0 × 9.5 cm porous rectangular plexiglass cage with or without an adult mouse as a target, allowing olfactory and minimal tactile interaction. Social interaction was measured as the time

spent in the interaction zone (area immediately surrounding the target cage). 1-way ANOVA was used to compare time spent in the interaction zones between groups.

Fear Conditioning – Fear conditioning was performed as described previously (Powell et al., 2004). Mice were placed in clear plexiglass shock boxes (Med Associates) for 2 min, and then two, 90 dB acoustic conditioned stimuli (CS; white noise, each 30 seconds in duration and separated by a 30 second delay) were played. Each CS co-terminated in a 2 s, 0.5 mA foot shock (US). Mice remained in the chamber for 2 min after the second pairing before returning to their home cages. Freezing behavior (motionless except respirations) was monitored at 5 s intervals by an observer blind to the genotype. To test contextual learning 24 hr later, mice were returned to the same training context and scored for freezing in the same manner. To assess cue-dependent fear conditioning, mice were placed in a novel environment with an unfamiliar vanilla odor in the afternoon following the contextual test. Freezing was measured first during a 3 min baseline period then during 3 minutes with the CS playing. Cue-dependent fear conditioning was measured by subtracting the 3 min baseline period from the 3 min CS period. Data were analyzed with a 1-way ANOVA.

Startle Threshold – This task was performed exactly as described previously (Blundell et al., 2010b). Briefly, mice were presented with 6 trial types of varying intensity (No Stimulus or 80, 90, 100, 110, or 120 dB pulses – eight presentations of each). Mean startle amplitudes for each condition were averaged. Data were analyzed with a 2-way rmANOVA.

Footshock Threshold – Footshock threshold analysis was performed as described previously (Blundell et al., 2009). Briefly, mice were placed in fear conditioning apparatus for a two min habituation followed by a two s footshock with an interstimulus interval of 20 s of gradually increasing intensity from 0.05 mA at 0.05 mA steps. The intensity required to elicit flinching, jumping and vocalizing was recorded by an observer blind to genotype. Data were analyzed with a 1-way ANOVA.

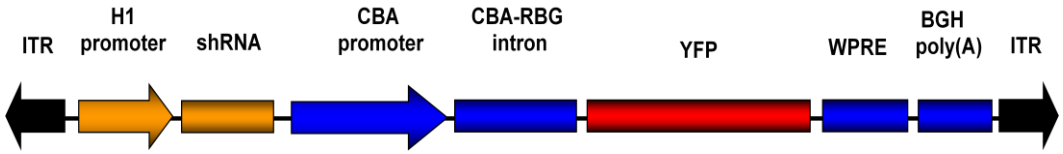

FIGURE 2.1 Map of AAV vectors. Map of AAV vectors. Major elements include: AAV-2 inverted terminal repeats (ITR), human H1 promoter, shRNA palindrome, hybrid CMV enhancer/chicken β-actin (CBA) promoter, enhanced yellow fluorescent protein (YFP), WPRE and bovine growth hormone (BGH) polyadenylation signal.

Chapter 2, Section 2

Experimental Findings

Chattarji and colleagues (Govindarajan et al., 2006, Lakshminarasimhan and Chattarji, 2012) had previously demonstrated that following chronic and acute immobilization stress, BDNF (an upstream regulator of the PI3K/AKT/mTOR pathway) and spine density concomitantly increase in the BLA (Lakshminarasimhan and Chattarji, 2012). In BDNF overexpressing transgenic mice, increased BDNF and increased neuronal spine density in BLA correlated with increased anxiety (Govindarajan et al., 2006). I initially hypothesized that increased activity of the PI3K/AKT/mTOR pathway via knockdown of PTEN would be sufficient to increase spine density and increase anxiety-like behavior. To test these hypotheses, I injected shRNA-expressing AAV serotype 2 into the BLA that would target and knockdown PTEN transcripts preferentially in neurons (Bartlett et al., 1998). I then measured neuronal and spine morphology and size, miniature EPSPs and a battery of anxiety, locomotor, social interaction and fear learning tasks.

Characterization of viral injections

In order to knockdown PTEN, I used AAV-PTEN-shRNA (shPTEN) injections into the BLA compared to control virus AAV-luciferase-shRNA (shLuc). Because both the shPTEN and shLuc viruses bicistronically expressed YFP, I used immunohistochemistry (IHC) against YFP to examine the accuracy of the bilateral viral injections into the BLA 3

weeks after injection (Figure 2.2 A-B). I found that more than half of the injected mice showed YFP expression largely contained bilaterally to the BLA bilaterally (data not shown). Mice that did not exhibit YFP expression in the BLA, or that exhibited significant YFP expression in the central amygdala, cortex, or striatum were excluded from the studies in a manner completely blind to behavioral and morphological results. In order to examine the anterior-posterior spread of the virus within the BLA, I again used anti-YFP antibodies to label brain sections taken every 180 μm along the anterior-posterior axis of the amygdala (Figure 2.2 C). I found that YFP expression spread more than 1 mm along the anterior-posterior axis. Finally, I quantified the percentage of neurons expressing YFP within an infected region by co-labeling sections with anti-YFP and anti-NeuN antibodies and then calculated the percentage of NeuN+ cells that were also YFP+ (Figure 2.2 D-G). The percentage of neurons infected by the shPTEN and shLuc viruses was not significantly different (shPTEN, Mean – 58.80%, SEM - ±1.58%; shLuc, Mean - 54.81%, SEM - ±1.58%; $p = 0.23$, N=5). While around half of the NeuN+ cells were also YFP+, it is important to note, that few of the YFP+ cells were NeuN- (Figure 2.2 G). Though small numbers of other cell types may have been infected, this supports what is already known about the neuron selective tropism of AAV serotype 2 viruses (Bartlett et al., 1998).

I next tested whether the shPTEN virus effectively resulted in decreased PTEN protein levels by double-labeling YFP and PTEN in brain sections from shPTEN and shLuc injected mice. In low magnification images, shPTEN infected tissue (Figure 2.3 A-C)

revealed that PTEN protein levels were significantly decreased in regions expressing viral YFP, while shLuc infected tissue (Figure 2.3 D-F) showed no change in PTEN levels in regions expressing viral YFP. When these sections were imaged with higher magnification, cells located within or bordering the shPTEN infected region that express detectable levels of PTEN do not express YFP (Figure 2.3 G-I). However, in the shLuc infected cells, no detectable change in PTEN levels was observed among cells inside or outside the infected region (Figure 2.3 J-L). Thus, shPTEN effectively reduces PTEN levels while the control virus, shLuc, does not.

To determine if PTEN function also decreased after shPTEN viral infection, I assessed the expression of phosphorylated AKT (pAKT) which is downstream of PTEN and PI3K. Under normal conditions PTEN function acts to decrease the amount of phosphatidylinositol trisphosphate, thereby decreasing PI3K activity and decreasing pAKT in the cell. Thus, with decreased PTEN function I expected increased pAKT within the shPTEN infected region. When I co-localized the virally expressed YFP and pAKT, low magnification images revealed that shPTEN infection dramatically increases pAKT levels (Figure 2.3 M-O) while shLuc infected tissue does not display any increase in pAKT levels (Figure 2.3 P-R). Under higher magnification I observed that cells infected with the shPTEN virus have increased pAKT levels (Figure 2.3 S-U) while shLuc infected cells do not (Figure 2.3 V-X).

PTEN knockdown in BLA neurons induces neuronal hypertrophy

In order to measure changes in the morphology of virally infected neurons, YFP+ BLA neurons were loaded with the red fluorescent dye, Alexa Fluor 568. Z-stack images of loaded cells (Figure 2.4 A-B) were used to digitally reconstruct infected cells and analyze soma size, dendritic length and dendritic branching. Somas of shPTEN infected neurons were found to be significantly larger than in shLuc infected neurons (Figure 2.4 C; shPTEN - Mean, 4143.0 μm^3, SEM, ± 345.9 μm^3; shLuc - Mean, 2636.1 μm^3, SEM, 176.3 μm^3; N=18, $p < 0.001$ using student's t-test). When I performed a Scholl analysis using concentric circles whose radii increase in increments of 30 µm, I found no change in total dendritic length (data not shown) or in the length of dendrite at any specific distance from the cell body between shPTEN and shLuc infected neurons (Figure 2.4 D). I also did not detect any change in the total number of branch points (data not shown) or number of branch points (nodes) at any specific distance from the cell body between the two groups (Figure 2.4 E). I did observe, however, a dramatic increase in dendrite diameter of shPTEN infected neurons that seemed to be most prominent from 30-80 µm from the cell body (Figure 2.4 F; 2-way ANOVA, main effect of virus, $F_{(1,310)} = 35.02$, $p < 0.0001$, main effect of distance $F_{(9,310)} = 13.58$, $p < 0.0001$, virus X distance interaction $F_{(9,310)} = 0.81$, $p = 0.61$). This difference in dendrite diameter between shLuc and shPTEN infected neurons is also beautifully illustrated in figure 2.5 A-D. The increase in dendritic caliber and soma size are consistent with what is known about the knockdown and knockout of PTEN in the DG (Zhou et al., 2009, Luikart et al., 2011, Kwon et al., 2006, Kwon et al., 2003).

PTEN knockdown causes a decrease in thin protrusion density at distal dendritic segments and a corresponding increase in mushroom spine size and density all along the dendritic tree

Because cell body and dendrite diameters were increased in the shPTEN neurons, I questioned whether spine head diameter would also increased. Thus, I analyzed spine heads and identified a significant increase in spine head diameter in PTEN knockdown neurons compared to shLuc-infected control neurons. Spine head diameter was measured using confocal microscopy to take high magnification, high resolution, z-stack images of dendritic segments every 10 µm up to 100 µm from the cell body (Figure 2.5 A-D shows representative images). Overall, average spine head diameter was increased in shPTEN neurons compared to shLuc neurons at all dendritic distances measured (Figure 2.5 E; 2-way ANOVA with repeated measures (rmANOVA), main effect of virus $F(1,26) = 25.14$, $p < 0.0001$; main effect of distance $F_{(9,234)} = 2.58$, $p < 0.01$; virus X distance interaction $F_{(9,234)} = 10.54$, $p < 0.0001$).

In addition to determining the overall spine head diameter, which could be affected simply by increasing the proportion of mushroom-shaped spines compared to thin protrusions, I sub-categorized spines into mushroom and stubby spines and thin protrusions. After sub-categorizing spines in this manner, I observed that mushroom spine head diameter as a separate group was increased in the shPTEN neurons (Figure 2.5 F; main effect of virus $F_{(1,17)} = 9.14$, $p < 0.01$; main effect of distance $F_{(9,153)} = 2.19$; $p < 0.05$; virus X distance interaction $F_{(9,153)} = 1.35$, $p = 0.21$). Stubby spine and thin

protrusion head diameters, however, were no different between shLuc and shPTEN neurons (Figure 2.5 G and 2.5 H respectively). Thus, it appears that the overall increase in spine head diameter of shPTEN neurons in the BLA can be attributed to the increase in mushroom spine head diameter in addition to possible changes in the proportion of mushroom spines.

Because knocking down PTEN has been reported by my lab and others to increase spine density (Luikart et al., 2011, Zhou et al., 2009, Kwon et al., 2006), I also measured spine density in shPTEN and shLuc neurons. Contrary to my lab's and others' previous findings using less sensitive measures, I did not find an increase in total spine density; on the contrary, statistical analysis revealed an interaction between virus and distance that suggested a decrease in total spine density in shPTEN neurons at the more distal segments compared to shLuc neurons with no change in density more proximally. (Figure 2.6 A; 2-way rmANOVA, main effect of virus $F_{(1,31)} = 2.13$, $p = 0.15$; main effect of distance $F_{(9,279)} = 32.72$, $p < 0.0001$; virus X distance interaction $F_{(9,279)} = 2.02$, $p < 0.05$).

To tease apart the contribution of different spine types on spine density, I evaluated the density of mushroom spines, stubby spines and thin protrusions independently. This analysis demonstrated that mushroom spine density was increased in shPTEN neurons compared to shLuc neurons while both thin protrusion and stubby spine densities were decreased in shPTEN neurons compared to shLuc neurons (Figure 2.6 B-D; mushroom, main effect of virus $F_{(1,31)} = 10.96$, $p < 0.01$; main effect of distance $F_{(9,279)} = 19.7$, $p < 0.0001$; virus X distance interaction $F_{(9,279)} = 1.02$, $p = 0.42$; thin, main

effect of virus $F_{(1,31)}$ = 5.12, $p < 0.05$; main effect of distance $F_{(9,279)}$ = 25.63, $p < 0.0001$; virus X distance interaction $F_{(9,279)}$ = 2.07, $p < 0.05$; stubby, main effect of virus $F_{(1,31)}$ = 14.99, $p < 0.001$; main effect of distance $F_{(9,279)}$ = 2.97, $p < 0.01$; virus X distance interaction $F_{(9,279)}$ = 0.61, $p = 0.79$). These differential changes in spine subtypes result in shPTEN neurons with a dramatically increased mushroom spine fraction along the entire length of the dendrite compared to shLuc neurons (Figure 2.6 E; main effect of virus $F_{(1,26)}$ = 34.44, $p < 0.0001$, main effect of distance $F_{(9,234)}$ = 2.65, $p < 0.01$; virus X distance interaction $F_{(9,234)}$ = 9.90, $p < 0.0001$). When the mushroom spine fraction was calculated for the entire 100 µm length of dendrite, 39.2% (SEM ± 3.02%) of spines in shPTEN neurons were mushroom spines, while only 22.95% (SEM ± 2.64%) of spines were mushroom spines in shLuc neurons (Figure 2.6 F; student's t-test, $p < 0.001$).

PTEN knockdown-induced shift from thin protrusions to mushroom spines is not specific to amygdala neurons

My findings in basolateral amygdala neurons of decreased spine density at distal segments and a shift from thin protrusions to mushroom spines directly contrasted with previous reports from the Powell Lab of increased spine density in dentate gyrus granule neurons of PTEN conditional knockout mice. These findings could be explained by regional and neuronal differences or by an increased sensitivity of Alexa Fluor 568 cell filling followed by confocal spine-imaging compared to previously used methods. In an effort to distinguish between these interpretations, I used the same fluorescent cell filling, imaging, and spine analysis techniques on dentate gyrus granule neurons in PTEN

conditional knockout mice (PTEN cKO) as I used in the BLA. Similar to previous work in these PTEN cKO mice, images were taken of dentate gyrus granule neuron dendrites spanning the 20-50 µm distance from the dentate gyrus cell body layer (representative images in Figure 2.7 A-B) As expected, and similar to my findings in the BLA and previous reports (Luikart et al., 2011, Zhou et al., 2009), I found that PTEN cKO neurons had increased dendritic diameter (Figure 2.7 C; WT, 0.80 ± 0.04 µm; PTEN cKO, 1.85 ± 0.13 µm, student's t-test $p < 0.0001$). I also found that, similar to the BLA shPTEN neurons, spine head diameter was increased; however, in the DG a significant increase was observed across all three spine types (Figure 2.7 D; All spines, WT 0.38 ± 0.01, PTEN cKO 0.63 ± 0.02, student's t-test $p < 0.0001$; mushroom spines, WT 0.77 ± 0.02, PTEN cKO 0.95 ± 0.02, $p < 0.0001$; thin protrusions, WT 0.32 ± 0.006, PTEN cKO 0.37 ± 0.006 $p < 0.05$; stubby spines, WT 0.40 ± 0.04, PTEN cKO 0.70 ± 0.04 $p < 0.0001$).

As spine density was previously reported to be increased in dentate gyrus granule neurons of PTEN cKO mice (Kwon et al., 2006), I expected similar results. However, I found that similar to the shPTEN neurons in BLA, there was an increase in mushroom spine density with a corresponding decrease in thin protrusion density with a small increase in stubby spine density that resulted in no change in overall spine density (Figure 2.7 E; all spines, WT 3.93 ± 0.27 spines/µm, PTEN cKO 3.87 ± 0.33 spines/µm, $p = 0.89$; mushroom spines, WT 0.48 ± 0.04 spines/µm, PTEN cKO 1.67 ± 0.17 spines/µm, $p < 0.0001$; thin protrusions, WT 3.36 ± 0.27 spines/µm, PTEN cKO 2.02 ± 0.19 spines/µm, $p < 0.001$; stubby, WT 0.09 ± 0.02 spines/µm, PTEN cKO 0.18 ± 0.02 spines/µm, $p < 0.01$).

Finally, again similar to shPTEN neurons in BLA, the mushroom spine fraction (# mushroom spines/# total spines) in the PTEN cKO dentate granule neurons was significantly and dramatically increased compared to WT neurons (Figure 2.7 F; WT 33.4 ± 2.54%, PTEN cKO 66.46 ± 2.52%, $p < 0.0001$). Thus, PTEN deficiency-induced increases in mushroom spine density and corresponding decreases in thin protrusion density are common to both amygdala neurons and dentate granule neurons, even using different knockdown approaches and different durations of knockdowns. These results suggest a widespread role for the PTEN/PI3K/AKT/mTOR pathway in maintaining the proper balance of thin protrusions and mushroom spines in neurons throughout the central nervous system.

shPTEN infected neurons display increased miniature EPSC neurotransmission

Dendritic spines are a major site for excitatory synaptic neurotransmission (Bourne and Harris 2007). Spines of diverse sizes and morphologies are thought to represent different stages of spine maturity and to vary in function (Bourne and Harris, 2007, Matsuo et al., 2008). As demonstrated above, shPTEN infected neurons had increased mushroom spine density, decreased thin protrusion density at distal segments, and increased spine head diameter. The differences in these dendritic spine parameters suggest that synaptic transmission may also be altered due to knockdown of PTEN. As an initial step in investigating this possibility, I recorded miniature excitatory post-synaptic currents (mEPSC) from the BLA in coronal brain slices 3-5 weeks after vector injection. shPTEN or shLuc infected neurons expressing YFP+ were detected by

epifluorescence. I found that shPTEN infected neurons showed a significant increase in mEPSC frequency (Figure 2.8 A and B; WT 1.18 ± 0.40 Hz, PTEN cKO 3.66 ± 1.01 Hz, $p < 0.030$). The amplitude of mEPSC was also increased (Figure 2.8 C and D; WT 17.39 ± 1.03 Hz, PTEN cKO 23.22 ± 2.6Hz, $p < 0.046$). Similar functional results have been published for dentate granule neurons with decreased PTEN (Luikart et al., 2011), supporting a conclusion of altered synaptic function due to PTEN knockdown.

Lack of associated behavioral abnormalities following PTEN knockdown in a subset of BLA neurons

Given previously published findings correlating increased functional spine density in the BLA with increased anxiety (Govindarajan et al., 2006), I sought to determine if the increase in mushroom spine density and corresponding increase in mEPSC frequency in the BLA alone would also correlate with increased anxiety. In spite of significant alterations in the number of functional, mature synaptic spines, I observed no alterations in anxiety-related tasks including elevated plus maze, open field and dark/light box (Figure 2.9 A-C). Similarly, no alterations in other behavioral tasks were observed including social interaction with a juvenile, fear conditioning, startle threshold, social interaction in an open field, and locomotor activity (Figure 2.9 D-H).

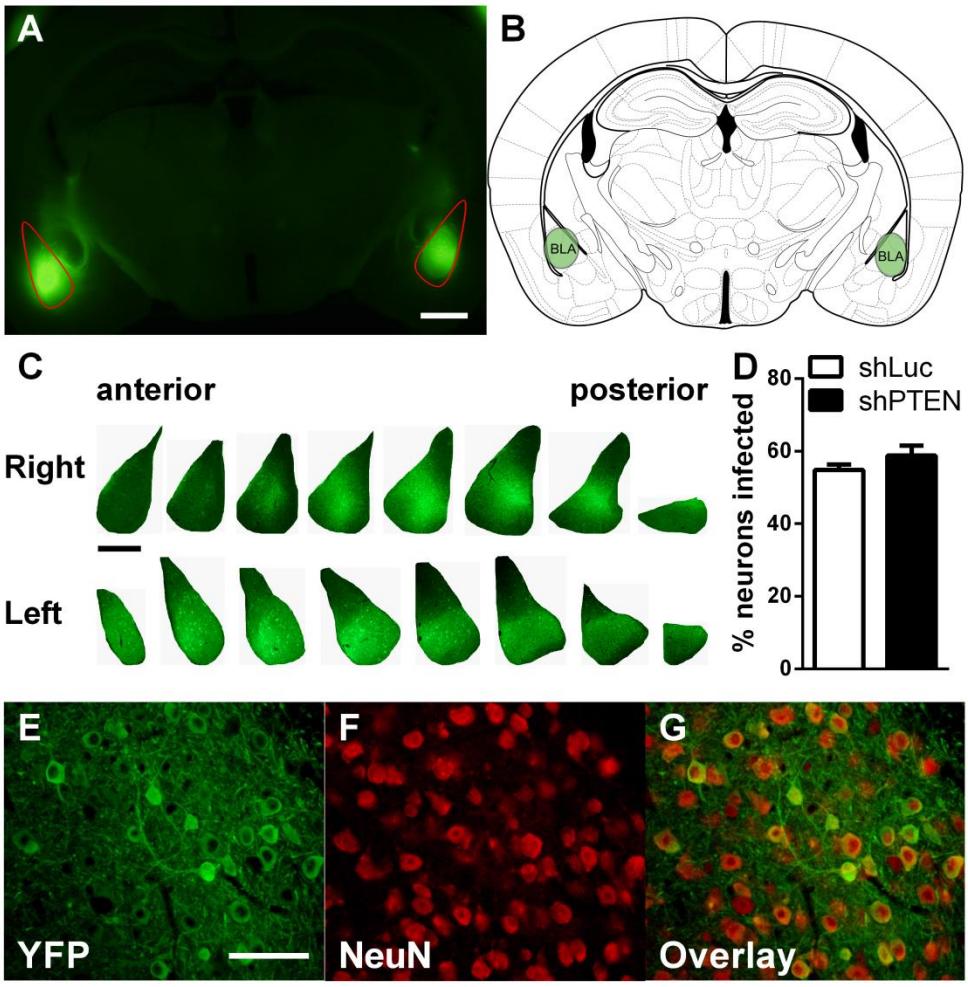

FIGURE 2.2 shPTEN and shLuc virus injections target the basolateral amygdala complex. A. Example image of bilateral infection of the BLA (outlined in red). **B.** A schematic of a coronal mouse brain section at -1.70 mm relative to bregma (adapted from Paxinos and Franklin (2001) with infection sight highlighted in green). **C.** Sections of virally infected BLA (sections separated by 180 µm) showing anterior-posterior spread of virus. **E-G.** Representative images of immunofluorescent staining of YFP (green) and NeuN (red). Images were taken within a virally infected region of the BLA and the number of NeuN+ and YFP+ cells were counted. **D.** Quantification of cell counts reported as the percentage of NeuN+ cells that were also YFP+. No difference between groups was observed using a student's t-test. N = 5 for both shPTEN and shLuc infected slices. (ant = anterior; pos = posterior; scale bar in **A** = 1mm; scale bar in **C** = 500 µm and applies to all images in panel C; scale bar in **E** = 60 µm and is applicable to **E-G**.)

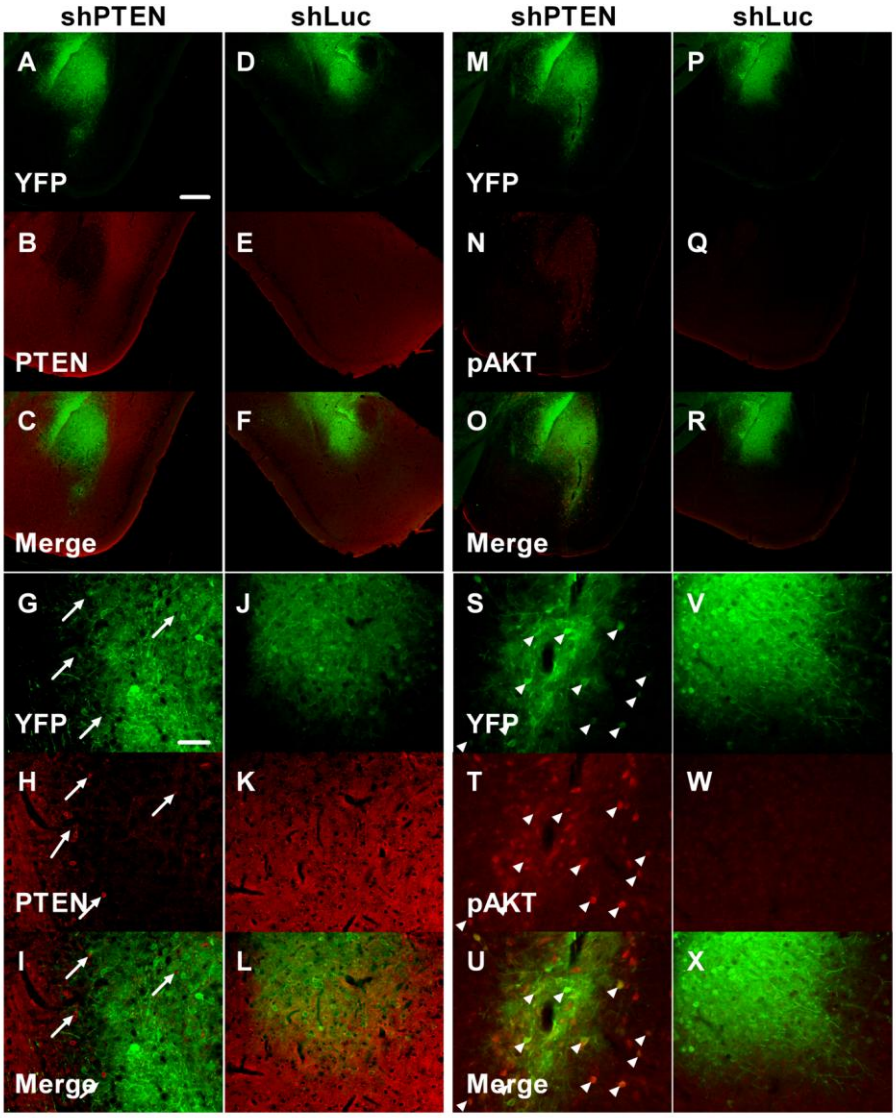

FIGURE 2.3 shPTEN infected cells experience a robust decrease in PTEN expression and a resultant increase in phosphorylated AKT. A-L are double immunofluorescent staining of YFP (green) PTEN (red). shPTEN infected cells show dramatic decrease in PTEN expression levels **(A-C low power and G-I high power)** while shLuc infected cells do not decrease PTEN expression **(D-F low power and J-L high power)**. Arrows point to cells within or at the borders of the infected region that still express PTEN and are not YFP positive **M-X** are double immunofluorescent staining of YFP (green) and phosphorylated AKT (pAKT, red). shPTEN infected cells display upregulated levels of pAKT **(M-O low power and S-U high power)** while shLuc infected cells do not express significant levels of pAKT **(P-R low power and V-X high power)**. Arrowheads point to individual cells that are double positive for YFP and pAKT. (Scale bar in **A** = 500 µm and is applicable to images **A-F and M-R**; scale bar in **G** = 100µm and applies to images **G-L and S-X**.)

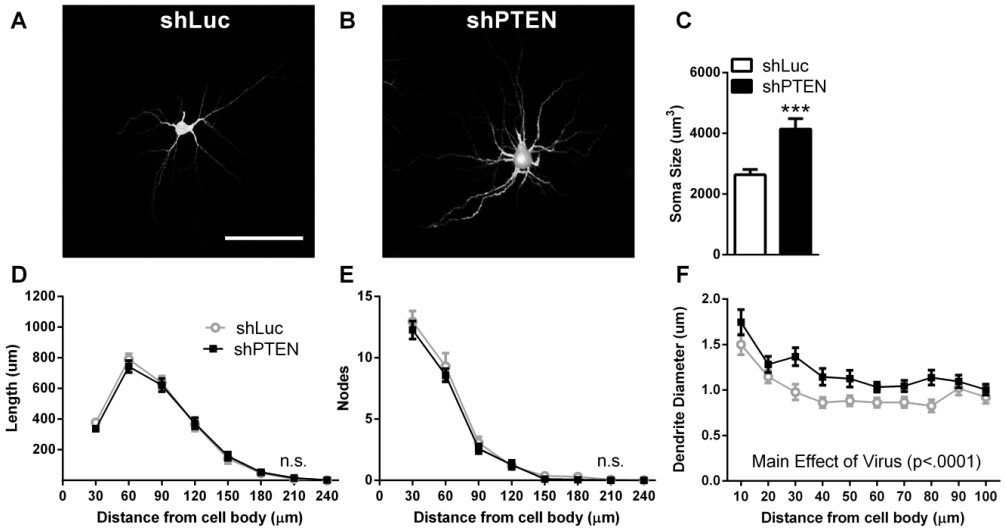

FIGURE 2.4 Soma size and dendrite width are increased in shPTEN infected cells compared to shLuc infected cells in the BLA. A and B. Representative images of shLuc **(A)** and shPTEN **(B)** infected neurons filled with the red Fluor 568 fluorescent dye. **C**. Quantification of 3-dimensional soma size (µm3) was analyzed after 3-D reconstruction of neurons using Neurolucida. **D and E**. A Scholl analysis was performed on 3-D reconstructions of Alexa Fluor 568 filled neurons using concentric circles whose radii increase incrementally by 30 µm. There was no difference in length of dendrites **(D)** or intersections of dendrites with concentric circles **(E)**. **F**. Dendrite diameter was measured in 10 µm increments. One dendritic segment was pseudo-randomly chosen and measured for each neuron at each distance. (N=17 shLuc infected neurons and N=16 shPTEN infected neurons; Scale bar in **A** = 100 µm and is applicable to **A and B**; *** - p<0.001; n.s. – not significant)

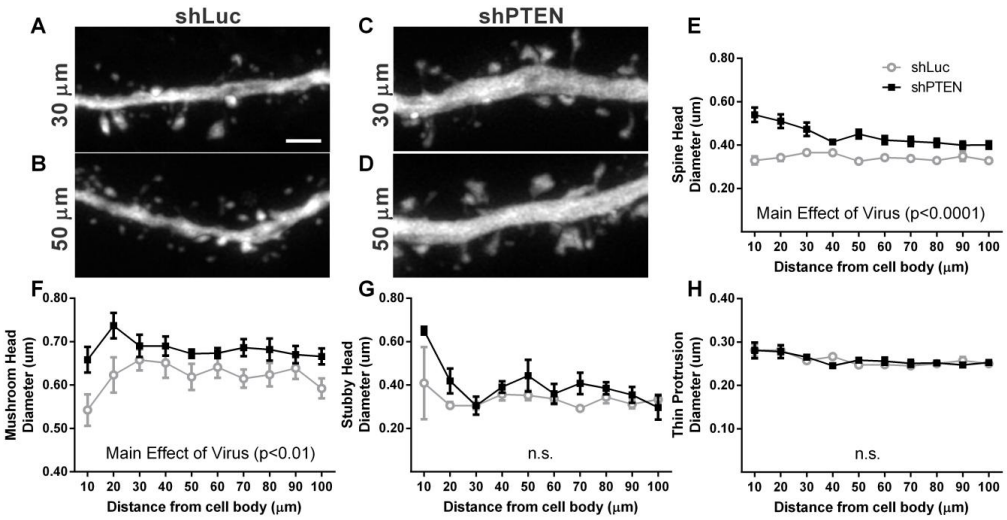

FIGURE 2.5 Mushroom spine head diameter is significantly increased in the shPTEN infected neurons. A-D. Representative images of Alexa Fluor 568 filled dendritic segments from shLuc infected (**A and B**) and shPTEN infected (**C and D**) neurons at 30 µm and 50 µm away from the cell body. **E.** Average spine head diameter is increased in shPTEN infected neurons compared to shLuc infected neurons. A detailed analysis of spine subtypes reveals that this increased spine head diameter is due to an increase in mushroom spine head diameter **(D)** while stubby spines **(E)** and thin protrusions **(F)** show no increase in spine head diameter. (N=17 shLuc infected neurons and N=16 shPTEN infected neurons. Scale bar in **A** = 2.5 µm and is applicable to **A-D**. n.s. – not significant)

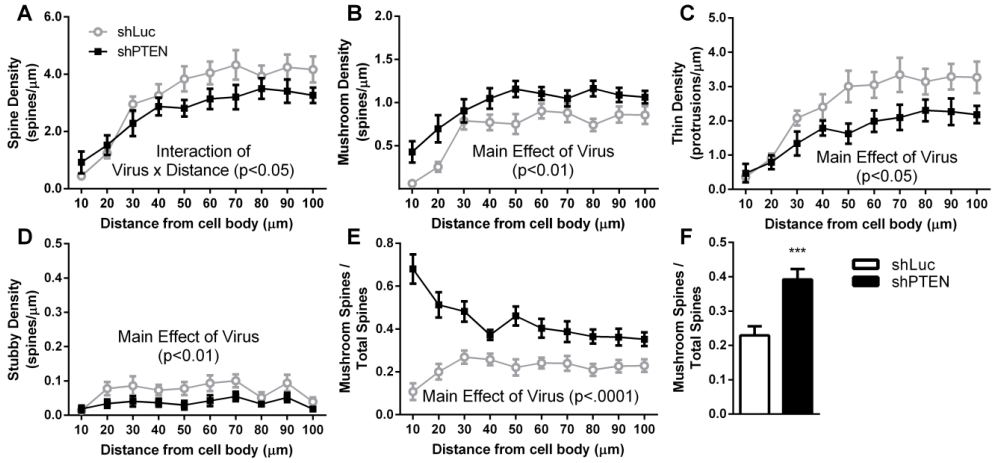

FIGURE 2.6 Fraction of mushroom spines is increased in shPTEN infected cells. A. Spine density is decreased in more distal dendrite segments. **B-D.** An analysis of spine subtypes reveals that although thin protrusions **(C)** and stubby spines **(D)** account for the decrease in total spine density, mushroom spine density **(B)** is significantly increased. **E.** There is a significant shift toward an increased fraction of mushroom spine density, particularly in the more proximal dendrite segments. **F.** The total mushroom spine density fraction including all distances from the cell body is increased in the shPTEN infected neurons compared to controls. (N=17 shLuc infected neurons and N=16 shPTEN infected neurons; ***, p<0.001)

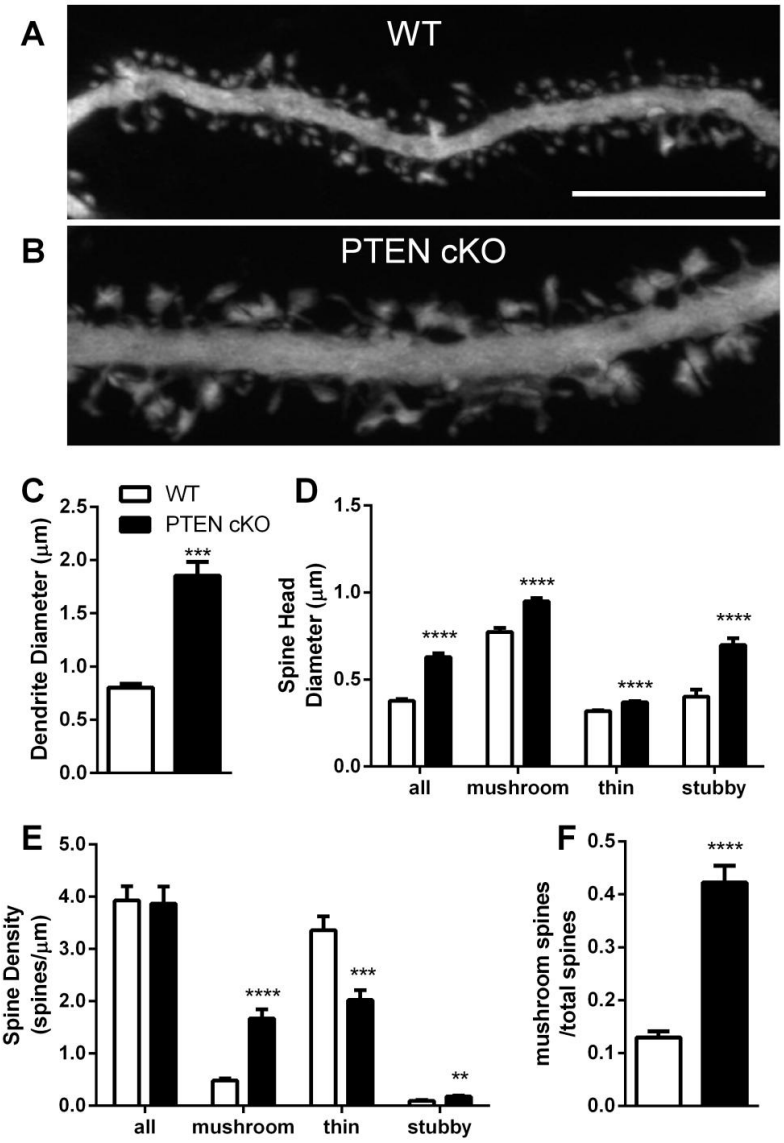

FIGURE 2.7 Conditional PTEN KO mice selective for the dentate gyrus granule neurons have increased mushroom spine head diameter and an increase in the mushroom spine fraction with no change in total spine density. A and B. Representative images of Lucifer Yellow filled WT **(A)** and PTEN-cKO **(B)** dentate gyrus granule neuron dendritic segments taken 20-50 µm from the dentate gyrus cell body layer. **C.** Diameter of the dendritic segments used for spine analysis. **D.** Average spine head diameter of all spine types, mushroom spines, thin protrusions and stubby spines. **E.** Spine density of all spines, mushroom spines, thin protrusions and stubby spines. **F.** Quantification of the mushroom spine fraction. (N=17 for both WT and PTEN-cKO neurons; **, $p < 0.01$; ***, $p < 0.001$; ****, $p < 0.0001$; Scale bar in **A** = 10 µm and is applicable to **A** and **B**)

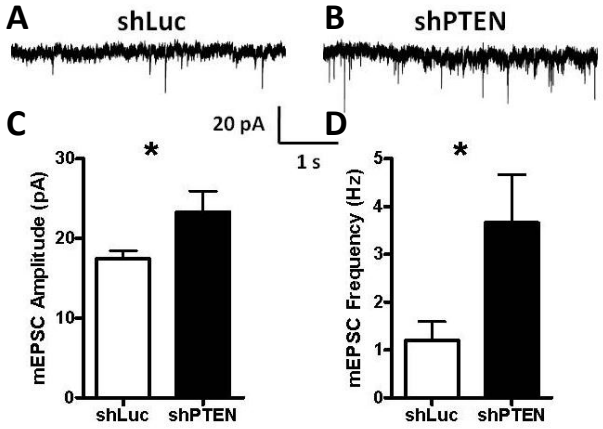

FIGURE 2.8 shPTEN infected neurons show increased miniature EPSC amplitude and frequency. Top. A and B. Representative traces from shLuc and shPTEN mEPSC recordings. **C.** Increased amplitude of mEPSCs in shPTEN compared to shLuc infected BLA neurons. **D.** Increased mEPSC frequency in shPTEN compared to shLuc infected BLA neurons. (*, P<0.05, N=11 shLuc and N=10 shPTEN)

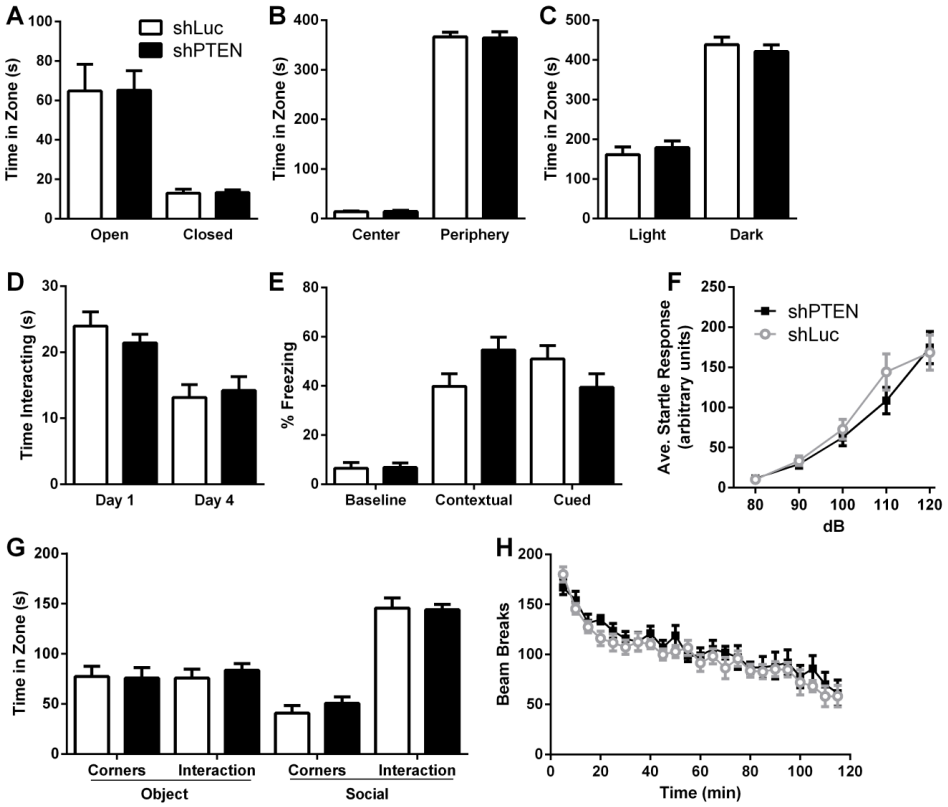

FIGURE 2.9 shPTEN injected mice do not show behavioral phenotypes three weeks post-injection. No difference was observed between shPTEN and shLuc injected mice in three tests of anxiety: elevated plus maze **(A)**, open field **(B)** and dark/light box **(C)**. Additionally, no differences were observed in social interaction with a juvenile **(D)**, both contextual and cued fear conditioning **(E)**, startle threshold **(F)**, social interaction in the open field **(G)** and locomotion **(H)**. (N=12 shLuc mice and N=15 shPTEN mice)

Chapter 2, Section 3

Conclusions and Future Directions

Previous work by my lab and others reported that loss of PTEN from DG granule neurons causes neuronal hypertrophy and increased spine density (Kwon et al., 2001, Kwon et al., 2006, Luikart et al., 2011). Loss of PTEN induces upregulation of pAKT and its downstream targets including mTOR. Inhibiting mTOR reversed the neuronal and synaptic effects of PTEN deletion in DG granule neurons (Kwon et al., 2003, Zhou et al., 2009). Additionally, PTEN knockdown increases mEPSC frequency and amplitude in dentate gyrus granule neurons (Luikart et al., 2011). In accordance with these reports, I found neuronal hypertrophy in BLA neurons after virally-mediated PTEN knockdown, measured as increased soma size and dendritic caliber (Figure 2.4 C and F). Thus, many of my findings support and extend previous work on PTEN in the brain. Moreover, I extended previous findings to include increased diameter of mushroom spine heads (Figure 2.5 F-G).

In contrast to previous reports, however, my data suggest that PTEN knockdown in neurons does not increase total spine density, but instead induces a shift in the mushroom:thin ratio such that the density of mushroom spines are increased while thin protrusion density is decreased in distal dendritic segments (Figure 2.6). In my analysis of spine morphology, I made no distinction between thin spines and filapodia leaving room to question whether one or both of those categories of protrusions were

decreasing after PTEN knockdown. Nevertheless, my findings were strengthened after I obtained similar results in a second brain region using cre recombination for PTEN knockdown and imaging spines in older mice: 6 months of age.

Interestingly, I still observed an increase in spontaneous synaptic activity in shPTEN infected BLA neurons in spite of a decrease in total spine density at more distal segments (Figure 2.8). The increased mEPSC frequency is most parsimoniously explained by increased density of mushroom spines, thought to represent more mature/active synapses (Bourne and Harris, 2007), relative to thin protrusion density. My data suggest that upregulation of the PI3K/AKT/mTOR pathway does not increase spine density, but instead increases the fraction of functional synapses in the BLA.

Since most studies examining the effects of PTEN knockdown on spine density were done in dentate gyrus (Kwon et al., 2001, Kwon et al., 2006, Luikart et al., 2011), one explanation for my novel findings could be that DG and BLA respond differently to PTEN knockdown. Alternatively, my results could be explained by a difference in spine imaging technique. Previous studies used Golgi staining and light microscopy (Govindarajan et al., 2006, Kwon et al., 2006) or confocal imaging of virally expressed GFP (Luikart et al., 2011). Light microscopy is low resolution, and GFP expression may not be concentrated enough in small spines, or there may be significant background signal due to many cells expressing GFP. In addition, imaging spines after Golgi staining using light microscopy prevents the observation of spines in front of or behind the dendrite, decreasing the observed total spine density. With a smaller total density it

would be more difficult to identify subtle changes in spine density across groups. Cell filling, however, allows for good intensity of fluorescent dye in spines and throughout the dendrites while producing little to no background from surrounding cells allowing for improved resolution. These differences in imaging technique and resolution would allow better detection of thin protrusions. Using methods with a decreased detection of thin protrusions, it would appear as though PTEN knockdown induced an increase in total spine density, while in reality no change or even a decrease had occurred.

To examine these alternative explanations, I measured spine density in DG granule neurons in PTEN cKO mice using the cell-fill approach. PTEN knockdown in DG decreased thin protrusion density and increased mushroom spine density without changing total spine density (Figure 2.7 E-F). The similar results in the DG and BLA using two different approaches for knocking down PTEN supports the hypothesis that cell filling techniques allow for better visualization of small spines and more accurate measurement of PTEN's effects on spine density/function. Overall, these data imply that loss of PTEN has similar effects on spine density and morphology in the DG and BLA neurons, and that in order to observe this shift from mushroom spines to thin protrusions, one must be able to image the smaller thin protrusions which may be missed with other techniques.

Similar to studies in the hippocampus (Luikart et al., 2011), I demonstrated that knockdown of PTEN in BLA causes an increase in the frequency and amplitude of mEPSCs. As pointed out above, although I saw no indication suggesting an increase in

the total number of synapses after PTEN knockdown, there was an important increase in the relative number and size of mushroom spines all along the dendritic arborization. Mushroom spines are thought to be more active than thin protrusions (Fiala et al., 2002). Interestingly, spine head volume correlate with the size of the presynaptic readily releasable pool and with the number of docked-vesicles (Dobrunz and Stevens, 1997, Harris and Stevens, 1989), which could affect the frequency of mEPSCs. Furthermore, the size of dendritic spines is also correlated with the area of the postsynaptic density and the number of glutamatergic receptors at the synapse (Harris and Stevens, 1989, Nusser et al., 1998, Arellano et al., 2007). This is consistent with the increase in mEPSC amplitude shown here after knockdown of PTEN, or with a similar outcome due to an increase in surface expression of AMPA receptors after leptin-induced PTEN inhibition (Moult et al., 2010). Thus, the increase in frequency and amplitude in mEPSC observed after knockdown of PTEN in BLA are likely caused by an increase in the number, diameter, and the associated functional properties of the “more mature” mushroom-type of synapse.

In addition to the neuronal and synaptic effects of BDNF overexpression, Govindarajan, et al. (2006) also demonstrated that BDNF overexpression in the mouse forebrain, including the BLA, causes anxiogenesis. Because the amygdala is part of the circuitry known to regulate fear and anxiety, I hypothesized that decreased PTEN in the BLA, which causes similar neuronal and synaptic changes as BDNF overexpression, would lead to increased anxiety-like phenotypes. However, in the elevated plus maze,

dark/light, and open field tasks I found no changes in behavior. Thus, the findings of neuronal hypertrophy, shifting of spine subtypes, and increased mEPSC frequency and amplitude in the BLA after knockdown of PTEN do not correlate with induction of anxiety-like behavioral abnormalities in these tasks. One possibility is that I did not infect a sufficient number of neurons in the BLA to induce a behavioral phenotype. On the other hand, the observed neuronal and synaptic changes in the BLA alone may not be sufficient to induce behavioral phenotypes. Thus, it remains unresolved whether PTEN knockdown in the BLA can lead to changes in anxiety-related behavior similar to those observed following chronic stress and in the BDNF overexpressing mice.

PTEN mutations have been implicated in human autism (Boccone et al., 2006, Butler et al., 2005, Buxbaum et al., 2007, Goffin et al., 2001, Herman et al., 2007, McBride et al., 2010, Orrico et al., 2009, Stein et al., 2010, Varga et al., 2009, Zori et al., 1998), and PTEN conditional knockout limited to the cortex and hippocampus results in alterations in social interaction, an effect that can be reversed by mTOR inhibition (Kwon et al., 2006, Zhou et al., 2009). In the present study, I assessed whether PTEN knockdown isolated to the BLA could result in social behavior abnormalities. Interestingly, I found no alterations in locomotor activity, social interaction with a juvenile, social interaction in an open field, startle threshold, fear conditioning, or footshock threshold in mice treated with shPTEN in the bilateral BLA. These findings support the conclusion that the social and anxiety phenotypes observed in the PTEN

conditional KO mice (Kwon et al., 2006, Zhou et al., 2009) are subserved largely by loss of PTEN in hippocampus or cortex.

In summary, my findings support a novel role for PTEN in modulation of spine morphology. My data suggest that the mechanism leading to increased synaptic activity after PTEN knockdown is not increased total spine density. Instead, my data implicate the PTEN/PI3K/AKT/mTOR pathway as an inducer of synaptic maturation by shifting the mushroom:thin ratio in favor of mushroom spines without dramatically altering total spine density. It seems most likely that loss of PTEN results in conversion of thin protrusions into mature, functional mushroom spines. I cannot rule out, however, that this shift is occurring via de novo mushroom spine formation with concurrent pruning of the thin protrusion population. Given the disease processes for which the PTEN/AKT/mTOR pathway has been implicated, including autism (Butler et al., 2005, Buxbaum et al., 2007) and some forms of cancer (Li et al., 1997, Steck et al., 1997), understanding the role of this pathway in neuronal and synaptic growth and maturation is vital to understanding the pathophysiology of these disorders.

Chapter 3

Two Approaches to Selective Knockdown

The Two Approaches

In the previous two chapters I discussed my findings regarding the alteration of two very different mechanisms affecting synaptic function within selected regions of the mouse brain. In Chapter 1 synapses were altered principally in CA3, DG and cerebellum by eliminating RIM1, a protein that is fundamental to the neurotransmitter release machinery. In Chapter 2, synaptic function was altered in the BLA by knocking down PTEN, a key regulator of the PI3K/AKT signaling pathway, which led to significant structural changes in synaptic spines and affected spontaneous neurotransmission. In both cases there is a change in synaptic function that presumably alters the manner in which the affected neurons communicate with and adapt to their circuits and ultimately how the circuit performs its function. And though some behavioral phenotypes were observed in the fRIM1/cre+ mouse lines, so little is known regarding how changes in synaptic function in specific brain regions lead to observed behavioral phenotypes. Many labs are working on this very broad and complex question.

The previous two chapters are also contrasted by the experimental techniques used to decrease expression of a particular protein at selected regions in the mouse brain. In the case of RIM1, transgenic mice were engineered to eliminate RIM1 from target proteins during development. In the PTEN study, I used shRNA expressing AAV to infect neurons and knockdown PTEN in adult mice. There are advantages and disadvantages to both of these techniques that are worth exploring and understanding so that future studies might be more efficiently executed.

Cre-Lox Transgenic Mice

With the advent of Cre-Lox recombination technology, huge leaps were taken in many fields. It is an extremely adaptable system that functions in many animal models and can be made more sophisticated (and more complicated) if necessary to target specific cell populations in space and time. Furthermore, cells within a given population will utilize similar promoter sequences with great reliability, such that extremely high percentages of cells within a population will express cre under a specific promoter, while neighboring or even overlapping cell populations will not. This allows for dissection of the nervous system by function or at least by gene expression without respecting spatial and temporal boundaries; something other scientific methods struggle to do. Additionally, cre-lox systems in combination with conditionally expressed fluorescent proteins allow researchers to visualize and study targeted cells before and after genetic manipulation in new, creative and extremely convenient ways.

In this system, scientific advancement is accelerated because one lab can generate a conditional (floxed) allele for a gene of interest and then eliminate the targeted gene using a variety of cre recombinase driver lines. This was the chosen strategy in the RIM1 study. I combined the fRIM1 mouse with 3 different cre driver lines hoping to understand RIM1's role at different but specific neuron populations. Prior to crossing the fRIM1 mice to the cre driver lines, I crossed the cre drivers to a ROSA-YFP reporter mouse and found that these cre drivers were fairly specific for the cells of interest. This however is where some of the cre-lox system's stumbling blocks appear.

Though a cre recombinase transgenic mouse line may have a great deal of specificity when crossed to a ROSA-YFP reporter mouse, there are still question marks that need to be addressed regarding the temporal and spatial expression of cre recombinase in the experimental model of choice. For instance, changes in genetic background, the presence of other transgenes, or even the location of the transgene within the genome can alter cre recombinase expression patterns in unpredictable but consequential ways. Thus, no matter how specific cre recombinase expression appears in a ROSA-YFP reporter mouse, the honest scientist must then validate proper cre expression and subsequent loss of target gene in his chosen experimental model. Fortunately, there are a variety of techniques one can use for that purpose including qRT-PCR, *in situ* hybridization, immunohistochemistry, Western blots, etc.

Another limitation of the ROSA-YFP reporter mice is that they only provide information regarding living cells that have at some point in development undergone recombination. Thus, in order to understand when during development recombination actually occurred, one must analyze YFP expression at many stages during development, both pre- and post-natally.

There is another important flaw in the cre-lox system that must be addressed before conclusions can be drawn. In some mouse lines, for reasons not completely understood, cre recombinase expression turns on in a subset of mice in the germ cell, or early during development. This occurs randomly, though with a fairly predictable rate of incidence. This was the case for all 3 of the fRIM1/cre+ mouse lines. By including in the

genotyping protocol primers that would detect, WT, floxed (fRIM1) and/or recombined (RXX) *Rim1* alleles, I found that within the tail DNA of all 3 mouse lines recombination was occurring at an alarming rate (Table 3.1 Results for fRIM1/POMC-cre are shown but mimic the other 2 mouse lines). In order to detect whether mice possessing the RXX allele in their tail DNA also had a decrease in RIM1 transcripts in their brain, I performed qRT-PCR on Cerebellum, Cortex, DG, CA1 and CA3 from the fRIM1/POMC-cre+, fRIM1/RXX/POMC-cre+ and RXX/RXX/POMC-cre+ mice (Figure 3.1). I found that both groups possessing RXX alleles in their tail DNA had significant decreases in RIM1 transcripts in 4 out of 5 brain regions tests. As a result, I was forced to abandon the fRIM1/DLX-cre line altogether (because an RXX allele was detected in all but 1 of the hundreds of fRIM1/DLX-cre+ mice) and was severely limited in the number of littermate pairs I could utilize from the fRIM1/POMC-cre and fRIM1/KA-cre crosses.

In summary, cre-lox systems have the potential for exquisite specificity for very unique cell types, but the aforementioned issues must be addressed in order to make definitive statements about any results obtained. And addressing those issues may reveal limitations of a particular experimental system that restricts the conclusions drawn from any experimental findings.

Virally Expressed shRNA

An alternative to the cre-lox system for targeting specific cell populations is viral injection and expression of genes of interest. This approach has many benefits including temporal control of the desired genetic manipulation and flexibility in the duration, quantity and type of gene expressed. It is also much easier to generate variants of virally

expressed genes than it is to create new transgenic mice. Finally, with this approach one can ensure that there is normal development prior to inducing whatever genetic manipulation is preferred.

In the PTEN knockdown study, an Adeno-Associated Virus (AAV) was used to express shRNA fragments that would target PTEN transcripts and eliminate them. AAV has the advantage that once expression of the gene of interest begins it continues undiminished for months in the adult mouse. Though it may take up to 2 weeks for expression to begin, this time provides the mouse an opportunity to recover from the surgery prior to beginning behavioral tests. Other viruses have different timing of gene expression. Herpes Simplex Virus (HSV) starts expressing within a couple of days, but is transient and gene expression diminished dramatically within 1 week. Another common virus used for this purpose is the Lentivirus which has the advantage of being able to carry much larger genetic constructs and though takes longer to initiate expression of genes, that expression is long-term and stable. Additionally, viruses have different serotypes that infect specific cell types. For example, the shPTEN expressing virus used in this report is an AAV-serotype 2 and targets neurons, thus injection of the virus into the BLA allows for infection of neurons without infection of local glial cells.

There are however some significant challenges with viral approaches as well. Perhaps the most significant challenge faced in my experiments was that spread of the virus as it leaves the syringe can be difficult to control. Usually, the virus will spread in all directions in a spherical pattern. Typically, the slower the infusion rate, the less spread

observed. However, like all things, the virus tends to travel the path of least resistance which may include the injection tract itself, or along borders created by the normal brain architecture. Furthermore, the targeted brain structures or nuclei are not always spherical or may be anatomically small and thus some amount of spillover into neighboring structures is expected. It is also challenging to infect a large percentage of the cells in the targeted region without overwhelming the tissue with virus.

The AAV-shPTEN injections were faced with most of these challenges and as a result the amount of virus injected was decreased so that it would not spread beyond the BLA. However, this caused a drop in the percentage of total BLA neurons that were infected which may be the cause for the lack of behavioral effects in these mice.

One possible approach to knocking down a gene in a spatially and temporally selective manner while circumventing many of the challenges faced by both cre-lox systems and viral delivery methods would be to combine the two approaches. For instance, it may be possible to inject a lentivirus (that integrates the target genes into the host cell genome), which contains a conditional shRNA construct that is regulated by a stop sequence flanked on either side by loxP sites, into a transgenic mouse that expresses cre recombinase in the preferred cell type or region. With such a method, one could theoretically inject large amounts of virus into the target region without worrying about spillover effects. Furthermore, ectopic expression of cre recombinase would be virtually irrelevant as only the region with viral infection would be affected by the shRNA product. This approach would also provide the benefit of normal mouse

development. Finally, this combined approach would allow a very quick study because 1) there would be no crossing of the cre driver lines and conditional floxed mice, 2) there would be no need for genotyping if mice homozygous for the cre transgene were used, 3) multiple cre driver lines could be injected at the same time, and 4) since viruses can be constructed to bicistronically express YFP, it would be easy to validate the exact cells that have been targeted by the virus.

fRIM1/fRIM1 x fRIM1/WT/POMC-cre+					
Expected Genotypes	**Expected Yield**	**Actual Yield**	**Unexpected Genotypes**	**Expected Yield**	**Actual Yield**
fRIM1/fRIM1 POMC-cre+	25%	4.8%	**fRIM1/RXX POMC-cre+**	0%	13.9%
fRIM1/fRIM1 POMC-cre-	25%	21.6%	**RXX/RXX POMC-cre+**	0%	12.1%
fRIM1/WT POMC-cre+	25%	7.8%	**fRIM1/RXX/WT POMC-cre+**	0%	8.7%
fRIM1/WT POMC-cre-	25%	19.9%	**WT/RXX POMC-cre+**	0%	8.2%

TABLE 3.1 Incidence of all possible genotypes from the fRIM1/fRIM1 X fRIM1/WT/POMC-cre+ cross. The groups of mice within the red outlined area are the genotypes used for experimental and control groups. Percentages shown in red are groups with significant decrease in actual yield compared to expected yield calculated with a Chi Square statistical test ($p < 0.05$). The two groups with a significant decrease in yield are those that posses the POMC-cre transgene.

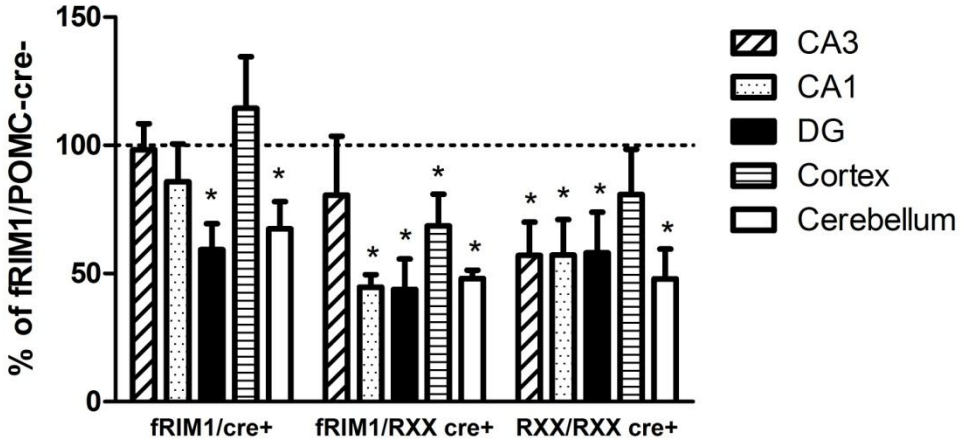

FIGURE 3.1 POMC-cre+ mice that posses RIM1 RXX alleles in their tail DNA show significant decrease in RIM1 transcripts in their brain. Mice possessing the recombined RIM1 allele (RXX) have significant decrease in RIM1 transcripts in 4 of 5 locations in the brain, whereas the fRIM1/cre+ mouse only shows decrease in the DG and cerebellum as expected. (***,** $p < 0.05$ using a one sample t-test; N = 6 mice per

Acknowledgements

I would like to thank Susumu Tonegawa, Joel Elmquist, Thomas Sudhof, and Pascal Kaeser for generously providing the KA-cre and POMC-cre, and fRIM1 mice and providing support as I characterized these mice. Thanks to Luis Parada for providing the PTEN cKO mice. I would also like to thank Scott Russo and Michael Kaplitt for providing the AAV-shPTEN and AAV-shLuc viruses and several occasions as the intracranial surgeries were worked out. Thanks to Dani Dumitriu and James Morrison for teaching me how to fill, image and analyze dendritic spines. Thanks to Shari Birnbaum and Ami Pettersen for their help in the animal core. Thanks to the many members of the Eisch Lab for lending materials and help with immunohistochemistry experiments. Thanks to Jim Richardson and John Shelton from the pathology core and Brian Potts for helping with in situ hybridization experiments. I would also like to thank Thomas Jaramillo and Felipe Espinosa-Becerra for their help performing the intracranial surgeries and electrophysiology respectively. Thanks to Zhong Xuan for teaching me all I know about molecular biology techniques. Thanks to Ajay Rao and Shunan Liu for their tireless watch over the breeding colonies and for the thousands of mice they genotyped on my behalf. I never could have done any of my work without these individuals. Special thanks to Allie Widman for the many hours she spent on neuron studio and the confocal microscope. Without her help, I likely would not have finished this work in time to start medical school when I did.

Over the last 5 years all of the Powell Lab members have provided assistance and support in ways they may not have recognized. In particular, thanks to Jacqueline

Blundell and Cory Blaiss for acting as my guides through failed experiments and counselors during the qualifying exam. I would also like to thank the many summer students who contributed in small ways, even if through failed experiments: Monica Tamil, Landry Jarvis, Ahleum Kim and Simi Kuye. Thank you also to my extended family that believed in me and encouraged me. A special thanks to my brothers Michael Cherry and Nathan Haws who spent time helping me program and do statistical analysis. And of course I can't thank my wife and children enough for the many hours they supported me while I was studying or working. They are my motivation for all I do.

Finally, I would like to thank my mentor, Dr. Craig Powell. From the very beginning he was excited to welcome me into his lab and provide me with many opportunities to succeed. He was patient while I slowly got my feet wet, and encouraging when I was discouraged. He went to many lengths to put me in contact with experts in techniques I used but with which his lab was unfamiliar, sending me to New York University (Morrison lab) and Albert Einstein College of Medicine (Castillo lab) to learn to do cell fills and do mossy fiber LTP field recordings respectively. I am grateful for having studied under his tutelage.

Bibliography

ABEL, T. W., BAKER, S. J., FRASER, M. M., TIHAN, T., NELSON, J. S., YACHNIS, A. T., BOUFFARD, J. P., MENA, H., BURGER, P. C. & EBERHART, C. G. 2005. Lhermitte-Duclos disease: a report of 31 cases with immunohistochemical analysis of the PTEN/AKT/mTOR pathway. *J Neuropathol Exp Neurol,* 64**,** 341-9.

AKBARIAN, S. & HUANG, H. S. 2006. Molecular and cellular mechanisms of altered GAD1/GAD67 expression in schizophrenia and related disorders. *Brain Res Rev,* 52**,** 293-304.

ARELLANO, J. I., BENAVIDES-PICCIONE, R., DEFELIPE, J. & YUSTE, R. 2007. Ultrastructure of dendritic spines: correlation between synaptic and spine morphologies. *Front Neurosci,* 1**,** 131-43.

BACKMAN, S. A., STAMBOLIC, V., SUZUKI, A., HAIGHT, J., ELIA, A., PRETORIUS, J., TSAO, M. S., SHANNON, P., BOLON, B., IVY, G. O. & MAK, T. W. 2001. Deletion of Pten in mouse brain causes seizures, ataxia and defects in soma size resembling Lhermitte-Duclos disease. *Nat Genet,* 29**,** 396-403.

BALTHASAR, N., COPPARI, R., MCMINN, J., LIU, S. M., LEE, C. E., TANG, V., KENNY, C. D., MCGOVERN, R. A., CHUA, S. C., JR., ELMQUIST, J. K. & LOWELL, B. B. 2004. Leptin receptor signaling in POMC neurons is required for normal body weight homeostasis. *Neuron,* 42**,** 983-91.

BANNO, R., ZIMMER, D., DE JONGHE, B. C., ATIENZA, M., RAK, K., YANG, W. & BENCE, K. K. 2010. PTP1B and SHP2 in POMC neurons reciprocally regulate energy balance in mice. *J Clin Invest,* 120**,** 720-34.

BARTLETT, J. S., SAMULSKI, R. J. & MCCOWN, T. J. 1998. Selective and rapid uptake of adeno-associated virus type 2 in brain. *Hum Gene Ther,* 9**,** 1181-6.

BEASLEY, C. L. & REYNOLDS, G. P. 1997. Parvalbumin-immunoreactive neurons are reduced in the prefrontal cortex of schizophrenics. *Schizophr Res,* 24**,** 349-55.

BENES, F. M. & BERRETTA, S. 2001. GABAergic interneurons: implications for understanding schizophrenia and bipolar disorder. *Neuropsychopharmacology,* 25**,** 1-27.

BESSON, A., ROBBINS, S. M. & YONG, V. W. 1999. PTEN/MMAC1/TEP1 in signal transduction and tumorigenesis. *Eur J Biochem,* 263**,** 605-11.

BETZ, A., THAKUR, P., JUNGE, H. J., ASHERY, U., RHEE, J. S., SCHEUSS, V., ROSENMUND, C., RETTIG, J. & BROSE, N. 2001. Functional interaction of the active zone proteins Munc13-1 and RIM1 in synaptic vesicle priming. *Neuron,* 30**,** 183-96.

BISHOP, S. J., DUNCAN, J. & LAWRENCE, A. D. 2004. State anxiety modulation of the amygdala response to unattended threat-related stimuli. *J Neurosci,* 24**,** 10364-8.

BLUNDELL, J., BLAISS, C. A., ETHERTON, M. R., ESPINOSA, F., TABUCHI, K., WALZ, C., BOLLIGER, M. F., SUDHOF, T. C. & POWELL, C. M. 2010a. Neuroligin-1 deletion results in impaired spatial memory and increased repetitive behavior. *J Neurosci,* 30**,** 2115-29.

BLUNDELL, J., KAESER, P. S., SUDHOF, T. C. & POWELL, C. M. 2010b. RIM1alpha and interacting proteins involved in presynaptic plasticity mediate prepulse inhibition and additional behaviors linked to schizophrenia. *J Neurosci,* 30**,** 5326-33.

BLUNDELL, J., TABUCHI, K., BOLLIGER, M. F., BLAISS, C. A., BROSE, N., LIU, X., SUDHOF, T. C. & POWELL, C. M. 2009. Increased anxiety-like behavior in mice lacking the inhibitory synapse cell adhesion molecule neuroligin 2. *Genes Brain Behav,* 8**,** 114-26.

BOCCONE, L., DESSI, V., ZAPPU, A., PIGA, S., PILUDU, M. B., RAIS, M., MASSIDDA, C., DE VIRGILIIS, S., CAO, A. & LOUDIANOS, G. 2006. Bannayan-Riley-Ruvalcaba syndrome with reactive nodular lymphoid hyperplasia and autism and a PTEN mutation. *Am J Med Genet A,* 140**,** 1965-9.

BOURNE, J. & HARRIS, K. M. 2007. Do thin spines learn to be mushroom spines that remember? *Curr Opin Neurobiol,* 17**,** 381-6.

BRYANT, C., JACKSON, H. & AMES, D. 2008. The prevalence of anxiety in older adults: methodological issues and a review of the literature. *J Affect Disord,* 109**,** 233-50.

BUTLER, M. G., DASOUKI, M. J., ZHOU, X. P., TALEBIZADEH, Z., BROWN, M., TAKAHASHI, T. N., MILES, J. H., WANG, C. H., STRATTON, R., PILARSKI, R. & ENG, C. 2005. Subset of individuals with autism spectrum disorders and extreme macrocephaly associated with germline PTEN tumour suppressor gene mutations. *J Med Genet,* 42**,** 318-21.

BUXBAUM, J. D., CAI, G., CHASTE, P., NYGREN, G., GOLDSMITH, J., REICHERT, J., ANCKARSATER, H., RASTAM, M., SMITH, C. J., SILVERMAN, J. M., HOLLANDER, E., LEBOYER, M., GILLBERG, C., VERLOES, A. & BETANCUR, C. 2007. Mutation screening of the PTEN gene in patients with autism spectrum disorders and macrocephaly. *Am J Med Genet B Neuropsychiatr Genet,* 144B**,** 484-91.

CALAKOS, N., SCHOCH, S., SUDHOF, T. C. & MALENKA, R. C. 2004a. Multiple Roles for the Active Zone Protein RIM1[alpha] in Late Stages of Neurotransmitter Release. *Neuron,* 42**,** 889-896.

CALAKOS, N., SCHOCH, S., SUDHOF, T. C. & MALENKA, R. C. 2004b. Multiple roles for the active zone protein RIM1alpha in late stages of neurotransmitter release. *Neuron,* 42**,** 889-96.

CANNICH, A., WOTJAK, C. T., KAMPRATH, K., HERMANN, H., LUTZ, B. & MARSICANO, G. 2004. CB1 cannabinoid receptors modulate kinase and phosphatase activity during extinction of conditioned fear in mice. *Learn Mem,* 11**,** 625-32.

CARIM-TODD, L., BATH, K. G., FULGENZI, G., YANPALLEWAR, S., JING, D., BARRICK, C. A., BECKER, J., BUCKLEY, H., DORSEY, S. G., LEE, F. S. & TESSAROLLO, L. 2009. Endogenous truncated TrkB.T1 receptor regulates neuronal complexity and TrkB kinase receptor function in vivo. *J Neurosci,* 29**,** 678-85.

CASTILLO, P. E., SCHOCH, S., SCHMITZ, F., SUDHOF, T. C. & MALENKA, R. C. 2002. RIM1alpha is required for presynaptic long-term potentiation. *Nature,* 415**,** 327-30.

CAZORLA, M., JOUVENCEAU, A., ROSE, C., GUILLOUX, J. P., PILON, C., DRANOVSKY, A. & PREMONT, J. 2010. Cyclotraxin-B, the first highly potent and selective TrkB inhibitor, has anxiolytic properties in mice. *PLoS One,* 5**,** e9777.

CHEVALEYRE, V., HEIFETS, B. D., KAESER, P. S., SUDHOF, T. C. & CASTILLO, P. E. 2007. Endocannabinoid-mediated long-term plasticity requires cAMP/PKA signaling and RIM1alpha. *Neuron,* 54**,** 801-12.

CHEVALEYRE, V., TAKAHASHI, K. A. & CASTILLO, P. E. 2006. Endocannabinoid-mediated synaptic plasticity in the CNS. *Annu Rev Neurosci,* 29**,** 37-76.

CHHATWAL, J. P., DAVIS, M., MAGUSCHAK, K. A. & RESSLER, K. J. 2005. Enhancing cannabinoid neurotransmission augments the extinction of conditioned fear. *Neuropsychopharmacology,* 30**,** 516-24.

COCHRAN, S. M., FUJIMURA, M., MORRIS, B. J. & PRATT, J. A. 2002. Acute and delayed effects of phencyclidine upon mRNA levels of markers of glutamatergic and GABAergic neurotransmitter function in the rat brain. *Synapse,* 46**,** 206-14.

COPPOLA, T., MAGNIN-LUTHI, S., PERRET-MENOUD, V., GATTESCO, S., SCHIAVO, G. & REGAZZI, R. 2001. Direct interaction of the Rab3 effector RIM with Ca2+ channels, SNAP-25, and synaptotagmin. *J Biol Chem,* 276**,** 32756-62.

D'ADAMO, P., WOLFER, D. P., KOPP, C., TOBLER, I., TONIOLO, D. & LIPP, H. P. 2004. Mice deficient for the synaptic vesicle protein Rab3a show impaired spatial reversal learning and increased explorative activity but none of the behavioral changes shown by mice deficient for the Rab3a regulator Gdi1. *Eur J Neurosci,* 19**,** 1895-905.

DAHIA, P. L. 2000. PTEN, a unique tumor suppressor gene. *Endocr Relat Cancer,* 7**,** 115-29.

DAVIS, M. 1992. The role of the amygdala in fear and anxiety. *Annu Rev Neurosci,* 15**,** 353-75.

DENNIS, N. A., CABEZA, R., NEED, A. C., WATERS-METENIER, S., GOLDSTEIN, D. B. & LABAR, K. S. 2010. Brain-derived neurotrophic factor val66met polymorphism and hippocampal activation during episodic encoding and retrieval tasks. *Hippocampus*.

DI CRISTOFANO, A. & PANDOLFI, P. P. 2000. The multiple roles of PTEN in tumor suppression. *Cell,* 100**,** 387-90.

DOBRUNZ, L. E. & STEVENS, C. F. 1997. Heterogeneity of release probability, facilitation, and depletion at central synapses. *Neuron,* 18**,** 995-1008.

DOWNES, C. P., BENNETT, D., MCCONNACHIE, G., LESLIE, N. R., PASS, I., MACPHEE, C., PATEL, L. & GRAY, A. 2001. Antagonism of PI 3-kinase-dependent signalling pathways by the tumour suppressor protein, PTEN. *Biochem Soc Trans,* 29**,** 846-51.

DUMITRIU, D., HAO, J., HARA, Y., KAUFMANN, J., JANSSEN, W. G., LOU, W., RAPP, P. R. & MORRISON, J. H. 2010. Selective changes in thin spine density and morphology in monkey prefrontal cortex correlate with aging-related cognitive impairment. *J Neurosci,* 30**,** 7507-15.

DUMITRIU, D., RODRIGUEZ, A. & MORRISON, J. H. 2011. High-throughput, detailed, cell-specific neuroanatomy of dendritic spines using microinjection and confocal microscopy. *Nat Protoc,* 6**,** 1391-411.

DYMECKI, S. M. 1996. Flp recombinase promotes site-specific DNA recombination in embryonic stem cells and transgenic mice. *Proc Natl Acad Sci U S A,* 93**,** 6191-6.

EASTWOOD, S. L., COTTER, D. & HARRISON, P. J. 2001. Cerebellar synaptic protein expression in schizophrenia. *Neuroscience,* 105**,** 219-29.

ENG, C. 1999. The role of PTEN, a phosphatase gene, in inherited and sporadic nonmedullary thyroid tumors. *Recent Prog Horm Res,* 54**,** 441-52; discussion 453.

ENG, C. 2003. PTEN: one gene, many syndromes. *Hum Mutat,* 22**,** 183-98.

ETHERTON, M. R., BLAISS, C. A., POWELL, C. M. & SUDHOF, T. C. 2009. Mouse neurexin-1alpha deletion causes correlated electrophysiological and behavioral changes consistent with cognitive impairments. *Proc Natl Acad Sci U S A,* 106**,** 17998-8003.

FERGUSON, G. D., WANG, H., HERSCHMAN, H. R. & STORM, D. R. 2004. Altered hippocampal short-term plasticity and associative memory in synaptotagmin IV (-/-) mice. *Hippocampus,* 14**,** 964-74.

FIALA, J. C., ALLWARDT, B. & HARRIS, K. M. 2002. Dendritic spines do not split during hippocampal LTP or maturation. *Nat Neurosci,* 5**,** 297-8.

FRASER, M. M., BAYAZITOV, I. T., ZAKHARENKO, S. S. & BAKER, S. J. 2008. Phosphatase and tensin homolog, deleted on chromosome 10 deficiency in brain causes defects in synaptic structure, transmission and plasticity, and myelination abnormalities. *Neuroscience,* 151**,** 476-88.

FUKUSHIMA, F., NAKAO, K., SHINOE, T., FUKAYA, M., MURAMATSU, S., SAKIMURA, K., KATAOKA, H., MORI, H., WATANABE, M., MANABE, T. & MISHINA, M. 2009. Ablation of NMDA receptors enhances the excitability of hippocampal CA3 neurons. *PLoS One,* 4**,** e3993.

GLANTZ, L. A. & LEWIS, D. A. 1997. Reduction of synaptophysin immunoreactivity in the prefrontal cortex of subjects with schizophrenia. Regional and diagnostic specificity. *Arch Gen Psychiatry,* 54**,** 660-9.

GOFFIN, A., HOEFSLOOT, L. H., BOSGOED, E., SWILLEN, A. & FRYNS, J. P. 2001. PTEN mutation in a family with Cowden syndrome and autism. *Am J Med Genet,* 105**,** 521-4.

GOLDIN, P. R., MANBER, T., HAKIMI, S., CANLI, T. & GROSS, J. J. 2009. Neural bases of social anxiety disorder: emotional reactivity and cognitive regulation during social and physical threat. *Arch Gen Psychiatry,* 66**,** 170-80.

GOVINDARAJAN, A., RAO, B. S., NAIR, D., TRINH, M., MAWJEE, N., TONEGAWA, S. & CHATTARJI, S. 2006. Transgenic brain-derived neurotrophic factor expression causes both anxiogenic and antidepressant effects. *Proc Natl Acad Sci U S A,* 103**,** 13208-13.

GUIDOTTI, A., AUTA, J., DAVIS, J. M., DI-GIORGI-GEREVINI, V., DWIVEDI, Y., GRAYSON, D. R., IMPAGNATIELLO, F., PANDEY, G., PESOLD, C., SHARMA, R., UZUNOV, D. & COSTA, E. 2000. Decrease in reelin and glutamic acid decarboxylase67 (GAD67) expression in schizophrenia and bipolar disorder: a postmortem brain study. *Arch Gen Psychiatry,* 57**,** 1061-9.

HAO, J., RAPP, P. R., LEFFLER, A. E., LEFFLER, S. R., JANSSEN, W. G., LOU, W., MCKAY, H., ROBERTS, J. A., WEARNE, S. L., HOF, P. R. & MORRISON, J. H. 2006. Estrogen alters spine number and morphology in prefrontal cortex of aged female rhesus monkeys. *J Neurosci,* 26**,** 2571-8.

HARRIS, K. M. & STEVENS, J. K. 1989. Dendritic spines of CA 1 pyramidal cells in the rat hippocampus: serial electron microscopy with reference to their biophysical characteristics. *J Neurosci,* 9**,** 2982-97.

HASHIMOTO, T., VOLK, D. W., EGGAN, S. M., MIRNICS, K., PIERRI, J. N., SUN, Z., SAMPSON, A. R. & LEWIS, D. A. 2003. Gene expression deficits in a subclass of GABA neurons in the prefrontal cortex of subjects with schizophrenia. *J Neurosci,* 23**,** 6315-26.

HAWS, M. E., KAESER, P. S., JARVIS, D. L., SUDHOF, T. C. & POWELL, C. M. 2012. Region-specific deletions of RIM1 reproduce a subset of global RIM1alpha(-/-) phenotypes. *Genes Brain Behav,* 11**,** 201-13.

HENSBROEK, R. A., KAMAL, A., BAARS, A. M., VERHAGE, M. & SPRUIJT, B. M. 2003. Spatial, contextual and working memory are not affected by the absence of mossy fiber long-term potentiation and depression. *Behav Brain Res,* 138**,** 215-23.

HENZE, D. A., URBAN, N. N. & BARRIONUEVO, G. 2000. The multifarious hippocampal mossy fiber pathway: a review. *Neuroscience,* 98**,** 407-27.

HERMAN, G. E., BUTTER, E., ENRILE, B., PASTORE, M., PRIOR, T. W. & SOMMER, A. 2007. Increasing knowledge of PTEN germline mutations: Two additional patients with autism and macrocephaly. *Am J Med Genet A,* 143**,** 589-93.

HOBERT, J. A. & ENG, C. 2009. PTEN hamartoma tumor syndrome: an overview. *Genet Med,* 11**,** 687-94.

HOEFFER, C. A. & KLANN, E. 2010. mTOR signaling: at the crossroads of plasticity, memory and disease. *Trends Neurosci,* 33**,** 67-75.

HOLZSCHNEIDER, K. & MULERT, C. 2011. Neuroimaging in anxiety disorders. *Dialogues Clin Neurosci,* 13**,** 453-61.

HUANG, Y. Y., KANDEL, E. R., VARSHAVSKY, L., BRANDON, E. P., QI, M., IDZERDA, R. L., MCKNIGHT, G. S. & BOURTCHOULADZE, R. 1995. A genetic test of the effects of mutations in PKA on mossy fiber LTP and its relation to spatial and contextual learning. *Cell,* 83**,** 1211-22.

KAESER, P. S., KWON, H. B., CHIU, C. Q., DENG, L., CASTILLO, P. E. & SUDHOF, T. C. 2008. RIM1alpha and RIM1beta are synthesized from distinct promoters of the RIM1 gene to mediate differential but overlapping synaptic functions. *J Neurosci,* 28**,** 13435-47.

KAMPRATH, K., MARSICANO, G., TANG, J., MONORY, K., BISOGNO, T., DI MARZO, V., LUTZ, B. & WOTJAK, C. T. 2006. Cannabinoid CB1 receptor mediates fear extinction via habituation-like processes. *J Neurosci,* 26**,** 6677-86.

KANDEL, E. R. 2001. The molecular biology of memory storage: a dialogue between genes and synapses. *Science,* 294**,** 1030-8.

KESSLER, R. C., CHIU, W. T., DEMLER, O., MERIKANGAS, K. R. & WALTERS, E. E. 2005. Prevalence, severity, and comorbidity of 12-month DSM-IV disorders in the National Comorbidity Survey Replication. *Arch Gen Psychiatry,* 62**,** 617-27.

KIM, M. J., LOUCKS, R. A., PALMER, A. L., BROWN, A. C., SOLOMON, K. M., MARCHANTE, A. N. & WHALEN, P. J. 2011. The structural and functional connectivity of the amygdala: from normal emotion to pathological anxiety. *Behav Brain Res,* 223**,** 403-10.

KINNEY, J. W., DAVIS, C. N., TABAREAN, I., CONTI, B., BARTFAI, T. & BEHRENS, M. M. 2006. A specific role for NR2A-containing NMDA receptors in the maintenance of parvalbumin and GAD67 immunoreactivity in cultured interneurons. *J Neurosci,* 26**,** 1604-15.

KOHWI, M., PETRYNIAK, M. A., LONG, J. E., EKKER, M., OBATA, K., YANAGAWA, Y., RUBENSTEIN, J. L. & ALVAREZ-BUYLLA, A. 2007. A subpopulation of olfactory bulb GABAergic interneurons is derived from Emx1- and Dlx5/6-expressing progenitors. *J Neurosci,* 27**,** 6878-91.

KWON, C. H., LUIKART, B. W., POWELL, C. M., ZHOU, J., MATHENY, S. A., ZHANG, W., LI, Y., BAKER, S. J. & PARADA, L. F. 2006. Pten regulates neuronal arborization and social interaction in mice. *Neuron,* 50**,** 377-88.

KWON, C. H., ZHU, X., ZHANG, J. & BAKER, S. J. 2003. mTor is required for hypertrophy of Pten-deficient neuronal soma in vivo. *Proc Natl Acad Sci U S A,* 100**,** 12923-8.

KWON, C. H., ZHU, X., ZHANG, J., KNOOP, L. L., THARP, R., SMEYNE, R. J., EBERHART, C. G., BURGER, P. C. & BAKER, S. J. 2001. Pten regulates neuronal soma size: a mouse model of Lhermitte-Duclos disease. *Nat Genet,* 29**,** 404-11.

LAGACE, D. C., WHITMAN, M. C., NOONAN, M. A., ABLES, J. L., DECAROLIS, N. A., ARGUELLO, A. A., DONOVAN, M. H., FISCHER, S. J., FARNBAUCH, L. A., BEECH, R. D., DILEONE, R. J., GREER, C. A., MANDYAM, C. D. & EISCH, A. J. 2007. Dynamic contribution of nestin-expressing stem cells to adult neurogenesis. *J Neurosci,* 27**,** 12623-9.

LAKSHMINARASIMHAN, H. & CHATTARJI, S. 2012. Stress leads to contrasting effects on the levels of brain derived neurotrophic factor in the hippocampus and amygdala. *PLoS One,* 7**,** e30481.

LESLIE, N. R. & DOWNES, C. P. 2002. PTEN: The down side of PI 3-kinase signalling. *Cell Signal,* 14**,** 285-95.

LEWIS, D. A., HASHIMOTO, T. & VOLK, D. W. 2005. Cortical inhibitory neurons and schizophrenia. *Nat Rev Neurosci,* 6**,** 312-24.

LI, J., YEN, C., LIAW, D., PODSYPANINA, K., BOSE, S., WANG, S. I., PUC, J., MILIARESIS, C., RODGERS, L., MCCOMBIE, R., BIGNER, S. H., GIOVANELLA, B. C., ITTMANN, M., TYCKO, B., HIBSHOOSH, H., WIGLER, M. H. & PARSONS, R. 1997. PTEN, a putative protein tyrosine phosphatase gene mutated in human brain, breast, and prostate cancer. *Science,* 275**,** 1943-7.

LI, Q., CLARK, S., LEWIS, D. V. & WILSON, W. A. 2002. NMDA receptor antagonists disinhibit rat posterior cingulate and retrosplenial cortices: a potential mechanism of neurotoxicity. *J Neurosci,* 22**,** 3070-80.

LICHTMAN, A. H., VARVEL, S. A. & MARTIN, B. R. 2002. Endocannabinoids in cognition and dependence. *Prostaglandins Leukot Essent Fatty Acids,* 66**,** 269-85.

LONART, G., SCHOCH, S., KAESER, P. S., LARKIN, C. J., SUDHOF, T. C. & LINDEN, D. J. 2003. Phosphorylation of RIM1alpha by PKA triggers presynaptic long-term potentiation at cerebellar parallel fiber synapses. *Cell,* 115**,** 49-60.

LUIKART, B. W., SCHNELL, E., WASHBURN, E. K., BENSEN, A. L., TOVAR, K. R. & WESTBROOK, G. L. 2011. Pten knockdown in vivo increases excitatory drive onto dentate granule cells. *J Neurosci,* 31**,** 4345-54.

MAEHAMA, T. & DIXON, J. E. 1998. The tumor suppressor, PTEN/MMAC1, dephosphorylates the lipid second messenger, phosphatidylinositol 3,4,5-trisphosphate. *J Biol Chem,* 273**,** 13375-8.

MAEHAMA, T. & DIXON, J. E. 1999. PTEN: a tumour suppressor that functions as a phospholipid phosphatase. *Trends Cell Biol,* 9**,** 125-8.

MAHAN, A. L. & RESSLER, K. J. 2012. Fear conditioning, synaptic plasticity and the amygdala: implications for posttraumatic stress disorder. *Trends Neurosci,* 35**,** 24-35.

MARSICANO, G., WOTJAK, C. T., AZAD, S. C., BISOGNO, T., RAMMES, G., CASCIO, M. G., HERMANN, H., TANG, J., HOFMANN, C., ZIEGLGANSBERGER, W., DI MARZO, V. & LUTZ, B. 2002. The endogenous cannabinoid system controls extinction of aversive memories. *Nature,* 418**,** 530-4.

MATSUO, N., REIJMERS, L. & MAYFORD, M. 2008. Spine-type-specific recruitment of newly synthesized AMPA receptors with learning. *Science,* 319**,** 1104-7.

MATYNIA, A., KUSHNER, S. A. & SILVA, A. J. 2002. Genetic approaches to molecular and cellular cognition: a focus on LTP and learning and memory. *Annu Rev Genet,* 36**,** 687-720.

MCBRIDE, K. L., VARGA, E. A., PASTORE, M. T., PRIOR, T. W., MANICKAM, K., ATKIN, J. F. & HERMAN, G. E. 2010. Confirmation study of PTEN mutations among individuals with autism or developmental delays/mental retardation and macrocephaly. *Autism Res,* 3**,** 137-41.

MCDONALD, A. J. 1982. Neurons of the lateral and basolateral amygdaloid nuclei: a Golgi study in the rat. *J Comp Neurol,* 212**,** 293-312.

MCHUGH, T. J., JONES, M. W., QUINN, J. J., BALTHASAR, N., COPPARI, R., ELMQUIST, J. K., LOWELL, B. B., FANSELOW, M. S., WILSON, M. A. & TONEGAWA, S. 2007. Dentate gyrus NMDA receptors mediate rapid pattern separation in the hippocampal network. *Science,* 317**,** 94-9.

MCILWAIN, K. L., MERRIWEATHER, M. Y., YUVA-PAYLOR, L. A. & PAYLOR, R. 2001. The use of behavioral test batteries: effects of training history. *Physiol Behav,* 73**,** 705-17.

MERIKANGAS, K. R., HE, J. P., BURSTEIN, M., SWANSON, S. A., AVENEVOLI, S., CUI, L., BENJET, C., GEORGIADES, K. & SWENDSEN, J. 2010. Lifetime prevalence of mental disorders in U.S. adolescents: results from the National Comorbidity Survey Replication--Adolescent Supplement (NCS-A). *J Am Acad Child Adolesc Psychiatry,* 49**,** 980-9.

MITRA, R., JADHAV, S., MCEWEN, B. S., VYAS, A. & CHATTARJI, S. 2005. Stress duration modulates the spatiotemporal patterns of spine formation in the basolateral amygdala. *Proc Natl Acad Sci U S A,* 102**,** 9371-6.

MOULT, P. R., CROSS, A., SANTOS, S. D., CARVALHO, A. L., LINDSAY, Y., CONNOLLY, C. N., IRVING, A. J., LESLIE, N. R. & HARVEY, J. 2010. Leptin regulates AMPA receptor trafficking via PTEN inhibition. *J Neurosci,* 30**,** 4088-101.

MUKAETOVA-LADINSKA, E. B., HURT, J., HONER, W. G., HARRINGTON, C. R. & WISCHIK, C. M. 2002. Loss of synaptic but not cytoskeletal proteins in the cerebellum of chronic schizophrenics. *Neurosci Lett,* 317**,** 161-5.

NAKAZAWA, K., QUIRK, M. C., CHITWOOD, R. A., WATANABE, M., YECKEL, M. F., SUN, L. D., KATO, A., CARR, C. A., JOHNSTON, D., WILSON, M. A. & TONEGAWA, S. 2002. Requirement for hippocampal CA3 NMDA receptors in associative memory recall. *Science,* 297**,** 211-8.

NELEN, M. R., VAN STAVEREN, W. C., PEETERS, E. A., HASSEL, M. B., GORLIN, R. J., HAMM, H., LINDBOE, C. F., FRYNS, J. P., SIJMONS, R. H., WOODS, D. G., MARIMAN, E. C., PADBERG, G. W. & KREMER, H. 1997. Germline mutations in the PTEN/MMAC1 gene in patients with Cowden disease. *Hum Mol Genet,* 6**,** 1383-7.

NUSSER, Z., LUJAN, R., LAUBE, G., ROBERTS, J. D., MOLNAR, E. & SOMOGYI, P. 1998. Cell type and pathway dependence of synaptic AMPA receptor number and variability in the hippocampus. *Neuron,* 21**,** 545-59.

OHTSUKA, T., TAKAO-RIKITSU, E., INOUE, E., INOUE, M., TAKEUCHI, M., MATSUBARA, K., DEGUCHI-TAWARADA, M., SATOH, K., MORIMOTO, K., NAKANISHI, H. & TAKAI, Y. 2002. Cast: a novel protein of the cytomatrix at the active zone of synapses that forms a ternary complex with RIM1 and munc13-1. *J Cell Biol,* 158**,** 577-90.

ORLOFF, M. S. & ENG, C. 2008. Genetic and phenotypic heterogeneity in the PTEN hamartoma tumour syndrome. *Oncogene,* 27**,** 5387-97.

ORRICO, A., GALLI, L., BUONI, S., ORSI, A., VONELLA, G. & SORRENTINO, V. 2009. Novel PTEN mutations in neurodevelopmental disorders and macrocephaly. *Clin Genet,* 75**,** 195-8.

PAYLOR, R., SPENCER, C. M., YUVA-PAYLOR, L. A. & PIEKE-DAHL, S. 2006. The use of behavioral test batteries, II: effect of test interval. *Physiol Behav,* 87**,** 95-102.

PFAFFL, M. W. 2001. A new mathematical model for relative quantification in real-time RT-PCR. *Nucleic Acids Res,* 29**,** e45.

POWELL, C. M. 2006. Gene targeting of presynaptic proteins in synaptic plasticity and memory: across the great divide. *Neurobiol Learn Mem,* 85**,** 2-15.

POWELL, C. M., SCHOCH, S., MONTEGGIA, L., BARROT, M., MATOS, M. F., FELDMANN, N., SUDHOF, T. C. & NESTLER, E. J. 2004. The presynaptic active zone protein RIM1alpha is critical for normal learning and memory. *Neuron,* 42**,** 143-53.

RADLEY, J. J. & MORRISON, J. H. 2005. Repeated stress and structural plasticity in the brain. *Ageing Res Rev,* 4**,** 271-87.

RAMADORI, G., FUJIKAWA, T., FUKUDA, M., ANDERSON, J., MORGAN, D. A., MOSTOSLAVSKY, R., STUART, R. C., PERELLO, M., VIANNA, C. R., NILLNI, E. A., RAHMOUNI, K. & COPPARI, R. 2010. SIRT1 deacetylase in POMC neurons is required for homeostatic defenses against diet-induced obesity. *Cell Metab,* 12**,** 78-87.

RAMSAWH, H. J., CHAVIRA, D. A. & STEIN, M. B. 2010. Burden of anxiety disorders in pediatric medical settings: prevalence, phenomenology, and a research agenda. *Arch Pediatr Adolesc Med,* 164**,** 965-72.

REINHOLD, J. A., MANDOS, L. A., RICKELS, K. & LOHOFF, F. W. 2011. Pharmacological treatment of generalized anxiety disorder. *Expert Opin Pharmacother,* 12**,** 2457-67.

ROBINSON, L., GOONAWARDENA, A. V., PERTWEE, R. G., HAMPSON, R. E. & RIEDEL, G. 2007. The synthetic cannabinoid HU210 induces spatial memory deficits and suppresses hippocampal firing rate in rats. *Br J Pharmacol,* 151**,** 688-700.

RODRIGUEZ, A., EHLENBERGER, D. B., DICKSTEIN, D. L., HOF, P. R. & WEARNE, S. L. 2008. Automated three-dimensional detection and shape classification of dendritic spines from fluorescence microscopy images. *PLoS One,* 3**,** e1997.

ROOZENDAAL, B., MCEWEN, B. S. & CHATTARJI, S. 2009. Stress, memory and the amygdala. *Nat Rev Neurosci,* 10**,** 423-33.

SAWADA, K., BARR, A. M., NAKAMURA, M., ARIMA, K., YOUNG, C. E., DWORK, A. J., FALKAI, P., PHILLIPS, A. G. & HONER, W. G. 2005. Hippocampal complexin proteins and cognitive dysfunction in schizophrenia. *Arch Gen Psychiatry,* 62**,** 263-72.

SCHOCH, S., CASTILLO, P. E., JO, T., MUKHERJEE, K., GEPPERT, M., WANG, Y., SCHMITZ, F., MALENKA, R. C. & SUDHOF, T. C. 2002. RIM1alpha forms a protein scaffold for regulating neurotransmitter release at the active zone. *Nature,* 415**,** 321-6.

SHELTON, J. M., LEE, M. H., RICHARDSON, J. A. & PATEL, S. B. 2000. Microsomal triglyceride transfer protein expression during mouse development. *J Lipid Res,* 41**,** 532-7.

SILVA, A. J., ROSAHL, T. W., CHAPMAN, P. F., MAROWITZ, Z., FRIEDMAN, E., FRANKLAND, P. W., CESTARI, V., CIOFFI, D., SUDHOF, T. C. & BOURTCHULADZE, R. 1996. Impaired learning in mice with abnormal short-lived plasticity. *Curr Biol,* 6**,** 1509-18.

SINGEC, I., KNOTH, R., DITTER, M., FROTSCHER, M. & VOLK, B. 2003. Neurogranin expression by cerebellar neurons in rodents and non-human primates. *J Comp Neurol,* 459**,** 278-89.

SMITH, L. 2011. Good planning and serendipity: exploiting the Cre/Lox system in the testis. *Reproduction,* 141**,** 151-61.

SOMERVILLE, L. H., KIM, H., JOHNSTONE, T., ALEXANDER, A. L. & WHALEN, P. J. 2004. Human amygdala responses during presentation of happy and neutral faces: correlations with state anxiety. *Biol Psychiatry,* 55**,** 897-903.

SORIANO, P. 1999. Generalized lacZ expression with the ROSA26 Cre reporter strain. *Nat Genet,* 21**,** 70-1.

STECK, P. A., PERSHOUSE, M. A., JASSER, S. A., YUNG, W. K., LIN, H., LIGON, A. H., LANGFORD, L. A., BAUMGARD, M. L., HATTIER, T., DAVIS, T., FRYE, C., HU, R., SWEDLUND, B., TENG, D. H. & TAVTIGIAN, S. V. 1997. Identification of a candidate tumour suppressor gene, MMAC1, at chromosome 10q23.3 that is mutated in multiple advanced cancers. *Nat Genet,* 15**,** 356-62.

STEIN, M. B., GOLDIN, P. R., SAREEN, J., ZORRILLA, L. T. & BROWN, G. G. 2002. Increased amygdala activation to angry and contemptuous faces in generalized social phobia. *Arch Gen Psychiatry,* 59**,** 1027-34.

STEIN, M. T., ELIAS, E. R., SAENZ, M., PICKLER, L. & REYNOLDS, A. 2010. Autistic spectrum disorder in a 9-year-old girl with macrocephaly. *J Dev Behav Pediatr,* 31**,** 632-4.

STUBER, G. D., SPARTA, D. R., STAMATAKIS, A. M., VAN LEEUWEN, W. A., HARDJOPRAJITNO, J. E., CHO, S., TYE, K. M., KEMPADOO, K. A., ZHANG, F., DEISSEROTH, K. & BONCI, A. 2011. Excitatory transmission from the amygdala to nucleus accumbens facilitates reward seeking. *Nature,* 475**,** 377-80.

SUNDBERG, R., CASTENSSON, A. & JAZIN, E. 2006. Statistical modeling in case-control real-time RT-PCR assays, for identification of differentially expressed genes in schizophrenia. *Biostatistics,* 7**,** 130-44.

TABUCHI, K., BLUNDELL, J., ETHERTON, M. R., HAMMER, R. E., LIU, X., POWELL, C. M. & SUDHOF, T. C. 2007. A neuroligin-3 mutation implicated in autism increases inhibitory synaptic transmission in mice. *Science,* 318**,** 71-6.

TAKAO-RIKITSU, E., MOCHIDA, S., INOUE, E., DEGUCHI-TAWARADA, M., INOUE, M., OHTSUKA, T. & TAKAI, Y. 2004. Physical and functional interaction of the active zone proteins, CAST, RIM1, and Bassoon, in neurotransmitter release. *J Cell Biol,* 164**,** 301-11.

TAMMINGA, C., HASHIMOTO, T., VOLK, D. W. & LEWIS, D. A. 2004. GABA neurons in the human prefrontal cortex. *Am J Psychiatry,* 161**,** 1764.

TONEGAWA, S., NAKAZAWA, K. & WILSON, M. A. 2003. Genetic neuroscience of mammalian learning and memory. *Philos Trans R Soc Lond B Biol Sci,* 358**,** 787-95.

VARGA, E. A., PASTORE, M., PRIOR, T., HERMAN, G. E. & MCBRIDE, K. L. 2009. The prevalence of PTEN mutations in a clinical pediatric cohort with autism spectrum disorders, developmental delay, and macrocephaly. *Genet Med,* 11**,** 111-7.

VARVEL, S. A., ANUM, E. A. & LICHTMAN, A. H. 2005. Disruption of CB(1) receptor signaling impairs extinction of spatial memory in mice. *Psychopharmacology (Berl),* 179**,** 863-72.

VAZQUEZ, F. & SELLERS, W. R. 2000. The PTEN tumor suppressor protein: an antagonist of phosphoinositide 3-kinase signaling. *Biochim Biophys Acta,* 1470**,** M21-35.

VYAS, A., MITRA, R., SHANKARANARAYANA RAO, B. S. & CHATTARJI, S. 2002. Chronic stress induces contrasting patterns of dendritic remodeling in hippocampal and amygdaloid neurons. *J Neurosci,* 22**,** 6810-8.

WAITE, K. A. & ENG, C. 2002. Protean PTEN: form and function. *Am J Hum Genet,* 70**,** 829-44.

WANG, P. S., LANE, M., OLFSON, M., PINCUS, H. A., WELLS, K. B. & KESSLER, R. C. 2005. Twelve-month use of mental health services in the United States: results from the National Comorbidity Survey Replication. *Arch Gen Psychiatry,* 62**,** 629-40.

WANG, Y., LIU, X., BIEDERER, T. & SUDHOF, T. C. 2002. A family of RIM-binding proteins regulated by alternative splicing: Implications for the genesis of synaptic active zones. *Proc Natl Acad Sci U S A,* 99**,** 14464-9.

WANG, Y., OKAMOTO, M., SCHMITZ, F., HOFMANN, K. & SUDHOF, T. C. 1997. Rim is a putative Rab3 effector in regulating synaptic-vesicle fusion. *Nature,* 388**,** 593-8.

WANG, Y., SUGITA, S. & SUDHOF, T. C. 2000. The RIM/NIM family of neuronal C2 domain proteins. Interactions with Rab3 and a new class of Src homology 3 domain proteins. *J Biol Chem,* 275**,** 20033-44.

WEEBER, E. J., BEFFERT, U., JONES, C., CHRISTIAN, J. M., FORSTER, E., SWEATT, J. D. & HERZ, J. 2002a. Reelin and ApoE receptors cooperate to enhance hippocampal synaptic plasticity and learning. *J Biol Chem,* 277**,** 39944-52.

WEEBER, E. J., LEVENSON, J. M. & SWEATT, J. D. 2002b. Molecular genetics of human cognition. *Mol Interv,* 2**,** 376-91, 339.

WEEBER, E. J. & SWEATT, J. D. 2002. Molecular neurobiology of human cognition. *Neuron,* 33**,** 845-8.

WOO, T. U., WALSH, J. P. & BENES, F. M. 2004. Density of glutamic acid decarboxylase 67 messenger RNA-containing neurons that express the N-methyl-D-aspartate receptor subunit NR2A in the anterior cingulate cortex in schizophrenia and bipolar disorder. *Arch Gen Psychiatry,* 61**,** 649-57.

XI, D., ZHANG, W., WANG, H. X., STRADTMAN, G. G. & GAO, W. J. 2009. Dizocilpine (MK-801) induces distinct changes of N-methyl-D-aspartic acid receptor subunits in parvalbumin-

containing interneurons in young adult rat prefrontal cortex. *Int J Neuropsychopharmacol,* 12**,** 1395-408.

XIONG, Q., OVIEDO, H. V., TROTMAN, L. C. & ZADOR, A. M. 2012. PTEN Regulation of Local and Long-Range Connections in Mouse Auditory Cortex. *J Neurosci,* 32**,** 1643-52.

XU, Y., JONES, J. E., KOHNO, D., WILLIAMS, K. W., LEE, C. E., CHOI, M. J., ANDERSON, J. G., HEISLER, L. K., ZIGMAN, J. M., LOWELL, B. B. & ELMQUIST, J. K. 2008. 5-HT2CRs expressed by pro-opiomelanocortin neurons regulate energy homeostasis. *Neuron,* 60**,** 582-9.

YEE, C. L., WANG, Y., ANDERSON, S., EKKER, M. & RUBENSTEIN, J. L. 2009. Arcuate nucleus expression of NKX2.1 and DLX and lineages expressing these transcription factors in neuropeptide Y(+), proopiomelanocortin(+), and tyrosine hydroxylase(+) neurons in neonatal and adult mice. *J Comp Neurol,* 517**,** 37-50.

YOON, K. L., FITZGERALD, D. A., ANGSTADT, M., MCCARRON, R. A. & PHAN, K. L. 2007. Amygdala reactivity to emotional faces at high and low intensity in generalized social phobia: a 4-Tesla functional MRI study. *Psychiatry Res,* 154**,** 93-8.

YOUNG, J. W., ZHOU, X. & GEYER, M. A. 2010. Animal models of schizophrenia. *Curr Top Behav Neurosci,* 4**,** 391-433.

YU, M. C., CHO, E., LUO, C. B., LI, W. W., SHEN, W. Z. & YEW, D. T. 1996. Immunohistochemical studies of GABA and parvalbumin in the developing human cerebellum. *Neuroscience,* 70**,** 267-76.

ZHANG, C., WU, B., BEGLOPOULOS, V., WINES-SAMUELSON, M., ZHANG, D., DRAGATSIS, I., SUDHOF, T. C. & SHEN, J. 2009. Presenilins are essential for regulating neurotransmitter release. *Nature,* 460**,** 632-6.

ZHOU, J., BLUNDELL, J., OGAWA, S., KWON, C. H., ZHANG, W., SINTON, C., POWELL, C. M. & PARADA, L. F. 2009. Pharmacological inhibition of mTORC1 suppresses anatomical, cellular, and behavioral abnormalities in neural-specific Pten knock-out mice. *J Neurosci,* 29**,** 1773-83.

ZORI, R. T., MARSH, D. J., GRAHAM, G. E., MARLISS, E. B. & ENG, C. 1998. Germline PTEN mutation in a family with Cowden syndrome and Bannayan-Riley-Ruvalcaba syndrome. *Am J Med Genet,* 80**,** 399-402.